DISSERTATION

GRAVITY WAVE AND MICROPHYSICAL EFFECTS ON BOW ECHO DEVELOPMENT

Submitted by

Rebecca Denise Adams Selin

Department of Atmospheric Science

In partial fulfillment of the requirements

For the Degree of Doctor of Philosophy

Colorado State University

Fort Collins, Colorado

Fall 2012

Doctoral Committee:

Advisor: Richard Johnson

Susan van den Heever
Bogusz Bienkiewicz
Russ Schumacher

ABSTRACT

GRAVITY WAVE AND MICROPHYSICAL EFFECTS ON BOW ECHO DEVELOPMENT

Numerical simulations of the 13 March 2003 bow echo over Oklahoma are used to evaluate bow echo development and its relationship with gravity wave generation and microphysical heating profile variations. The first part of the research is directed at an explanation of recent observations of surface pressure surges ahead of convective lines prior to the bowing process. Multiple fast-moving $n = 1$ gravity waves are generated in association with fluctuations in the first vertical mode of heating in the convective line. The surface impacts of four such waves are observed in Oklahoma mesonet data during this case. A slower gravity wave is also produced in the simulation, which is responsible for the pre-bowing pressure surge in the model. This gravity wave is generated by an increase in low-level microphysical cooling associated with an increase in rear-to-front flow and low-level downdrafts shortly before bowing. The wave moves ahead of the convective line and is manifested at the surface by a positive pressure surge ahead of the convective line. The low-level upward vertical motion associated with this wave, in conjunction with higher-frequency gravity waves generated by the multicellularity of the convective line, increases the immediate pre-system CAPE by approximately 250 J kg^{-1}.

Two-dimensional heating profiles from this idealized, full-physics bow echo simulation are placed as a constant heat source in another simulation without moisture, to evaluate what type of gravity waves are produced by a heating profile from a given instance in time. A one-dimensional vertical mean heating profile is calculated from each two-dimensional profile, and a statistical method is used to evaluate the significance of each vertical mode. A number of gravity waves are produced in the dry simulation despite their vertical mode lacking

statistical significance in the one-dimensional profile, suggesting that horizontal variations in the heating profile are important to consider.

Microphysical sensitivity tests further elucidate the importance of the horizontal distribution of the microphysical heating profile. The tests used variations in the graupel parameter to evaluate its effect on bowing development and related forecasting parameters. Idealized and case study simulations showed that simulations using a larger, heavier, more "hail-like" graupel parameter with faster fallspeeds have decreased evaporation and melting rates concentrated closer behind the convective line, compared to simulations with a smaller, slower-falling, more "graupel-like" graupel parameter. This resulted in increased precipitation efficiency but a smaller stratiform region, weaker cold pool, weaker downdrafts and surface wind gusts, rear-to-front flow that remained elevated until close behind the convective line, and delayed bowing development in the "hail-like" simulations. Output from the case study sensitivity tests were compared to data from the Oklahoma Mesonet, which showed "hail-like" microphysical variations can cause significant variations in simulated forecasting parameters, including a 90 minute delay in onset of bowing, 150% weaker surface wind gusts, and a 600% increase in storm-total precipitation.

Results from this work emphasize the importance of microphysical heating and cooling profiles in development of bow echoes, be it through the generation of multiple gravity waves and their feedback to the convection, or through direct modification of convective features such as the rear-inflow circulation and the cold pool strength. The pressure surge gravity wave generated by low-level cooling prior to bowing, and associated destabilization of the environment immediately in advance of the system, improves understanding of the cause of convective intensification as the system bows. However, the strong connection shown between bow echo development and microphysical processes, and the highly diverse nature of microphysical parameterizations, presents a challenge to the prediction of these severe weather phenomena.

ACKNOWLEDGEMENTS

This research was supported by National Science Foundation Grant ATM-0500061, and portions of it were conducted under the Cooperative Research Data Agreement between the Air Force Weather Agency and Atmospheric Environmental Research, Inc. Oklahoma Mesonet data were provided through the courtesy of the Oklahoma Mesonet, a cooperative venture between Oklahoma State University and the University of Oklahoma and supported by the taxpayers of Oklahoma. NCEP/EMC 4-km Stage-IV data provided by NCAR/EOL under sponsorship of the National Science Foundation. The WSI NOWrad data were provided by the Mesoscale and Microscale Meteorology Division of the University Corporation for Atmospheric Research (UCAR) through David Ahijevych. Computing resources were provided by the Navy Department of Defense Supercomputing Resource Center (Navy DSRC) and the Army Research Laboratory Department of Defense Supercomputing Resource Center (ARL DSRC), which are sponsored by the DoD High Performance Computing Modernization Program.

George Bryan was very helpful explaining and discussing his Cloud Model 1. Morris Weisman and Kevin Manning provided excellent assistance in running and understanding the WRF model. The members of my graduate committee, as well as Steven Rutledge, have all offered constructive comments and helpful criticism on this work and the research preceding it. Particularly, Susan van den Heever has provided valuable insight and support. The members of the Johnson research group, both current and alumni, have been quite helpful. Thanks also go to David McDonald of the Air Force Weather Agency for a clear explanation of ordinal linear regression, as well as my employers at Atmospheric and Environmental Research, Inc., for flexibility and understanding.

My advisor, Richard Johnson, has not only provided crucial guidance, assistance, and criticism, but also has been kind and accommodating throughout the entire research process.

Finally, I would like to thank my husband, family, and friends, without whose answered prayers and unending support I would have neither sanity nor finished dissertation.

TABLE OF CONTENTS

Abstract ii

Acknowledgements iii

List of Tables viii

List of Figures ix

1 INTRODUCTION 1

2 LITERATURE REVIEW 4
2.1 Convectively-generated gravity waves 4
2.1.1 $n = 1$ gravity waves 4
2.1.2 $n = 2$ and 3 gravity waves 7
2.1.3 Higher-frequency gravity waves 9
2.2 Bow echo development 10
2.3 Microphysical effects on convection 12
2.3.1 Cold pool and system intensity 12
2.3.2 System precipitation structure 14
2.3.3 Precipitation coverage and amount 14

3 EXAMINATION OF ATMOSPHERIC WAVES ASSOCIATED WITH 13 MARCH 2003 BOW ECHO 16
3.1 13 March 2003 case review 16
3.1.1 Fast-moving low pressure perturbations 16
3.1.2 Pressure surge 19
3.2 Model description 22
3.3 Multiple $n = 1$ gravity waves 23
3.4 Pressure surge 29
3.4.1 Feature description 29
3.4.2 Low-level cooling source and effects 36
3.5 High-frequency gravity waves 40
3.6 Summary 42

4 EVALUATION OF MICROPHYSICAL PROFILES ACTING TO GENERATE GRAVITY WAVES 44
4.1 Methodology 44
4.1.1 Simulation descriptions 44
4.1.2 Statistical evaluation of heating profile 47
4.2 “Early” dry simulation 48
4.2.1 Wave identification and structure 48
4.2.2 Environmental effects 53

4.3 "Surge" dry simulation . . . 56
4.3.1 Wave identification and structure . . . 56
4.3.2 Environmental effects . . . 60
4.4 Summary . . . 61

5 IMPACT OF GRAUPEL PARAMETERIZATION SCHEMES ON IDEALIZED BOW ECHO . . . 63
5.1 Methodology . . . 63
5.1.1 Model description . . . 63
5.1.2 Model microphysics and experiment design . . . 65
5.2 Results from hail-graupel comparison . . . 69
5.2.1 System-relative rear-to-front flow . . . 71
5.2.2 Mid-level pressure and buoyancy perturbations . . . 73
5.2.3 Microphysical effects on bowing . . . 79
5.2.4 Comparison to other studies . . . 81
5.3 Results from removal of graupel class . . . 83
5.4 Summary . . . 93

6 QUANTITATIVE EVALUATION OF BOW ECHO MICROPHYSICAL SENSITIVITY . . . 94
6.1 Methodology . . . 94
6.1.1 Model setup . . . 94
6.1.2 Microphysics and experiment design . . . 96
6.1.3 Convective/stratiform area determination . . . 100
6.2 Case review . . . 101
6.3 Results from sensitivity tests . . . 103
6.3.1 Bowing initiation . . . 106
6.3.2 10-m wind gust speeds . . . 108
6.3.3 System speed . . . 112
6.3.4 Convective/stratiform areal coverage . . . 115
6.3.5 Accumulated precipitation . . . 120
6.4 Summary . . . 122

7 SUMMARY AND CONCLUSIONS . . . 124
7.1 Summary and discussion of presented results . . . 124
7.2 Suggested future work . . . 131

References . . . 134

LIST OF TABLES

4.1 Vertical modes in the "early" mean vertical heating profile determined to be significant at level of 99%. "Sign" of vertical mode explained in the text. . . 48
4.2 Simulated and predicated speeds of four wave modes in the first dry run simulation. Predicted speed calculated using the mean N of the profile, 7.8×10^{-3} s^{-1}. The mean wind speed in direction of wave motion, 3.1 m s^{-1}, was accounted for. 51
4.3 As in Table 4.1, but for the "surge" mean vertical heating profile. 56
4.4 As in Table 4.2, but for the second dry run simulation. The mean profile N was 8.7×10^{-3} s^{-1}. The mean wind in the direction of wave motion was 4.4 m s^{-1}. 59

5.1 Names of model simulations with the intercept value (n_{0G}), density (ρ_G), and fallspeed parameters (a_G, b_G) used in the hail/graupel comparison experiment, and graupel removal experiment. The default values in WSM6 are those of the "graupel" simulation. 66

6.1 Characteristics of the twelve unique microphysics configurations used in this chapter. Within the classes column, cw, ci, rw, sn, gr represent cloud water, cloud ice, rain water, snow, and graupel, respectively. ρ is environmental air density (kg m^{-3}); ρ_{850} the density of the standard atmosphere at 850 hPa (kg m^{-3}); q_G graupel mixing ratio (kg kg^{-1}); and N_G total concentration (m^{-3}). Mixing ratio is a prognostic value for all classes; total concentration is the second prognostic value for all double-moment classes. 99
6.2 Time bowing initiates; UTC 13 March 2003. 106
6.3 Times of arrival of simulated and observed convective line at Oklahoma Mesonet stations VANO and LANE, and system speed between the two. Times are UTC on 13 March 2003. 112

LIST OF FIGURES

2.1 (a-d): Signal of a 2.0 J kg^{-1} s^{-1} convective ($n = 1$) heating pulse of 2 h duration underneath a rigid lid at 10 km. (a) horizontal velocity (m s^{-1}); (b) vertical velocity (m s^{-1}); (c) perturbation pressure (Pa); (d) perturbation buoyancy (m s^{-2} $\times 10^2$). The heating source is at x=0 km. (e-h): As in (a-d), but the heating source is the combined $n = 1$ and $n = 2$ heating modes, of magnitude 1.0 J kg^{-1} s^{-1}, and is not turned off. From Nicholls et al. (1991). 6

2.2 Pressure perturbations at (a,c) 2 h and (b,d) 4 h into the simulations of Haertel and Johnson (2000) with a stationary (a,b) and moving (c,d) source of cooling. Contours every 0.4 hPa. In (c,d) the cool source is moving at 10 m s^{-1}. 8

2.3 Conceptual model from Fovell et al. (2006) showing the cool, moist tongue generated by a low-frequency gravity wave (a), and the "daughter clouds" generated within this layer by high-frequency gravity waves (b). 9

2.4 Conceptual model from Weisman (1992) portraying the relative strength of the vorticity associated with the low-level environmental shear, cold pool, and rear inflow jet. The convective updraft is shown by the thick arrow; the rear inflow jet by the thin arrow. In (a) the rear inflow jet descends to the surface far behind the convective line, producing a more tilted updraft. In (b) the jet remains elevated until shortly before the convective line, and the updraft is more upright. 11

3.1 WSI NOWrad base reflectivity from 0230 (a), 0345 (b), 0515 (c), 0545 (d), 0615 (e), and 0830 (f) UTC 13 March 2003. High-pass filtered potential temperature (purple, 1^{o}C), surface wind (black, barbs) and adjusted pressure (black, 0.5 hPa). The star is the KTLX radar, and the black dots in (a) are Mesonet stations VANO and HUGO. (From ASJ10.) 17

3.2 Timeseries display to high-pass filtered data from stations VANO (a) and HUGO (b) from the Oklahoma Mesonet (locations shown in Fig. 3.1a). Time increases to the left from 0300 to 0800 UTC 13 March 2003. Upper graphs in each figure show potential temperature (K, dashed, upper right scale) and adjusted pressure (hPa, solid line, upper left scale). Lower graphs show sustained winds (knots, barbs), sustained wind speed (m s^{-1}, solid line, lower left scale), unfiltered wind gusts (m s^{-1}, G, lower left scale), and unfiltered precipitation rate (mm (5 min)$^{-1}$, dashed line, lower right scale). [a] - [f] refer to indications of passing gravity waves or gravity current at each station and are referenced in the text. 18

3.3 Isochrones (grey, contoured every 30 min) for the features noted in Fig. 3.2 at arrows [a], [b], [c], [d], and [e], corresponding to figure (a), (b), (c), (d), and (e), here, respectively. Only stations where each feature was observed are included (some stations are omitted for display clarity). Times are displayed in decimal format (e.g., 4.33 is 0420 UTC 13 March 2003). 20

3.4 0000 UTC 13 March 2003 KOUN sounding. 23
3.5 Simulated reflectivity (filled contours, dBZ) and pressure perturbation (black, 0.5 hPa, negative dashed) for (a) 0:50 and (b) 1:50 simulation time. Black arrow in (b) points to the pressure surge discussed in Section 3.4. 24
3.6 Vertical x cross-section from 0-12 km, through the pressure surge, averaged 5 km about the x cross-section. Vertical wind speed (color, m s^{-1}) and pressure perturbation (black, 0.2 hPa, negative dashed). (a) 0:50 and (b) 1:35 simulation time. Upward and downward motion indicated by arrows; high and low pressure perturbations by "H" and "L". The wave in (a), and the rightmost wave in (b), are the same feature. 25
3.7 (a) Mean microphysical heating (K (1 min)$^{-1}$) between 5.2 and 7.3 km aloft and x=50 to 150 km (width of system), from 0:00 to 3:00 simulation time. Y-average calculated 5 km about the x cross-section. (b) Time evolution of horizontal distribution of vertical motion (m s^{-1}) at 6 km aloft, averaged 5 km about the x cross-section. Signature of the five gravity waves shown in Fig. 3.6, are denoted by black lines. Grey lines connect the time of initial generation of these waves to the heating rate. 27
3.8 Time evolution of horizontal distribution of CAPE (color, 45 J kg^{-1}), averaged 5 km about the x cross-section. Five thin black lines track the five gravity waves shown in Fig. 3.6. Thick dashed grey and black lines denote the pressure surge discussed in Section 3.4. Thin dashed black line tracks a cloud generated by a high-frequency gravity wave, discussed in Section 3.5. 28
3.9 Vertical 0-12 km x cross-section through pressure surge, averaged 5 km about the x axis at time of surge development, 1:55 simulation time. (a) Cloud water mixing ratio (color, 0.1 g kg^{-1}) and pressure perturbation (black, 0.25 hPa, negative dashed). (b) Vertical wind speed (color, m s^{-1}) and surface pressure perturbation (as in (a)). Convective line is at approximately x=120 km. The pressure surge is labelled. The vertical black arrows mark upward and downward motion. The black boxes outline the high-frequency wave signatures discussed in Section 3.5. 30
3.10 (a) Mean microphysical heating (K (1 min)$^{-1}$) between 1.8 and 2.2 km aloft, y=100.5 to 105.5 km (5 km about pressure surge), and the width of convective line. (b) Time evolution of surface pressure perturbation (hPa) averaged 5 km about the x cross-section. Thin black lines are as in Fig. 3.7b. The thick dashed black and grey lines show the progression of the pressure surge feature. 32

3.11 Time-height series of mean vertical profiles, created by averaging over the horizontal width of the system and pressure surge in the x-direction, and 5 km about the pressure surge and bow echo in the y-direction. Area averaged over shown in inset in (a); area moves with convective line. The positive and negative u wind averages were calculated separately. The thin black vertical line in each is the time of the start of the pressure surge. (a) Microphysical cooling rates due to evaporation (filled contours, K (5 min)$^{-1}$), melting (red, 0.01 K (5 min)$^{-1}$), and sublimation (purple, 0.02 K (5 min)$^{-1}$). (b) Storm-relative front-to-rear u wind (1.5 m s^{-1}). (c) Storm-relative rear-to-front u wind (1 m s^{-1}). (d) Maximum cold pool intensity (C, m s^{-1}). (e) Maximum upward vertical motion (1 m s^{-1}). (f) Maximum downward vertical motion (1.0 m s^{-1}). Labels [1] through [6] detail the bowing process and are discussed in the text. 35
3.12 As in Fig. 3.11, but for a non-bowing segment of the convective line, shown in inset in (a). 38
3.13 CAPE (color, J kg^{-1}) and pressure perturbation (black, 0.5 hPa, negative dashed) at 1:55 simulation time. 39
3.14 Vertical 0-12 km cross-section at 1:50 simulation time, averaged 5 km about x-axis, of the Scorer parameter (color, m^{-2}). Black box delineates the same area as in Fig. 3.9. 41

4.1 Vertical cross-sections of microphysical heating rate over the past 5 minutes (black, 1 K (5 min)$^{-1}$, negative dashed) and simulated radar reflectivity (dBZ). (a) from the full physics simulation at 0:40 simulation time; (b) from 1:50 simulation time. Both are averaged 10 km in the y-direction, about a cross-section through the area of the pressure surge discussed in the previous chapter. 45
4.2 Mean sounding profile from full physics simulation, over a 1 km box 5 km in advance of the pressure surge as it developed. 46
4.3 *Caption on following page.* 50
4.4 Hovmöller diagram of surface pressure (hPa) in the same x-cross-section as shown in Fig. 4.3. Four black lines mark the four gravity waves discussed in Fig. 4.3. The advancing cold pool is marked by the text "Gravity Current". . 52
4.5 As in Fig. 4.4, but of (a) CAPE (J kg^{-1}) and (b) CIN (J kg^{-1}). 54
4.6 *Caption on following page.* 55
4.7 As in 4.6, but from 2:00 into the surge dry simulation. Thick black lines are now the $n = 4$, 3, and 2 gravity waves, at x=178, 211, and 267 km, respectively. 57
4.8 As in Fig. 4.4, but for the second dry run simulation. 60
4.9 As in Fig. 4.5, but of CAPE (J kg^{-1}) for the second dry run simulation. . . . 61

5.1 (a) Graupel hydrometeor size distributions for the model runs given in Table 1. This assumes a graupel mixing ratio of 1 g kg^{-1} and air density of 1 kg m^{-3}. (b) Mass-weighted mean graupel hydrometeor terminal velocity (m s^{-1}) for a range of graupel mixing ratios (kg kg^{-1}) as a function of four different schemes. Temperature is fixed at 268.15 K, and pressure at 900 hPa. The "fast graupel" fallspeed is equivalent to that of the "hail-like" system. The Morrison fallspeed uses the single-moment Morrison scheme described in Bryan and Morrison (2012). 67
5.2 Simulated composite reflectivity for the "graupel-like" (a), "mid" (b), "hail-like", and (d) "fast graupel" systems as they each begin to bow, at 2:40, 2:50, 3:00, and 2:20 simulation time, respectively. Thick black lines delineate bowing segments. Thin black lines show location of later vertical cross-section figures. Simulated composite reflectivity calculated as in Stoelinga (2005), but modified to use the WSM6 scheme's temperature-dependent snow intercept parameter. 70
5.3 0-6 km vertical cross-sections of the "graupel-like" (a), "mid" (b), "hail-like" (c), and "fast graupel" (d) systems, at the time each developed significant system-relative rear-to-front flow: 2:30, 2:35, 2:45, and 2:20 simulation time, respectively. These cross-sections are taken along the black line shown in Fig. 5.2; plotted values are averages 5 km either side of the cross-section. Simulated reflectivity (color) and storm-relative line-normal winds in the plane of the cross-section (black contours, 4 m s^{-1}, negative dashed) are shown. . . 72
5.4 Mixing ratios (g kg^{-1}) are of graupel (color), cloud water and ice (red, 0.5 g kg^{-1}), rain water (green, 0.5 g kg^{-1}), and snow (thin black, 0.5 g kg^{-1}); the thick solid black lines are cold pool potential temperature perturbation contours every 2 K. Thin dashed black line is the melting level. Vertical cross-sections as in Fig. 5.3, but from 0 to 12 km. 74
5.5 Cooling rates (K $(5\ min)^{-1}$) of evaporation (blue image), melting (red, 0.6K $(5\ min)^{-1}$), and sublimation (purple, 0.6K $(5\ min)^{-1}$). Thick solid black lines are the simulated reflectivity at 25, 40, and 50 dBZ. Thin dashed black line is the melting level. Vertical cross-sections as in Fig. 5.4. 75
5.6 Vertical motion (color, cm s^{-1}) and relative perturbation pressure (black, 0.5 hPa, negative dashed). Perturbation pressure was calculated by subtracting the mean total domain pressure profile from the total pressure field. These cross-sections are a 60-km subset of the cross-sections shown in Fig. 5.4. The black arrows in each figure point to the low pressure perturbation discussed in the text. The brackets show the total tilt of the convective updraft over heights from 0 to 6 km. 76
5.7 *Caption on following page.* 77
5.8 Simulated composite reflectivity from the "graupel" (a,b,c) and "no graupel" (d,e,f) simulations. Columns, from left to right, correspond to times 2:35 (a, d), 3:10 (b, e), and 4:45 (c, f). Simulated reflectivity calculated as in Fig. 5.2. Thin black lines delineate location of cross-sections in subsequent figures. Thick black lines show development of bowing segment. 84

5.9 Mixing ratio cross-sections from the "graupel" (left column) and "no-graupel" (right column) simulations, at 2:35 (a, b), 3:30 (c, d), and 4:45 (e, f) from cross-section lines shown in Fig. 5.8. Contour values identical to Fig. 5.4. No color in (b), (d), and (f) as they lack graupel. 85
5.10 Microphysical cooling cross-sections from the "graupel" (left column) and "no-graupel" (right column) simulations, at 2:35 h (a, d), 3:10 h (b, e), and 4:45 (c, f) from cross-section lines shown in Fig. 5.8. Contour values identical to Fig. 5.5. 86
5.11 Storm relative wind vertical cross-sections from the "graupel" (left column) and "no-graupel" (right column) simulations, at 2:35 (a, b), 3:30 (c, d), and 4:45 (e, f) from cross-section lines shown in Fig. 5.8. Contour values identical to Fig. 5.3. 87
5.12 Vertical motion and relative pressure perturbation cross-sections from the "graupel" (left column) and "no-graupel" (right column) case study simulation, at 2:35 (a, d), 3:10 (b, e), and 4:45 (c, f). Perturbation pressure was calculated by subtracting the mean domain pressure profile from the total pressure field. Contour values, arrows, an brackets identical to Fig. 5.6. These cross-sections are a 65-km subset of the cross-sections shown in Fig. 5.9. 89
5.13 Comparison of "no-graupel" (blue) and "graupel" (red) simulations from 1 to 6 h simulation time within the convective line. (a) maximum cold pool intensity (C, m s^{-1}), (b) maximum z-wind updraft (m s^{-1}), and (c) maximum z-wind downdraft (m s^{-1}). Maximum and minimum values are calculated at 5-minute intervals. The two thick grey lines are the times new bowing development initiates in the "no graupel" and "graupel" simulations (2:35 and 3:30, respectively). 90

6.1 WRF-ARW domain. The entire domain was run in 3-km resolution. Later figures will show only a subsection of the domain over eastern Oklahoma for space considerations. 95
6.2 (a) Graupel hydrometeor distributions for the microphysics schemes examined that have a graupel class. This assumes a graupel mixing ratio of 1 g kg^{-1} and air density of 1 kg m^{-3}. Within the Morrison scheme, bounds are placed on the distribution slope; the largest and smallest values allowed are shown here. (b) Mass-weighted mean graupel hydrometeor terminal velocity (m s^{-1}) for a range of graupel mixing ratios (kg kg^{-1}). The WDM6 mean terminal velocity is very similar to the WSM6 "graupel-like" modification. The two Morrison terminal velocity functions represent the two bounds on the graupel distribution function, shown above. Temperature is fixed at 268.15 K, and pressure at 900 hPa. Calculations for "graupel-like", "mid", and "hail-like" are as in Chapter 5. 97
6.3 0315 UTC (a), 0500 UTC (b), 0600 UTC (c), and 0730 (d) 13 March 2003 WSI NOWrad composite radar reflectivity data. Oklahoma Mesonet stations VANO, LANE, and HUGO are displayed from northwest to southeast, respectively, as black dots in (a). 102

6.4 Composite reflectivity, from the KTLX radar (a) and model-simulated (b-k) at the time of bowing initiation of each system (see Table 3 for times of bowing initiation). 104
6.5 Minimum surface buoyancy (m s^{-2}) of the cold pool associated with the simulated and observed (using the Oklahoma Mesonet) convective systems. . . . 105
6.6 10-m wind gust speed (m s^{-1}), from simulations and observed from Oklahoma Mesonet, 30 min after bowing initiation of each system (see Table 3 for times of bowing initiation). Wind gust speed calculated as in the Unified WRF Post-Processor (UPP). 109
6.7 Maximum 10-m wind gust within simulated or observed system (using Oklahoma Mesonet). Wind gust speed calculated as in Unified WRF Post-Processor (UPP). 110
6.8 Area (in 1000 km^2) of stratiform (a) or convective (b) precipitation, either observed (via KOUN radar) or simulated, over the course of the system's lifecycle. Convective precipitation was assumed to have reflectivity values of 45 dBZ or larger; stratiform precipitation greater than 0 dBZ but less than 45 dBZ. Additional discussion on these calculation is provided in Section 2c. 116
6.9 Total system accumulated precipitation (mm) for each simulated system and observations (calculated using Oklahoma Mesonet). Precipitation from extraneous simulated convection in northeast Oklahoma is masked out. 119

CHAPTER 1
INTRODUCTION

A bow echo, or "bow-shaped line of convective cells that is often associated with swaths of damaging straight-line winds and small tornadoes" (American Meteorological Society 2000), is an important meteorological and forecasting phenomenon. The convective feature's close association with severe winds and strong downbursts is so well-documented (Fujita 1978; Johnson and Hamilton 1988; Houze et al. 1989; Evans and Doswell 2001; Klimowski et al. 2003) that it is included in the American Meteorological Society's definition of the term. Understanding the development of these bowing features is key to being able to forecast them and their associated severe weather correctly.

Adams-Selin and Johnson (2010), hereafter ASJ10, noted surface pressure and temperature patterns associated with an Oklahoma bow echo that appeared to correspond to gravity waves generated by the heating profile of the convective system. One specific pressure feature observed by ASJ10, a surge of the mesohigh partially ahead of the convective line, appeared in conjunction with new bowing in 35 of 39 bow echoes observed in Oklahoma over the 4-year study, suggesting a connection to bowing development. Because that study only dealt with surface observations, neither the vertical structure nor the generating mechanism of these features could be confirmed. Given the strong correlation of the pressure surge with new bowing development observed in ASJ10, it is possible that the surge is related to the mechanism generating new bowing development, and could feed back to the newly bowing system in some way.

Numerous gravity waves have been associated with convection and its heating profiles in the literature, including a wave linked to the first internal mode of heating, or the convective heating profile (Nicholls et al. 1991; Mapes 1993). ASJ10 observed a surface pressure pattern associated with an Oklahoma bow echo that appeared to be a reflection of this type of wave,

but this result also could not be fully confirmed. Higher wave modes have also been simulated in conjunction with convection by Nicholls et al. (1991), Mapes (1993), Lane and Reeder (2001), Fovell (2002), and Fovell et al. (2006). However, the heating profiles associated with bow echoes have not been evaluated in the context of gravity wave generation. The environmental changes effected by these gravity waves, and the possible effects on bow echo development, have also not been studied.

While heating profiles within a convective system do generate gravity waves that can indirectly affect the system, they can also have a more direct effect. For example, it is well known that a key component of the strength, structure, and longevity of bow echoes is the cold pool (Rotunno et al. 1988; Weisman et al. 1992, 1993; Weisman and Rotunno 2005). Changes in the rates of cooling through variations in the microphysical processes have a large effect on the shape and strength of the cold pool (Lin et al. 1983; Fovell and Ogura 1988; James et al. 2006), and hence the eventual bow echo structure and development. While the impact of microphysical scheme variations on cold pool and storm structure have been noted for supercells (Gilmore et al. 2004a; van den Heever and Cotton 2004, 2007; Dawson et al. 2010; Snook and Xue 2008; Lerach et al. 2008), and squall lines (Nicholls 1987; Tao and Simpson 1989; Fovell and Ogura 1988; Szeto and Cho 1994; Morrison et al. 2009; Bryan and Morrison 2012), few, if any, studies have looked at the effects on development and maintenance of bow echoes.

Many of the studies of convective microphysical effects were idealized simulations only. Those that did focus on simulations initialized with real data were primarily interested in either longer-term statistical verification (Jankov et al. 2005; Liu and Moncrieff 2007; Schwartz et al. 2010), or the individual dynamics occurring within that case study (McCumber et al. 1991; Luo et al. 2010; van Weverberg et al. 2011a). Little research has focused on the effect of these microphysical variations on operationally forecasted fields, particularly in comparison to observations.

Thus, the goal of this work is to evaluate the effects of microphysical heating profiles,

and variations thereof, on bow echo development. Changes in the heating profile can result in generation of gravity waves and multiple feedbacks to the convective system. Those same microphysical changes can also directly modify the shape or strength of the cold pool, resulting in additional system adjustments. Understanding these connections will aid in understanding new bowing development.

Chapter 2 will review the current literature, with a focus on both gravity wave generation and microphysical variations. An idealized simulation of the case examined in ASJ10 is performed in Chapter 3, and the resulting gravity waves in that simulation are examined for their similarity to the observed pressure features. A journal article summarizing this study will be submitted to *Monthly Weather Review* shortly. Two dry simulations are performed in Chapter 4, using the microphysical heating profiles observed in Chapter 3, to clarify the vertical structure of the generated waves and their individual effect on the pre-storm environment; a journal article is being prepared from the study in this chapter. In Chapter 5, the microphysical heating profile of a bow echo is modified by changing the graupel parameterization within the simulation's microphysics scheme, and the resulting effects on bowing are detailed. *Monthly Weather Review* has conditionally accepted an article exploring this study. These variations are performed again in Chapter 6 but in a case study simulation initialized using a real data analysis. The subsequent variations are quantified and compared to observations from the Oklahoma Mesonet. These results are discussed in an article that will be submitted to *Weather and Forecasting* presently. Finally, conclusions are presented in Chapter 7.

CHAPTER 2
LITERATURE REVIEW

2.1 Convectively-generated gravity waves

The ability of convective systems to generate gravity waves is well-documented in the literature (Nicholls et al. 1987; Bretherton and Smolarkiewicz 1989; Schmidt and Cotton 1990; Mapes 1993; Fovell 2002, 2006; Knupp 2006). Specifically, changes in heating and cooling rates in the atmosphere, as are often found with convection, can result in the generation of gravity waves due to the difference in buoyancy between the convection and the surrounding environment (Bretherton and Smolarkiewicz 1989; Nicholls et al. 1991; Mapes 1993). If the vertical heating profile is a harmonic of the depth of the troposphere, the partial reflection of the wave energy at the tropopause allows these hydrostatic waves to propagate horizontally for large distances without the aid of a trapping level other than the tropopause (Nicholls et al. 1991). Such a wave is labelled by the number of antinodes in the heating profile that generates it; for example a $n = 1$ mode wave is generated by a heating profile that extends throughout the troposphere with its maximum at mid-levels.

Few studies have recorded real-world observations of these hydrostatic waves. Bryan and Parker (2010) observed a $n = 1$ wave moving quickly ahead of an Oklahoma squall line, and ASJ10 noted multiple surface pressure features that appeared to be associated with gravity waves. Chapters 3 and 4 evaluate the ASJ10 pressure features, using an idealized simulation to determine the vertical structure and cause of the observed surface pressure features.

2.1.1 $n = 1$ gravity waves

An $n = 1$ warming vertical temperature profile is typical during the formation of a convective line due to the latent heat release from condensation, freezing, and deposition in the updraft (Houze 1982; Johnson and Young 1983; Gallus and Johnson 1991). The speed of these low

frequency waves is given by:

$$c = \frac{NH}{n\pi} \tag{2.1}$$

where N is the Brunt-Väisälä frequency, H is the vertical depth of the atmosphere, and n is the vertical mode of the heating profile (Nicholls et al. 1991). In this study, the N used is the N_m defined in Bryan and Rotunno (2009). For subsaturated air, N_m is defined as

$$\left(\frac{g}{\theta_v}\right)\frac{\partial \theta_v}{\partial z} \tag{2.2}$$

where g is gravitational acceleration, z height, $\theta_v = \theta(1 + q_v R_v/R_d)/(1 + q_v + q_l)$, q_v and q_l the water vapor and liquid water mixing ratios, and R_d and R_v the gas constants for dry air and water vapor, respectively. The full description of N_m for saturated air is given in Bryan and Rotunno (2009). Typical values of N (0.01 s^{-1}) and H (10 km) yield a $n = 1$ wave speed of approximately 30 m s^{-1}.

Nicholls et al. (1991) calculated the linear atmospheric response to the introduction of a $n = 1$ warming temperature profile (Fig. 2.1a-d). In that study, the heat source, located at x=0 km, was turned on immediately at the the start of the solution, left on for 2 hours, and then turned off. The switch "on" of the heat resulted in a temporary low (high) pressure perturbation at the surface (aloft), along with an increase in the u wind flow toward the heating source at lower levels, and away from the heating source at upper levels (at x=450 km in Figs. 2.1a,c; also noted by Mapes 1993). An increase in potential temperature particularly at mid-levels also occured, generated by subsidence throughout the column following passage of the first wave front (Figs. 2.1b,d). At the surface, this appears as a temporary decrease in pressure unaccompanied by a change in temperature. When the heating ceased, a second signal traveled at the same speed away from the system. This second response contained ascent throughout the column, and the pressure, potential temperature, and u wind fields returned to the ambient values (Fig. 2.1a-d at x=225 km).

Within the idealized analytical solution of Nicholls et al. (1991), the ambient environment

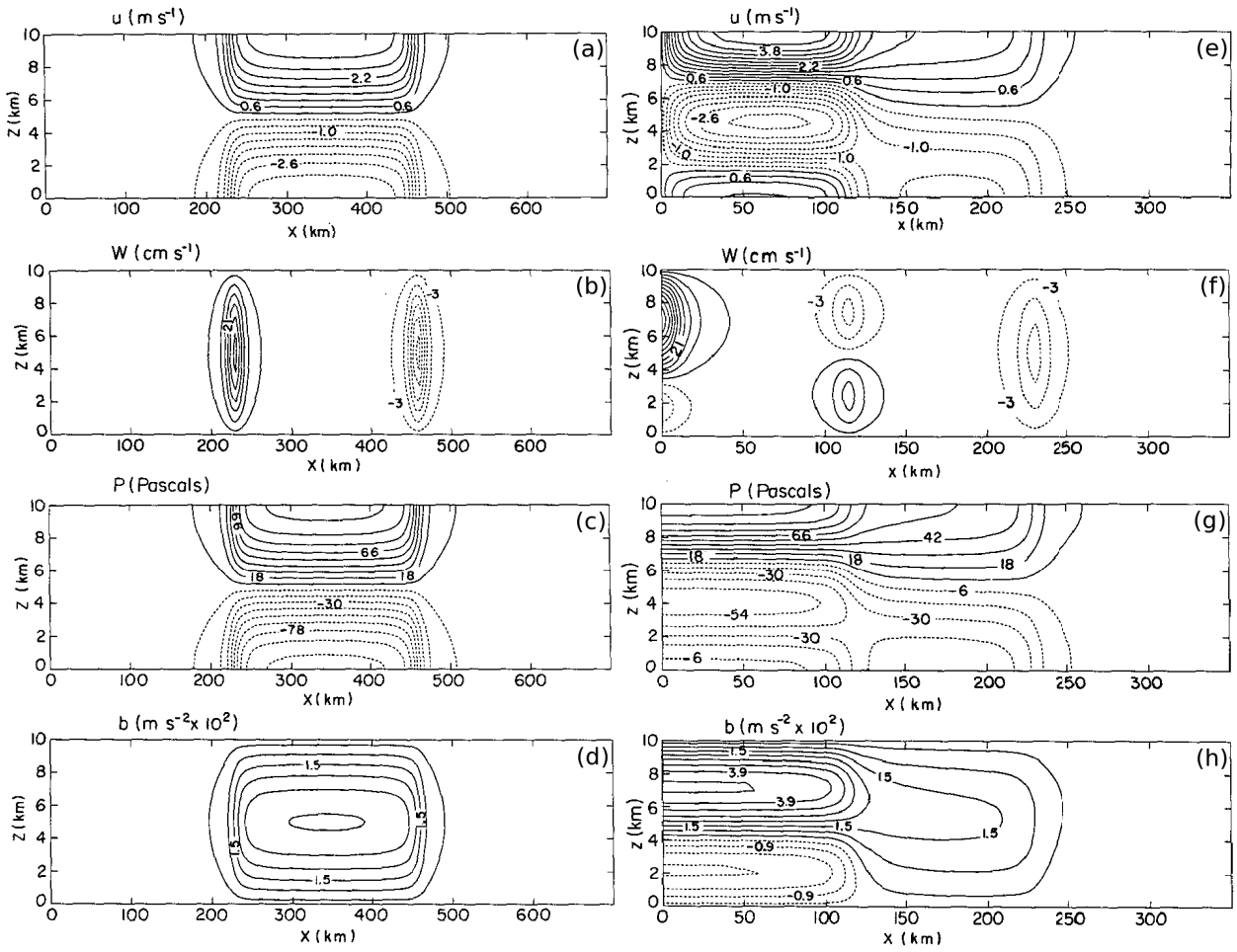

Figure 2.1: (a-d): Signal of a 2.0 J kg^{-1} s^{-1} convective ($n = 1$) heating pulse of 2 h duration underneath a rigid lid at 10 km. (a) horizontal velocity (m s^{-1}); (b) vertical velocity (m s^{-1}); (c) perturbation pressure (Pa); (d) perturbation buoyancy (m s^{-2} $\times 10^2$). The heating source is at x=0 km. (e-h): As in (a-d), but the heating source is the combined $n = 1$ and $n = 2$ heating modes, of magnitude 1.0 J kg^{-1} s^{-1}, and is not turned off. From Nicholls et al. (1991).

returns to its initial state after both responses pass. However, it was noted by Mapes (1993) that the pre-storm environment is permanently modified, even after both responses pass, due to the overall net heating produced by the convective system. The subsidence-induced slight warming and drying throughout the depth of the atmosphere resulting from the first response is a permanent modification, particularly in the mid-levels.

2.1.2 $n = 2$ and 3 gravity waves

The heating profile generated by a system's stratiform precipitation region, of $n = 2$ or even $n = 3$ structure consisting partially of cooling in low levels, can generate yet another low-frequency gravity wave (Nicholls et al. 1991; Mapes 1993; Lane and Reeder 2001; Fovell 2002; Fovell et al. 2006). In the $n = 2$ wave, upward (downward) motion is excited throughout the lower (upper) half of the troposphere; the lower half of the troposphere is adiabatically cooled (Fig. 2.1f,h at approximately x=120 km). The wind profile is modified to create mid-tropospheric inflow (Fig. 2.1e, Fovell 2002); a mid-tropospheric low pressure perturbation is created as well, with high pressure perturbations generated in the lowest and highest third of the troposphere (Fig 2.1g). Through (2.1), it can be seen that this wave moves at half the speed of the $n = 1$ wave. Pandya and Durran (1996)and Pandya et al. (2000) found that the wind perturbations generated by the combination of $n = 1$ and 2 gravity waves could largely explain the circulations within a squall line, including the onset of rear-to-front flow.

The $n = 3$ wave also exhibits a lifting and cooling response, but over the lowest third of the atmosphere (Lane and Reeder 2001). The $n = 3$ cooling profile is typically associated with the onset of melting contributing to a low-level cooling maximum. While both $n = 2$ and $n = 3$ wave modes cool and moisten the lower levels, Lane and Reeder (2001) found that the $n = 3$ wave had a more significant effect in decreasing the pre-storm environment convective inhibition (CIN). This is because the peak upward vertical motions associated with this wave were located lower, closer to the sub-cloud layer, a major determinant of CIN. Combinations of the $n = 2$ and $n = 3$ waves can act as positive feedbacks to their generating systems, cooling and moistening the lower level air feeding into the storm and organizing surrounding convection (Schmidt and Cotton 1990; Mapes 1993; McAnelly et al. 1997; Lane and Reeder 2001; Fovell 2002; Fovell et al. 2006; Lane and Moncrieff 2008; Bryan and Parker 2010; Lane and Zhang 2011).

Heating profiles that are not harmonics of the depth of the troposphere also generate gravity wave responses similar in appearance to those discussed above. With reduced op-

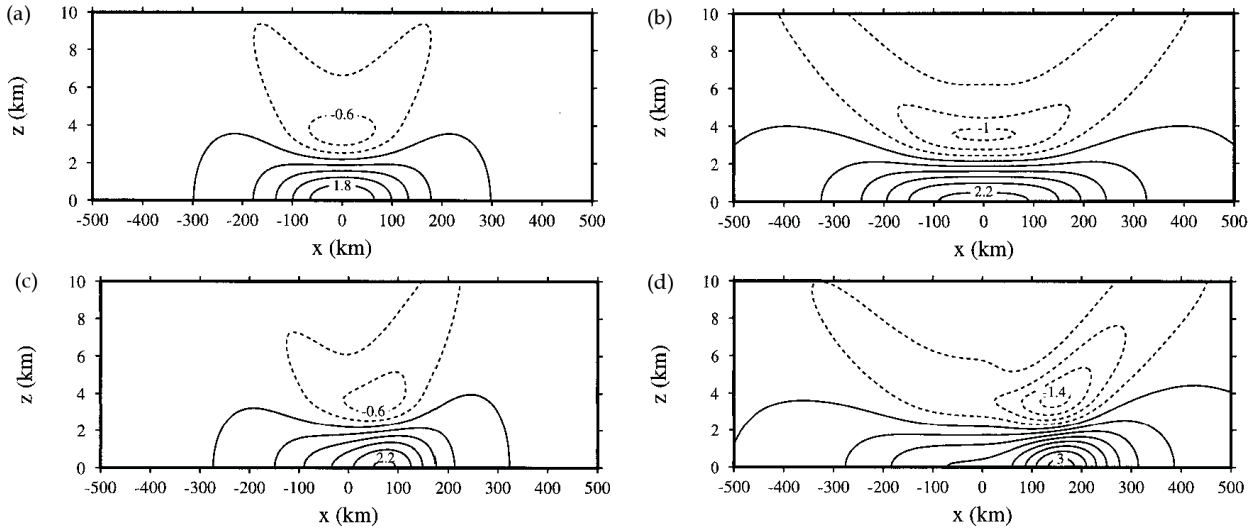

Figure 2.2: Pressure perturbations at (a,c) 2 h and (b,d) 4 h into the simulations of Haertel and Johnson (2000) with a stationary (a,b) and moving (c,d) source of cooling. Contours every 0.4 hPa. In (c,d) the cool source is moving at 10 m s^{-1}.

portunity for reflection these waves can quickly propagate vertically out of the troposphere, but that is not always the case: gravity wave responses to low-level cooling were produced in Parker (2008) and Schumacher (2009) that remained near the surface. In idealized linear simulations by Haertel and Johnson (2000), hereafter HJ00, they found the gravity wave response to cooling over the lowest 4 km of the troposphere results in a prominent pressure signal at the surface 6 hours into the simulation. This response was in addition to the features associated with the also-generated gravity current. Furthermore, if the cooling source moves at a speed approximately equal to that of its generated wave, the wave response is amplified. Fig. 2.2 displays the pressure perturbations observed in the HJ00 simulation with stationary and moving sources of cooling, at 2 and 4 h into the simulation. Between 2 and 4 h, the positive surface pressure perturbation grew from 20 to 35% larger in magnitude when the cooling source moved at a speed close to that of the wave as opposed to remaining stationary.

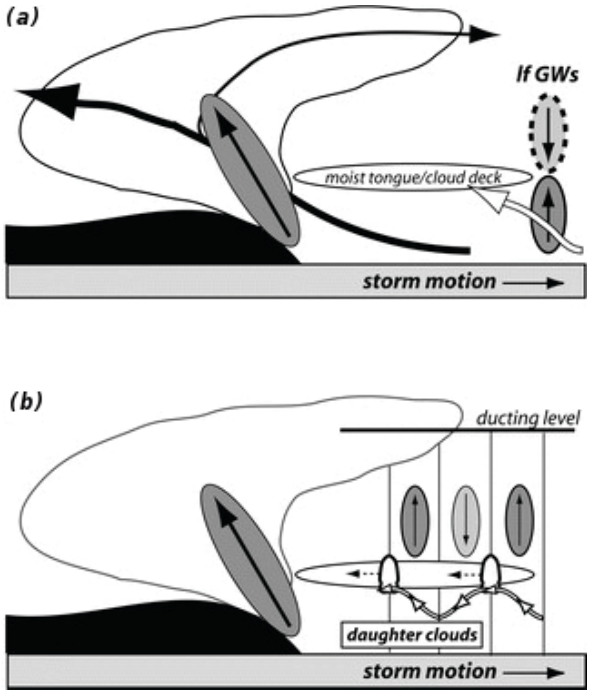

Figure 2.3: Conceptual model from Fovell et al. (2006) showing the cool, moist tongue generated by a low-frequency gravity wave (a), and the "daughter clouds" generated within this layer by high-frequency gravity waves (b).

2.1.3 Higher-frequency gravity waves

Finally, Fovell et al. (2006) noted that high-frequency, non-hydrostatic gravity waves propagating in the troposphere ahead of a squall line can be generated by multicellular development and frequent temporal changes of the heating profile within a convective line. These waves do require a trapping layer to not quickly propagate out of the troposphere; the curvature of the wind profile due to outflow aloft from the system at anvil level can provide this. They found that small amounts of water condensed within the updrafts associated with these high-frequency waves, increasing the parcel's buoyancy, and small clouds formed (Fig. 2.3b). This particularly can occur if the lower levels have previously been lifted, cooled, and moistened by a low-frequency gravity wave (Fig. 2.3a). The newly formed clouds are then advected toward the main system by the system-relative wind. As the clouds are ingested by the system, the increase in buoyancy can act to locally strengthen the convective line, provided the cloud has not already developed rainfall and its own associated cold pool (Fovell et al. 2006).

2.2 Bow echo development

Multiple studies (Hane 1973; Thorpe et al. 1982; Nicholls et al. 1988; Rotunno et al. 1988) have noted a relationship between the tilt of the convective updraft and the balance between vorticities generated at the front edge of the cold pool and by the environmental wind. When these two vorticity sources are balanced, the convective updraft remains upright, and stronger, by virtue of low-level air being lifted into the upper levels over a shorter distance. This does not necessarily translate to system longevity (Fovell and Ogura 1989; Lafore and Moncrieff 1989) but has been related to system intensity (Rotunno et al. 1988; Weisman and Rotunno 2004; Bryan et al. 2006; Parker 2010), although some studies question even that (Stensrud et al. 2005). When the cold pool and its associated vorticity strengthens, the updraft tilts rearward over the cold pool (Rotunno et al. 1988). The buoyancy gradient between it and the warm outflow from the updraft aloft increases, resulting in a strengthened mid-level low pressure perturbation (Garner and Thorpe 1992; Weisman and Rotunno 2005).

Lafore and Moncreif (1989) and Weisman (1992) found that rear-to-front flow, or the rear inflow jet, in the system at mid- and low-levels forms in response to this mid-level buoyancy and pressure gradient; more recent studies have found this flow to be generated by a rearward-propagating gravity wave generated by low-level microphysical cooling (Pandya and Durran 1996; Pandya et al. 2000). Given a large stratiform region or intense cold pool, the rear inflow jet descends to the surface gradually, farther behind the convective line (Fig. 2.4; Weisman 1992); the farther the microphysical cooling extends behind the convective line, the farther rearward the rear inflow descends to the surface (Pandya and Durran 1996; Pandya et al. 2000). As a result the positive vorticity source associated with the back bottom edge of the cold pool is minimal, and the updraft is allowed to tilt further rearward over the cold pool. Systems in which the rear inflow is largely surface-based are expected to develop more quickly and create bowing segments, but are not anticipated to be as long-lived (Weisman 1993). Conversely, systems with elevated rear inflow generate

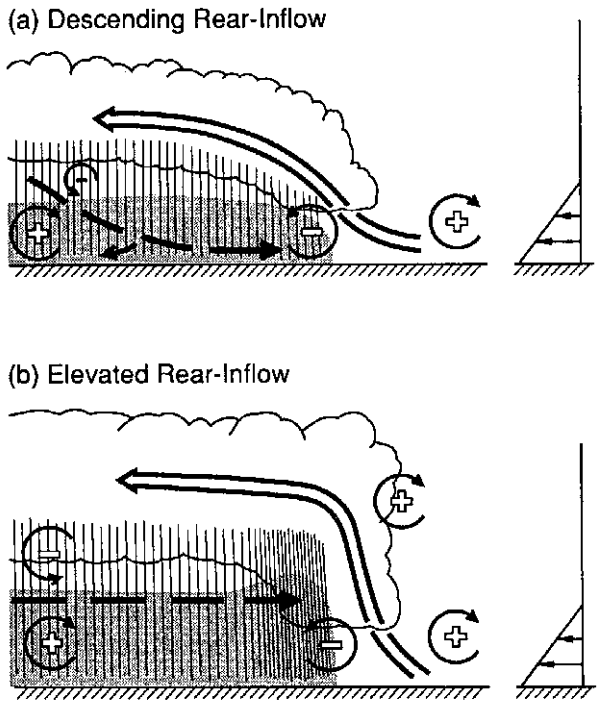

Figure 2.4: Conceptual model from Weisman (1992) portraying the relative strength of the vorticity associated with the low-level environmental shear, cold pool, and rear inflow jet. The convective updraft is shown by the thick arrow; the rear inflow jet by the thin arrow. In (a) the rear inflow jet descends to the surface far behind the convective line, producing a more tilted updraft. In (b) the jet remains elevated until shortly before the convective line, and the updraft is more upright.

additional positive vorticity that can balance the negative vorticity generated by the cold pool, aiding a more upright updraft (Weisman 1992).

A temporary, local intensification of the cold pool and its associated vorticity can result in only a portion of the storm updraft temporarily tilting farther upshear (Lafore and Moncrieff 1989; Weisman 1993; Weisman and Rotunno 2005; James et al. 2006). This additional tilt allows horizontal momentum within the system rear-to-front flow to be more easily transported to the surface, resulting in damaging downburst winds. These winds enhance evaporation by entraining additional unsaturated air, further cooling the cold pool. The combination of additional horizontal momentum and a more intense cold pool acts to locally increase the speed of the convective line, resulting in development of a bowing segment within the convective line (Weisman 1993; Weisman and Rotunno 2005; James et al. 2006).

2.3 Microphysical effects on convection

2.3.1 Cold pool and system intensity

Changes in the microphysical characteristics, through changes in heating and cooling rates, can have a large effect on the cold pool and resulting vorticity balances. The importance of the inclusion of ice in convective squall line simulations has been noted multiple times in the literature: the additional intensification of the updraft due to latent heat from freezing is required to best simulate the updraft strength and resultant system front-to-rear flow (Nicholls 1987; Tao and Simpson 1989; Fovell and Ogura 1988; Szeto and Cho 1994). Simulations that include ice have a larger and more realistic stratiform precipitation structure (Fovell and Ogura 1988). Cooling by melting also contributes significantly to the cold pool strength, and hence the mid-level thermal and pressure gradients in the stratiform region (Chen and Cotton 1988; Szeto and Cho 1994). This also enhances the speed of the rear inflow jet. Yang and Houze (1995) performed a simulation which included a hail parameter, in addition to cloud ice. They noted a much narrower stratiform precipitation region, weaker mid-level buoyancy and pressure perturbation, and resulting weaker rear inflow jet with the inclusion of hail.

The cold pool in simulations with ice was much stronger due to additional cooling by melting, thereby producing more intense convection and a faster system (Fovell and Ogura 1988; Szeto and Cho 1994). Replacing the graupel class with a hail class in other squall line simulations resulted in a much smaller stratiform region due to faster particle fallspeeds (Yang and Houze 1995; Luo et al. 2010; Morrison and Milbrandt 2011; Bryan and Morrison 2012). The faster fallspeeds also meant less time for melting and evaporation, and thus reduced cooling rates and a weaker cold pool, and correspondingly slower system (Szeto et al. 1988; Szeto and Cho 1994; Adams-Selin et al. 2012).

Multiple studies have been performed examining the effects of using graupel or hail as the rimed frozen species in addition to snow and cloud ice. In Bryan and Morrison (2012), a

hail squall line simulation produced a much narrower convective line with higher simulated reflectivities and a slightly smaller stratiform region, compared to the graupel simulation. Seigel and van den Heever (2012) noted increased rear-to-front and front-to-rear flows in simulations with smaller, less dense hail. van den Heever and Cotton (2004) and Cohen and McCaul (2006) found simulations with larger, denser hail resulted in weaker cold pools due to decreased evaporation and melting from hydrometeors with a faster fall speed and reduced surface area to volume ratio. Conversely, van Weverberg et al. (2011a) and (2012) and Milbrandt and Morrison (2011) found the opposite: because of the faster hail fallspeed, the downward precipitation flux was higher and consequentially the melting rate larger. Melting also extended to the surface instead of being confined to just below the melting level; this created a stronger surface cold pool. Gilmore et al. (2004a) found these results may be time dependent - their more graupel-like simulations' cold pools became coldest only late in the 2 h simulation; van Weverberg (2011b) noted a dependency on updraft strength.

Changes in simulated microphysical heating and cooling rates can also be affected by the use of a one- or two-moment microphysics scheme. In a one-moment scheme, only one distribution variable can be explicitly predicted; this is almost always the hydrometeor mixing ratio. In a two-moment scheme, typically the hydrometeor mixing ratio and number concentration are prognostic. Multiple studies evaluating the differences between these schemes in both squall line and supercell simulations have been performed; these studies also note the large effects changes in the heating and cooling profile of a system can have (Morrison et al. 2009; Dawson et al. 2010; Bryan and Morrison 2012; van Weverberg et al. 2012). Through the variation in particle number concentration allowed by the double-moment scheme, particularly that of rain and graupel (van Weverberg et al. 2012), evaporation rates were reduced due to changes in the total particle surface area, resulting in a weaker system cold pool. Within squall lines, this effect was largely evident in the stratiform region (Bryan and Morrison 2012).

Thus, variations in the ice parameters of a microphysical parameterization scheme can

have large effects on system heating and cooling profiles and cold pool strength, among other factors. Additionally, cold pool strength and rear inflow play a large role in new bowing development. To this point, however, there have been no studies linking new bowing development to variations in microphysics schemes. Therefore, a cloud-resolving model is used to examine the impacts of microphysics specifically on bow echoes. The sensitivity of new bowing frequency and intensity to changes in microphysical heating and cooling rates will be investigated, particularly through their relation to cold pool strength and depth, rear-to-front flow within the system, and the stratiform region microphysical structure.

2.3.2 System precipitation structure

Microphysics variations have many implications beyond the strength of the cold pool. For example, the inclusion of ice as a microphysics class produced a more realistic stratiform precipitation region in both size and intensity in multiple squall line simulations (Nicholls 1987; Tao and Simpson 1987; Fovell and Ogura 1988; Szeto and Cho 1994). In Bryan and Morrison (2012), a hail squall line simulation produced a much narrower but more intense convective line, with a slightly smaller stratiform region, compared to the graupel simulation. van den Heever and Cotton (2004) noted supercell type, such as classic or high precipitation, was determined by changes in the mean hail diameter.

2.3.3 Precipitation coverage and amount

Total accumulated precipitation is also strongly affected by the characteristics of the microphysics scheme utilized. Johnson et al. (2011) found that for short-term forecasts (less than 12 h) changes in the microphysics parameterization affected simulated precipitation more than either boundary layer parameterization or model dynamic core. Precipitation seems particularly sensitive to changes to the graupel (or hail, depending on the scheme) class characteristics; changes to this parameter produced the largest resultant variations in total precipitation in previous studies (Gilmore et al. 2004a; van Weverberg et al. 2011a). Fovell

and Ogura (1988) noted that at least in 2D simulations, melting graupel/hail was the largest source of rainwater.

When microphysics schemes with graupel only were used in squall line simulations, a significant decrease in precipitation efficiency and accumulation resulted in comparison to simulations with only hail (McCumber et al. 1991; Luo et al. 2010; Morrison and Milbrandt 2011; Bryan and Morrison 2012). The total precipitation coverage, however, increased in area, in both squall line and supercell simulations (van den Heever and Cotton 2004; Gilmore et al. 2004a; van Weverberg et al. 2011b). This result was even more highlighted with microphysics schemes that do not have graupel as a frozen precipitation class; the slow snowflake terminal velocities resulted in very widespread, light rainfall (Liu and Moncrieff 2007). Use of a microphysics scheme which explicitly predicted two moments of the graupel size distribution (mixing ratio and concentration) allowed the scheme to reduce the concentration of small hydrometeors during the simulation, thereby essentially increasing the mean size (van Weverberg 2012; Bryan and Morrison 2012). Similarly to the processes discussed previously, this resulted in less evaporation, a higher precipitation efficiency, and increased precipitation accumulation.

Chapter 6 will evaluate the effects of microphysical variations on bowing development and these other operational parameters just discussed, including precipitation accumulation and area, and system size.

CHAPTER 3
EXAMINATION OF ATMOSPHERIC WAVES ASSOCIATED WITH 13 MARCH 2003 BOW ECHO

The goal of this chapter is to determine if the surface pressure features noted in ASJ10 were indeed generated by gravity waves, and if so to ascertain the effect of those waves on the bow echo system particularly in relation to new bowing development. An idealized, high resolution Cloud Model 1 simulation (CM1, Bryan and Fritsch 2002) will be used to reproduce these pressure features and their cause. A discussion of the bow echo, which occurred on 13 March 2003, and all observed pressure features are given in Section 3.1. The CM1 model used is described in Section 3.2. Sections 3.3 and 3.4 analyze the low-frequency wave features simulated in the CM1 model, while Section 3.5 discusses the high-frequency wave features seen, and 3.6 provides a summary.

3.1 13 March 2003 case review

3.1.1 Fast-moving low pressure perturbations

Figure 3.1, from ASJ10, displays composite WSI NOWrad radar reflectivity data, overlaid with high-pass Lanczos-filtered pressure and temperature data from the Oklahoma Mesonet. (The high-pass filtering was designed to remove synoptic features from the data; see ASJ10 for more details.) The 13 March 2003 bow echo initialized as a convective line in central Oklahoma, in isolation from other convection at 0230 UTC (Fig. 3.1a). A low pressure region was evident centered over the convective line. This low pressure region quickly split and propagated away from the convective line (0345 UTC, Fig. 3.1b).

Data timeseries from Oklahoma Mesonet stations VANO and HUGO, the locations of which are shown by black dots in Fig. 3.1a, are given in Fig. 3.2. A dip in pressure, unaccompanied by a temperature change, is shown at arrow [a] at both stations. This would seem

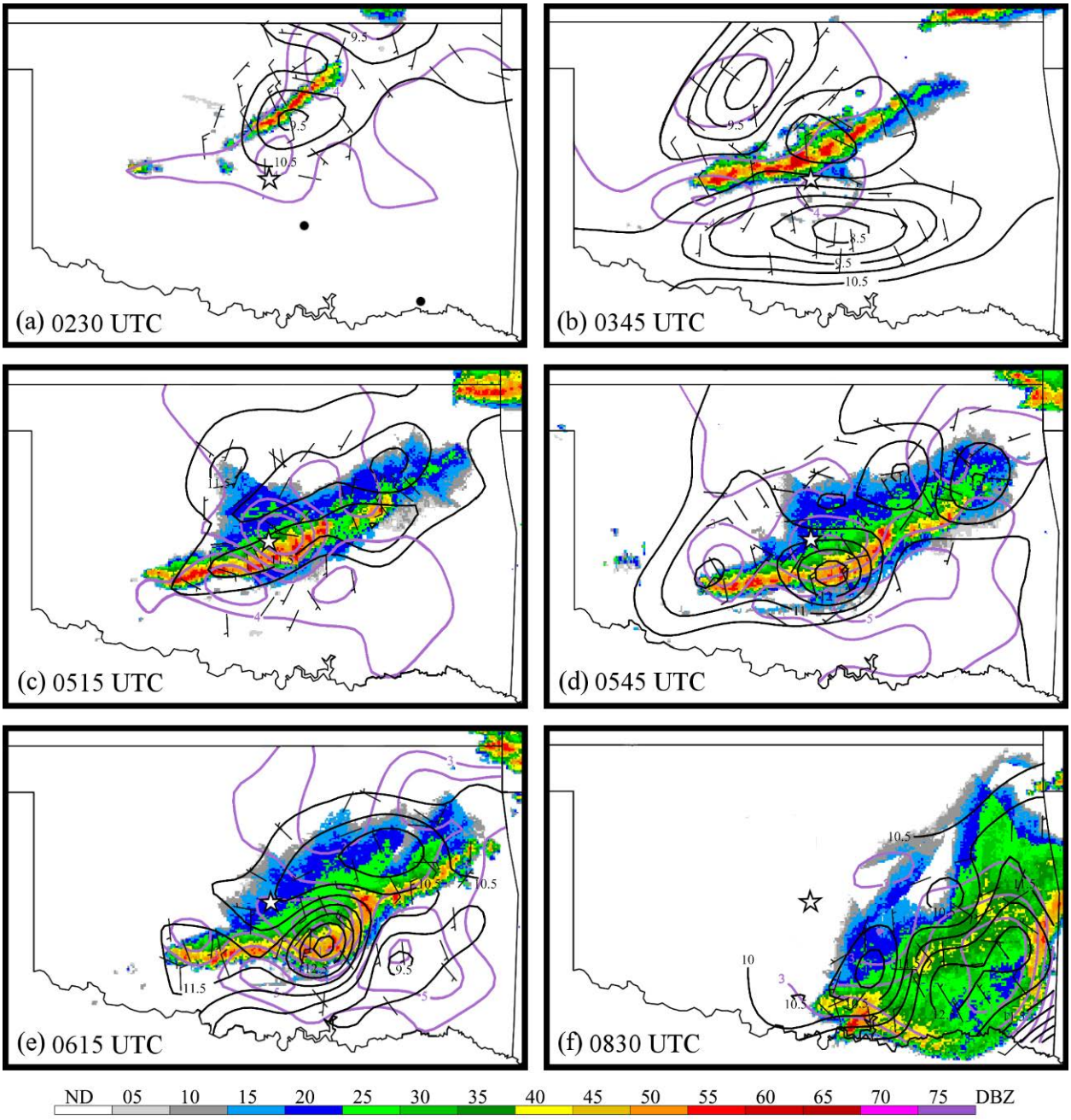

Figure 3.1: WSI NOWrad base reflectivity from 0230 (a), 0345 (b), 0515 (c), 0545 (d), 0615 (e), and 0830 (f) UTC 13 March 2003. High-pass filtered potential temperature (purple, 1^oC), surface wind (black, barbs) and adjusted pressure (black, 0.5 hPa). The star is the KTLX radar, and the black dots in (a) are Mesonet stations VANO and HUGO. (From ASJ10.)

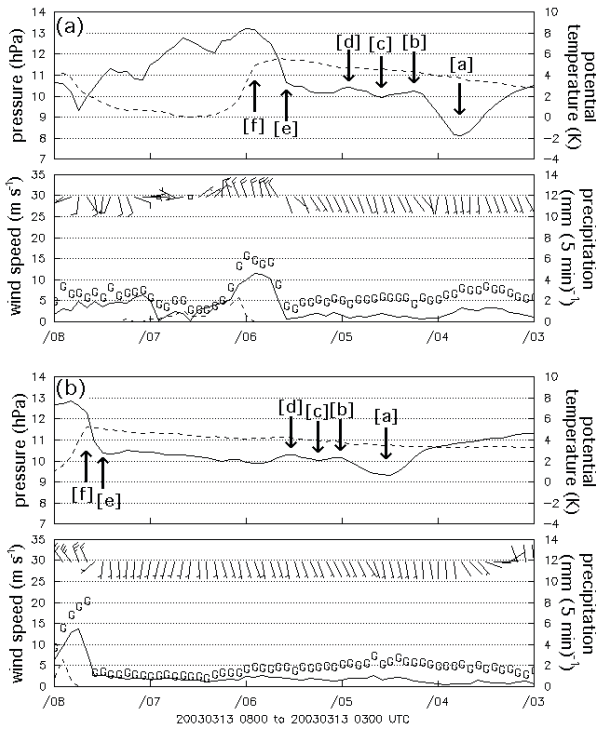

Figure 3.2: Timeseries display to high-pass filtered data from stations VANO (a) and HUGO (b) from the Oklahoma Mesonet (locations shown in Fig. 3.1a). Time increases to the left from 0300 to 0800 UTC 13 March 2003. Upper graphs in each figure show potential temperature (K, dashed, upper right scale) and adjusted pressure (hPa, solid line, upper left scale). Lower graphs show sustained winds (knots, barbs), sustained wind speed (m s^{-1}, solid line, lower left scale), unfiltered wind gusts (m s^{-1}, G, lower left scale), and unfiltered precipitation rate (mm (5 min)$^{-1}$, dashed line, lower right scale). [a] - [f] refer to indications of passing gravity waves or gravity current at each station and are referenced in the text.

to be indicative of a $n = 1$ gravity wave feature, as discussed in Chapter 2. In ASJ10, this dip in pressure was tracked in numerous Mesonet stations across Oklahoma, and an average ground-relative speed of 34.1 m s^{-1} was calculated. Isochrones of this feature are displayed in Fig. 3.3a. The mean environmental tropospheric wind speed parallel to the direction of motion of the feature, 1.6 m s^{-1}, was computed using the 0000 UTC sounding from Norman, Oklahoma (KOUN, Fig. 3.4). Accounting for this tailwind yielded an actual feature speed of 32.5 m s^{-1}.

Upon further examination of these timeseries, additional pressure features, also possibly indicative of gravity waves, were noted. Because these features are such small variations in pressure, they did not appear in the objective analysis. However, in Fig. 3.2, arrows [b], [c],

and [d] at each station are also pressure rises and dips unaccompanied by surface temperature changes. These features were evident at multiple Mesonet stations across Oklahoma as well, and isochrones of each feature are shown in Figs. 3.3b, c, and d. The ground-relative speeds of these features are estimated to be 32.8, 28.3, and 35.5 m s^{-1}, which are very similar to the ground-relative speed of the initial feature denoted by arrow [a], particularly considering the possible errors inherent in the estimation.

As discussed above, Nicholls et al. (1991) noted that upon a decrease in the magnitude of the heating, that is, a decrease in the amplitude of a $n = 1$ heating profile, a positive pressure perturbation propagates quickly away from the heating source in the lower half of the troposphere. Thus, it is possible that the low pressure perturbations indicated by arrows [a] and [c] were gravity waves generated by a sudden increase in the amplitude of a $n = 1$ heating profile, and the pressure increases at arrows [b] and [d] signatures of a sudden decrease in that profile. The large magnitude of the pressure response at [a] could have resulted from the larger, initial increase in convective heating as the updraft first developed. However, without observations of the heating profile within the convective system, such suppositions cannot be validated.

Bryan and Parker (2010) observed similar oscillations in surface pressure prior to the passage of a squall line. They related the initial oscillation in surface pressure to the combination of an approaching cold front and a hydrostatic response to surface cooling by anvil shading. In this case the synoptic features have been removed from the pressure data by the filtering technique, and the anvil had not yet reached the stations when the pressure rises at [b] and [d] occurred. Nevertheless, determination of the features as gravity waves requires a numerical model.

3.1.2 Pressure surge

The second pressure feature associated with the system noted by ASJ10 was a mesohigh surge partially ahead of the convective line. Between 0345 and 0515 UTC (Figs. 3.1b, c) a

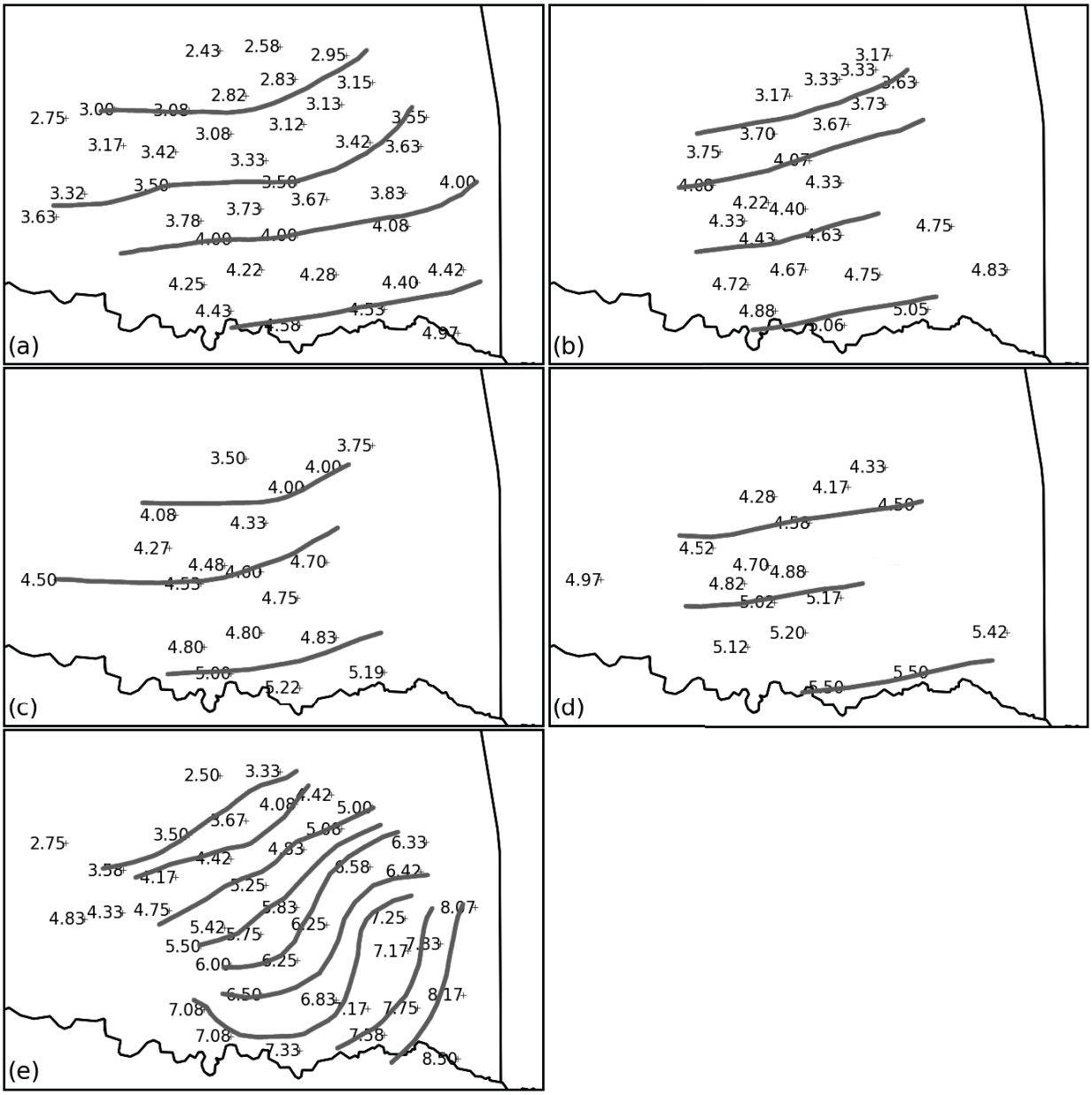

Figure 3.3: Isochrones (grey, contoured every 30 min) for the features noted in Fig. 3.2 at arrows [a], [b], [c], [d], and [e], corresponding to figure (a), (b), (c), (d), and (e), here, respectively. Only stations where each feature was observed are included (some stations are omitted for display clarity). Times are displayed in decimal format (e.g., 4.33 is 0420 UTC 13 March 2003).

mesohigh pressure perturbation formed over the convective line and spread southwestward as the convective intensity strengthened. At 0545 UTC (Fig. 3.1d) the mesohigh surged partially ahead of the convective line. This was shortly followed by new bowing development within the line at 0615 UTC (Fig. 3.1e).

It was noted in ASJ10 that the size of the mesohigh pressure surge in this figure produced by the objective analysis was excessive compared to timeseries observations. Given the pressure surge speed of 21.6 m s^{-1} during this time, the distance corresponding to the 20-min interval between the initial pressure rise and final pressure peak at station VANO (arrows [e] and [f] in Fig. 3.2a) should be 25.9 km. However, the pressure interval in Fig. 3.1d is approximately 60 km. Thus, while the mesohigh surge ahead of the convective line existed, its size was overestimated by about a factor of three. Multiple objective analysis methods were tried in an attempt to fix this overestimation, but it was an inherent problem in all analysis methods.

Figure 3.2a shows a sharp increase in pressure, a wind shift of almost 180 degrees, and an increase in wind speed all at 0535 UTC (arrow [e]), but no accompanying potential temperature drop. The sharp temperature drop and onset of rain at 0555 UTC (arrow [f]) indicated the arrival of the surface cold pool or gravity current. This pressure rise, significantly in advance of the temperature drop, occurred at almost all Mesonet stations passed by the bow echo system, including station HUGO (Fig. 3.2b, arrows [e] and [f].) The ground-relative speed of the feature was estimated to be 21.6 m s^{-1} (ASJ10). If the mean environmental wind speed of 1.6 m s^{-1} in the direction of surge motion is accounted for, the actual feature speed is 20.0 m s^{-1}.

These observations could be indicative of one of three features: a gravity wave response generated by low-level cooling behind the convective line, similar to simulations in Haertel et al. (2001); a non-hydrostatic pressure response to an intensifying cold pool as in Wakimoto (1982) or Klemp (1994); or a bore propagating ahead of the system in a stable boundary layer as in Parker (2008). Without observations above the surface it is not possible to discriminate

among these three possibilities. Thus, a numerical model was used to simulate and evaluate this feature.

3.2 Model description

Cloud Model 1 (CM1, Bryan and Fritsch 2002), version 1.15, was initialized with the 0000 UTC 13 March 2003 Norman, Oklahoma (KOUN) sounding, which is shown in Fig. 3.4. This sounding was released approximately two hours prior to convective initialization, and 100 km to the south. Minor smoothing was performed to remove absolute instabilities and prevent overturning immediately after initialization, and missing moisture data was extrapolated to upper levels, but otherwise the sounding was unmodified. The observed convection formed along a southwest-northeast line approximately 60° clockwise of vertical (Fig. 2a). The sounding was not rotated in the idealized simulation, and the idealized convection initiated along a south-north line. As a result, the 0-2.5 km line-normal wind shear values increased from 11.7 to 14 m s^{-1}, and 0-5 km shear from 6 to 14.2 m s^{-1}. In an idealized simulation with the sounding rotated, a bow echo did not form, suggesting shear over a deeper layer may be necessary as in Stensrud et al. (2005). A discussion of these implications, however, is beyond the scope of this study.

The domain covered 600 km (x direction) by 400 km (y direction) by 18 km vertically. A horizontal resolution of 250 m was used with a 2 s time step. The vertical resolution was 100 m from the surface to 4 km aloft; the resolution stretched to 500 m above 8 km. The Thompson et al. (2008) microphysics parameterization and TKE subgrid turbulence parameterization were used. The domain was translated 12.5 m s^{-1} in the x direction and 3.3 m s^{-1} in the y direction to keep the system inside.

The initialization method was the "cold pool-dam break" (Weisman et al. 1997). In this method, a "cold dam" of air was created along the left side of the domain by decreasing the initial potential temperature. This was done from 0 to 200 km in the x-direction, and 50 to 350 km in the y-direction. The magnitude of the potential temperature decrease was 6 K at

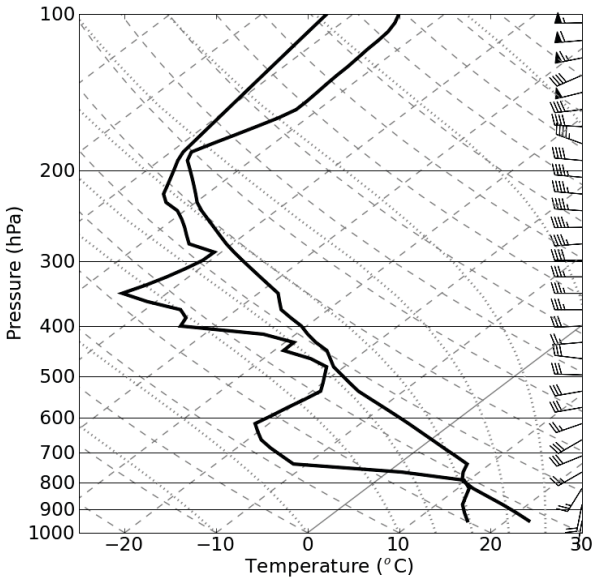

Figure 3.4: 0000 UTC 13 March 2003 KOUN sounding.

the surface, and linearly decreased until reaching 0 K 2.5 km aloft. As the simulation began, the cold pool dam "broke" and surged forward as a gravity current. Air in advance of the gravity current was forced upward, generating convection.

Coriolis forcing was not included in this simulation. Previous studies have noted that the temperature perturbations generated by gravity waves become trapped within a Rossby deformation radius, dependent upon the speed of the gravity wave (Johnson and Mapes 2001). The time and space scales within this study are small enough that this does not affect the results. However, these effects would begin to be noticed when tracking a fast-moving gravity wave over larger spatial scales; for a gravity wave moving at 30 m s^{-1}, at the latitude of Oklahoma, the Rossby radius of deformation (given as $\lambda_R = NH/f_c$, where f_c is the Coriolis force at 35 ° N latitude, and Z_t the height of the troposphere, 12 km) would be approximately 640 km.

3.3 Multiple $n = 1$ gravity waves

Within the CM1 simulation, convection initializes at 0:15 simulation time, directly over the edge of the gravity current created by the broken "cold pool dam". By 0:35 the convection

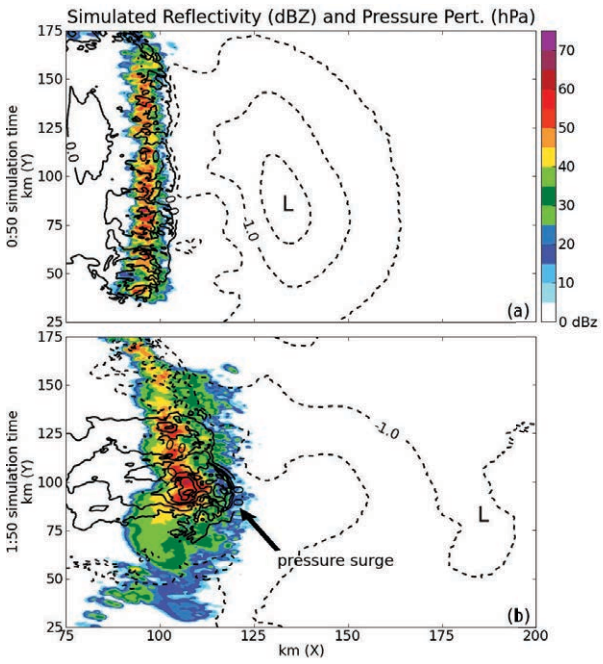

Figure 3.5: Simulated reflectivity (filled contours, dBZ) and pressure perturbation (black, 0.5 hPa, negative dashed) for (a) 0:50 and (b) 1:50 simulation time. Black arrow in (b) points to the pressure surge discussed in Section 3.4.

reaches approximately 12 km vertically, and remains there for the rest of the simulation. A low pressure perturbation of -1 hPa becomes evident parallel to and just ahead of the convective line (not shown). By 0:50, this feature has propagated approximately 30 km ahead of the convective line (Fig. 3.5a), and appears very similar to the observed fast-moving low pressure perturbation noted in Figs. 3.1a and b.

The vertical structure of this low pressure anomaly is displayed in Fig. 3.6. At simulation time 0:50, in Fig. 3.6a, it is located at approximately x=130 km, where a low pressure perturbation in the lower half of the atmosphere is overlaid by a high pressure perturbation aloft. (The convective line is at 105 km.) Subsidence is indicated in the "eastern" half of the low pressure anomaly, and ascending motion in the "western" half. A temporary dip in the potential temperature contours (not shown) is colocated with the pressure perturbations, due to the adiabatic warming and cooling associated with the downdraft-updraft couplet. The environmental flow toward the system is strengthened from the surface to 6 km aloft, and the flow away from the system is also intensified, at 6 km and above (not shown). In

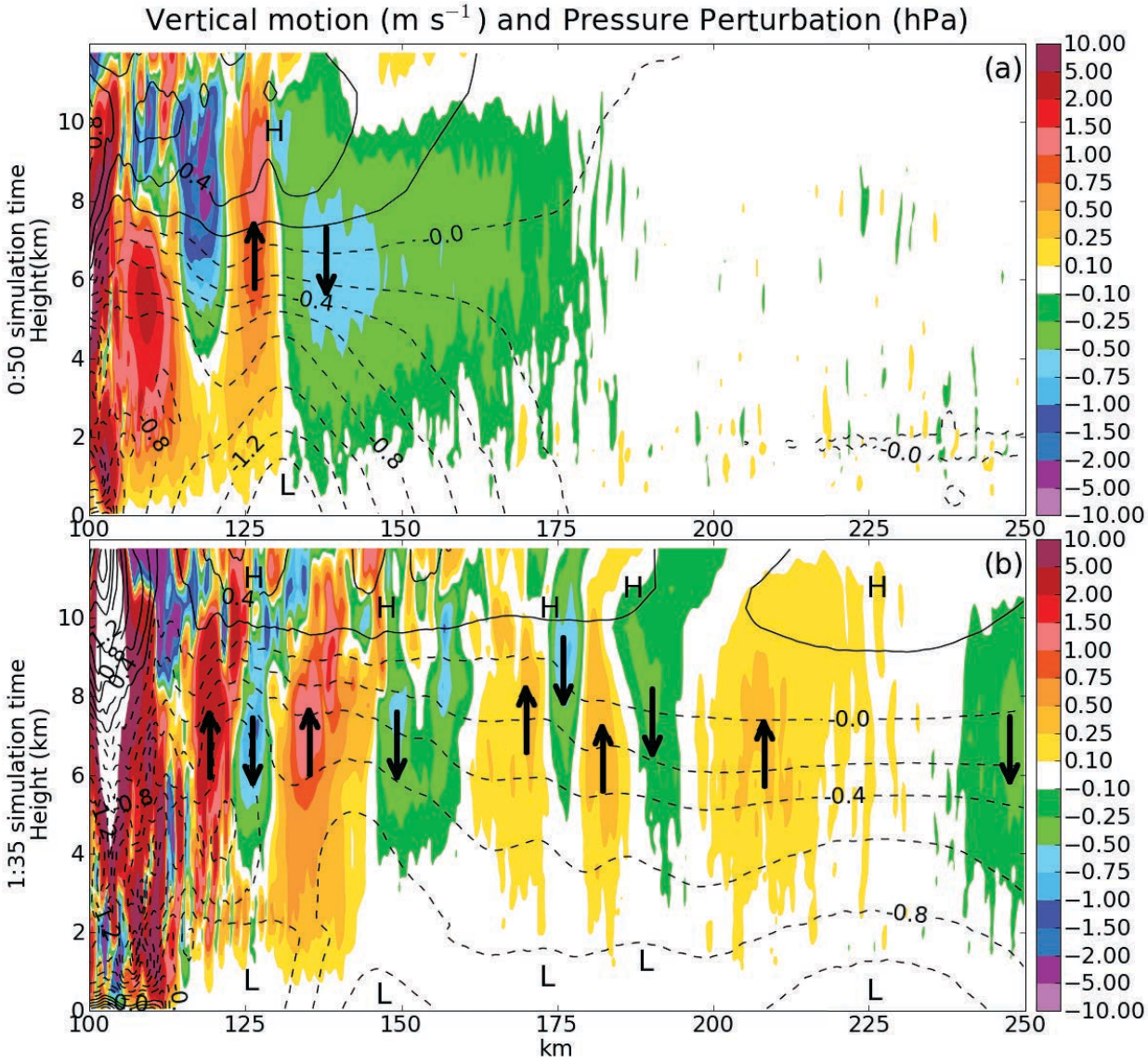

Figure 3.6: Vertical x cross-section from 0-12 km, through the pressure surge, averaged 5 km about the x cross-section. Vertical wind speed (color, m s^{-1}) and pressure perturbation (black, 0.2 hPa, negative dashed). (a) 0:50 and (b) 1:35 simulation time. Upward and downward motion indicated by arrows; high and low pressure perturbations by "H" and "L". The wave in (a), and the rightmost wave in (b), are the same feature.

sum, this feature appears very similar to a gravity wave generated by a sudden increase, shortly followed by a decrease, of a $n = 1$ heating profile (Nicholls et al. 1991).

By 1:35 simulation time, the low pressure anomaly is at approximately x=225 km (Fig. 3.6b). The "widening" of the wave is due to the wave being advected slightly northward; the x cross-section of the figure views the wave at an angle. Taking into account the mean tropospheric wind speed in direction of wave motion (-13.0 m s^{-1}) and the translation speed of the domain (12.5 m s^{-1}), the modeled wave speed is an estimated 32 m s^{-1}. This is very close to the estimated first observed feature speed of 32.5 m s^{-1} (Fig. 3.3a). Using the N of the pre-storm environment in the simulation, 7.8×10^{-3} s^{-1}, and 12 km as the depth of the troposphere, (2.1) predicts the speed of a $n = 1$ wave in this environment to be 29.8 m s^{-1}. This is somewhat slower than both the modeled and observed speeds, but still very similar.

Also evident in Fig. 3.6b are four other features, at x=120 km, 145 km, 175 km, and 182 km, that appear very much like $n = 1$ gravity waves. To determine if these features are also waves generated by surges in the $n = 1$ heating profile, a Hovmöller diagram of vertical motion at 6 km was created (Fig. 3.7b). Six kilometers was selected as it is half the height of the troposphere and vertical motion associated with a $n = 1$ wave should be strongest there (Nicholls et al. 1991); this is observed in Fig. 3.6. The mean microphysical heating between 5.2 and 7.3 km, the closest three vertical levels above and below 6 km, was also calculated (Fig. 3.7a). This was calculated along a 10 km y cross-section through the $n = 1$ wave pressure responses (y=100 to 110 km, shown in Fig. 3.6). It should be noted that the heating rates shown are averages over an area, and it is possible cells within that area have larger heating fluctuations.

From Fig. 3.7, it can be seen that changes in the mean mid-level heating rate correspond well with wave signatures in the vertical motion field. For example, an increase in heating between approximately 0:22 and 0:28 produces an area of subsidence that propagates away from the source. The decrease in heating between 0:29 and 0:33 generates an area of ascent that does the same. This process is repeated numerous times throughout the simulation;

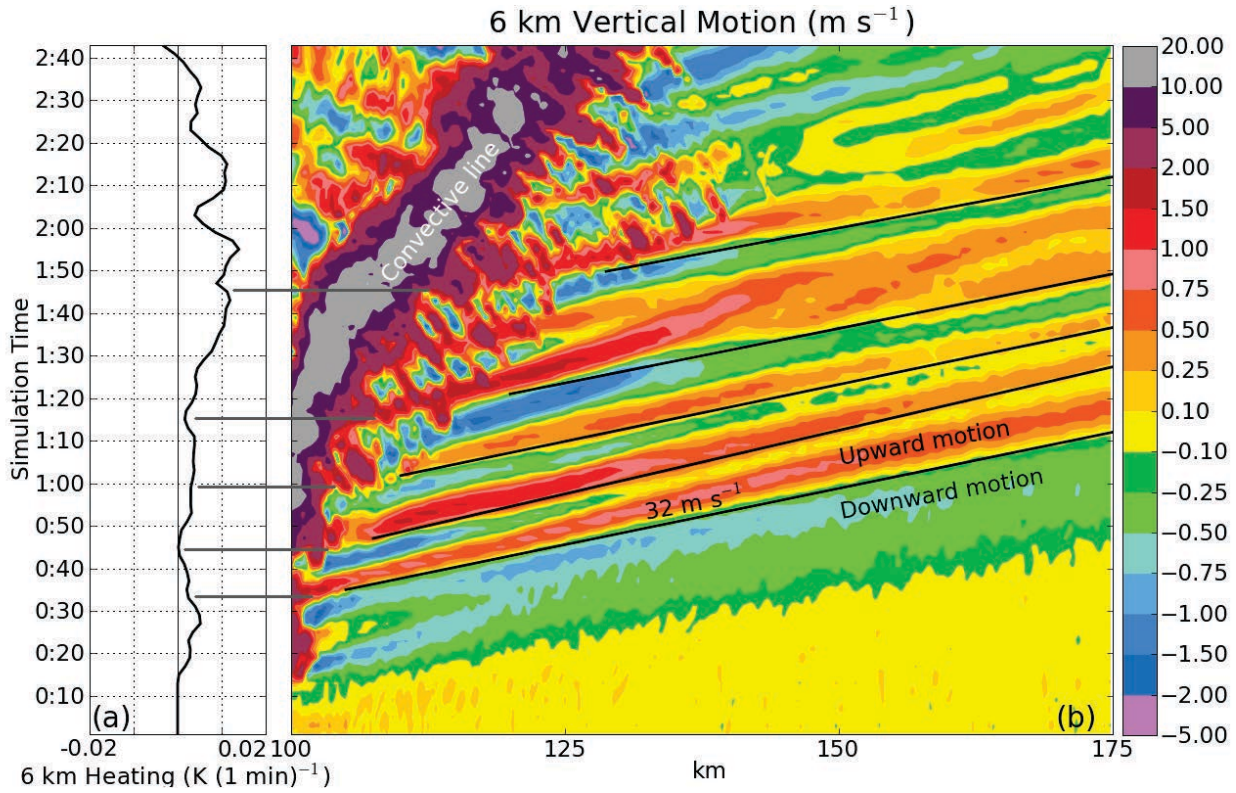

Figure 3.7: (a) Mean microphysical heating (K (1 min)$^{-1}$) between 5.2 and 7.3 km aloft and x=50 to 150 km (width of system), from 0:00 to 3:00 simulation time. Y-average calculated 5 km about the x cross-section. (b) Time evolution of horizontal distribution of vertical motion (m s^{-1}) at 6 km aloft, averaged 5 km about the x cross-section. Signature of the five gravity waves shown in Fig. 3.6, are denoted by black lines. Grey lines connect the time of initial generation of these waves to the heating rate.

as an illustration the five waves shown in Fig. 3.6b are marked on Fig. 3.7b by thin black lines. The times of generation of each of these waves, as determined by first visibility of the wave signature within the vertical motion field, are connected to the heating rate at the same time by thin grey lines; each upward motion response occurs in conjunction with an increase in the 6 km heating rate. The waves generating the vertical motion perturbations all propagate at approximately the same speed, 32 m s^{-1}. This speed is very similar to the speed of all four pressure features tracked across Oklahoma in Figs. 4a-d. Therefore, it is a reasonable assumption that these observed features were reflections at the surface of $n = 1$ gravity waves generated by variations in the convective heating profile.

Lane and Reeder (2001) found that the subsidence generated by a $n = 1$ wave due to an

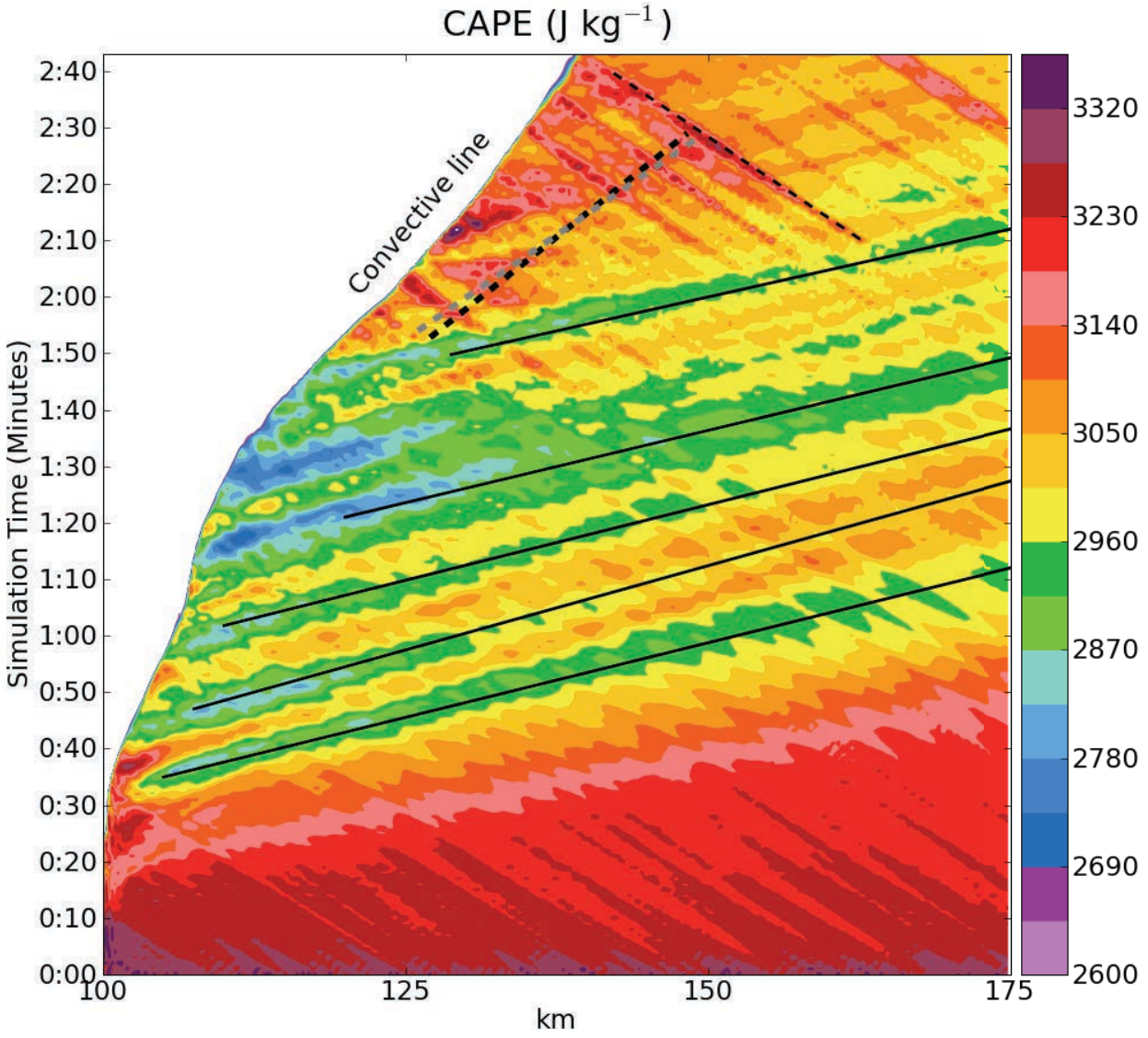

Figure 3.8: Time evolution of horizontal distribution of CAPE (color, 45 J kg^{-1}), averaged 5 km about the x cross-section. Five thin black lines track the five gravity waves shown in Fig. 3.6. Thick dashed grey and black lines denote the pressure surge discussed in Section 3.4. Thin dashed black line tracks a cloud generated by a high-frequency gravity wave, discussed in Section 3.5.

increase in heating decreased the pre-storm convectively available potential energy (CAPE) in their study by approximately 240 J kg^{-1}, or 15% of the ambient environmental value. Conversely, the wave produced due to a decrease in the first internal mode of heating should lift, cool, and moisten the troposphere, increasing the CAPE. Fig. 3.8d displays the CAPE over the same horizontal cross-section as Fig. 3.7, with respect to time. As expected, the variations in CAPE very closely match the gravity waves shown in Fig. 3.7b.

With each gravity wave passage, the CAPE values vary approximately 200 - 250 J kg^{-1}, or about 5-7% with respect to the initial sounding CAPE of 3752 J kg^{-1}. This is somewhat less than the Lane and Reeder (2001) results, but their simulations used a more stable atmosphere, with an N^2 of 0.0115 s^{-1}, as opposed to this study's 0.0078 s^{-1}; higher potential temperature perturbations are expected with increased stability. The convective inhibition (CIN) values (not shown) do not vary significantly with passage of each $n = 1$ wave. Because the largest magnitudes of vertical motion associated with each $n = 1$ wave were located at approximately 6 km, and most of the CIN was located in the 0-3 km layer, the lack of effect on CIN is not surprising. Most of the CAPE variations were due to changes in the mid-level lapse rate around these peak vertical motions.

3.4 Pressure surge

3.4.1 Feature description

A surge of higher pressure ahead of the convective line can be seen in Fig. 3.5b, in the same location where the convective line was beginning to bow. As discussed above, the observed pressure gradient surge extended approximately 20 km ahead of the convective line. The surge in Fig. 3.5b extends approximately 5 km ahead of the convective line, and will later extend as far as 12 km ahead of the convective line; but both of these are a smaller distance than observed. The bowing portion of the simulated convective line was much smaller than observed as well - approximately 25 km in length instead of 100 km, meaning associated cooling would be of smaller size as well. However, the simulated heating

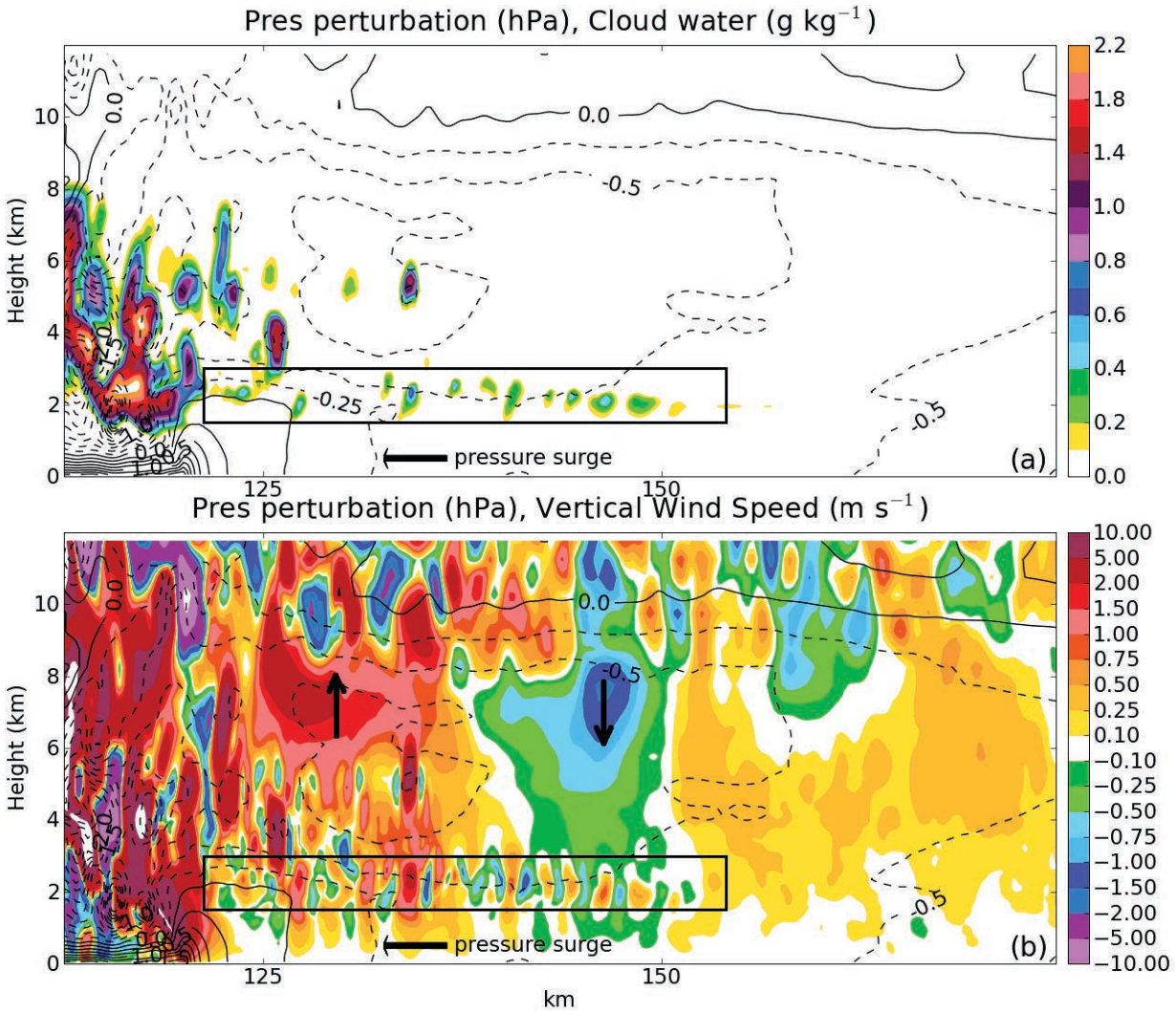

Figure 3.9: Vertical 0-12 km x cross-section through pressure surge, averaged 5 km about the x axis at time of surge development, 1:55 simulation time. (a) Cloud water mixing ratio (color, 0.1 g kg^{-1}) and pressure perturbation (black, 0.25 hPa, negative dashed). (b) Vertical wind speed (color, m s^{-1}) and surface pressure perturbation (as in (a)). Convective line is at approximately x=120 km. The pressure surge is labelled. The vertical black arrows mark upward and downward motion. The black boxes outline the high-frequency wave signatures discussed in Section 3.5.

profile and associated $n = 1$ waves match very well with the observed pressure perturbations, as discussed in the previous section. Thus, it is not unreasonable to expect the processes generating the simulated surge to be similar to those generating the observed surge.

Figure 3.9 displays a vertical cross-section through the surge immediately after its development. A positive pressure perturbation (with respect to the initial state) ahead of the

convective line (between x = 120 and 125 km), reaching vertically to 2 km, is evident. The general trend of pressure increasing toward the convective line continues from x = 132 km, however. The pre-storm pressure field has been significantly modified by the numerous $n = 1$ wave features already propagating ahead of the convective line. Overall, the net effect of these earlier waves was a decrease in surface pressure ahead of the system. Thus, within Fig. 3.9 the general trend of increasing pressure is more relevant than absolute positive or negative perturbations, and the pressure surge will be identified here as the increasing pressure gradient between x = 120 to 132 km, from 0 to 2.5 km aloft.

A number of higher-frequency features are also noticeable in the cloud water and vertical motion fields in Fig. 3.9, between x = 125 and 150 km and at approximately 2 km and 5 km aloft. These features will be discussed in the next section. Unfortunately, because these high-frequency features were in the same area as the pressure surge, the surge's exact structure and evolution was difficult to clearly isolate.

To better examine the pressure surge another Hovmöller diagram, of surface pressure along the same cross-section through the surge, was constructed (Fig. 3.10b). Examination of Fig. 2.1c shows that the height of the negative pressure perturbation (in that figure, 5 km) corresponds to the height of the maximum heating within the profile. Because the pressure surge appears approximately 2.5 km in depth, the sum of the microphysical heating near that level (2 km) was examined and is displayed in Fig. 3.10a.

Evident within this figure are a number of compression waves, propagating at approximately 360 m s^{-1}, causing periodic oscillations within the surface pressure and heating fields. As these oscillations are strongest at the surface and do not appear above 4 km, propagate horizontally only, and do not have any associated vertical velocity perturbations, the waves appear to be Lamb waves (Nicholls and Pielke 2000; Fanelli and Bannon 2005). CM1 is a compressible model (Bryan and Fritsch 2002) so this type of behavior is expected and was formally evaluated by Smith and Bannon (2008).

The five waves noted in Fig. 3.6b also appear in Fig. 3.10b as low pressure regions

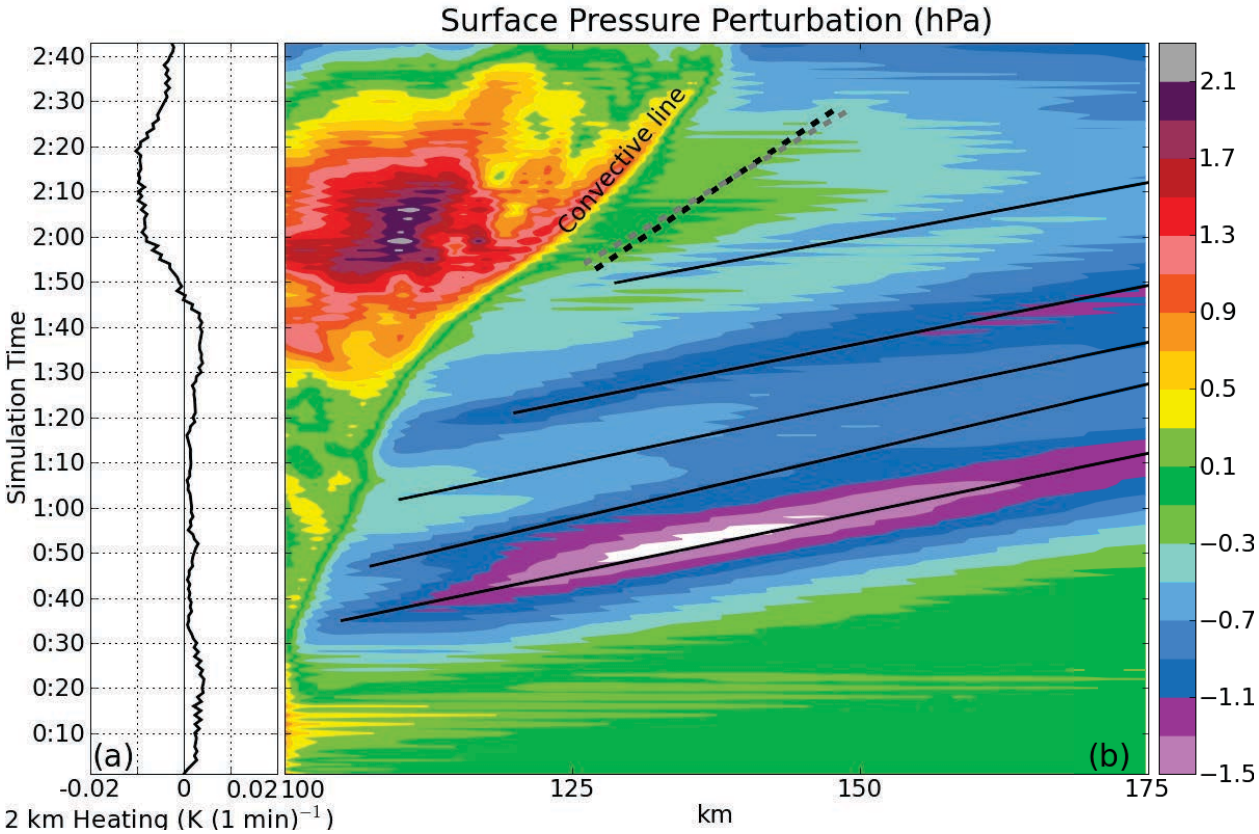

Figure 3.10: (a) Mean microphysical heating (K (1 min)$^{-1}$) between 1.8 and 2.2 km aloft, y=100.5 to 105.5 km (5 km about pressure surge), and the width of convective line. (b) Time evolution of surface pressure perturbation (hPa) averaged 5 km about the x cross-section. Thin black lines are as in Fig. 3.7b. The thick dashed black and grey lines show the progression of the pressure surge feature.

propagating away from the convective line (marked by thin black lines). Not every $n = 1$ wave that is visible in Fig. 3.7b is also evident at the surface. Tulich et al. (2007) found that due to variations in tropospheric wind shear and stability, not all vertical levels of a gravity wave travel at the same speed. The first $n = 1$ wave has the strongest surface pressure response. The subsidence associated with that wave lasts for the longest time period (Fig. 3.7b), resulting in the low surface pressures.

Immediately prior to the appearance of the pressure surge, at approximately 1:45 simulation time, a strong increase in 2 km cooling is evident in Fig. 3.10a. The cause and vertical structure of the cooling will be discussed later, but its timing in relation to the pressure surge is unmistakable. The surge cannot be a bore because there is not a sufficient density

discontinuity between the surface layer and the layer above (Fig. 3.4). The pressure surge is also moving faster than the convective line and associated gravity current, which has a speed of 7.6 m s^{-1} during the same period and is labeled in Fig. 3.10b. The pressure surge and gravity current are clearly unique features in Fig. 3.10b and are separated by approximately 10 km at 2:25 simulation time. Thus, the evidence suggests that the pressure surge feature is a gravity wave generated by increased cooling in the lower levels of the convective line.

From Fig. 3.9, the leading edge of the pressure surge can be delineated by the -0.25 hPa contour. However, because of the oscillations in the low-level pressure field due to Lamb waves, tracking the surge using this contour does not produce a constant speed. Evaluation of Fig. 3.10b shows fluctuations in surface pressure with a period of approximately 1 min. Thus, to minimize the error introduced by these fluctuations, two speeds of the surge-leading -0.25 hPa contour were calculated: one from 1:53 to 2:29 simulation time, and the other from 1:54 to 2:28, using two-minute intervals within these periods.

The two calculated speeds are displayed on Fig. 3.10b as grey and black dashed lines, and they are very similar: 11.3 and 9.8 m s^{-1}, respectively. After calculating the mean and removing the domain translation and mean wind in direction of surge motion, this yields a feature speed of 11.0 m s^{-1}. Using (2.1) and the N calculated immediately in front of the system at that time (7.7×10^{-3} s^{-1}), the predicted speed for a $n = 3$ wave is 9.8 m s^{-1}. The two speeds agree reasonably well, particularly considering the possible error added to the speed estimation by the Lamb and high-frequency waves. The low-level positive pressure perturbation associated with a $n = 3$ wave, given a 12 km tropopause height, should extend to approximately 3 km, as is also seen here (Fig. 3.9).

Haertel and Johnson (2000), hereafter HJ00, observed similar gravity wave behavior in response to a moving source of cooling. In their Section 3b, a two-dimensional cool source extending to 4 km was prescribed to move at 10 m s^{-1} in a linear numerical model. The cooling produced a gravity wave response moving at 13 m s^{-1}, or 3 m s^{-1} ahead of the cool source. The response contained a positive pressure perturbation extending to approximately

3 km aloft, overtopped by a weak low pressure perturbation (see their Fig. 5b). Because the cool source and wave speed were similar, the positive surface pressure perturbation was amplified by over 20% compared to a similar simulation with a stationary cooling source. As the speed of the pressure surge gravity wave and convective line are also similar in this simulation, it is possible the pressure surge response is being enhanced by this effect.

In Lane and Reeder (2001), the heating profile generating the $n = 3$ wave extended to the tropopause, and contained three antinodes consisting of low- and upper-level cooling and mid-level warming. The resulting pressure perturbations combined to extend the depth of the troposphere as well. Within HJ00, the wave response was produced solely by low-level cooling, and the pressure response also remained in the lower levels. The pressure responses in both studies appeared very similar within the lower levels, at least at time scales on the order of 2 h or less; at longer time scales, the vertical propagation of the wave in HJ00 became evident. The full vertical structure of a $n = 3$ wave does not appear in the perturbation pressure field of this simulation (Fig. 3.9). It is possible that the response is masked by the high-frequency features, but it is also possible that the pressure surge gravity wave response is produced solely by the low-level cooling.

The pressure surge observed in ASJ10 moved at a speed of 21.6 m s^{-1}, which is significantly faster than observed here. This would explain why the observed pressure surge was larger than the simulated one. However, a few factors must be considered. The stability and mean wind of the environment through which the observed pressure surge was propagating is not known. The observed surge could also have been generated by deeper low-level cooling. Nevertheless, this simulation still provides an feasible mechanism that can generate the pressure surge ahead of the bowing convective line seen so often by ASJ10.

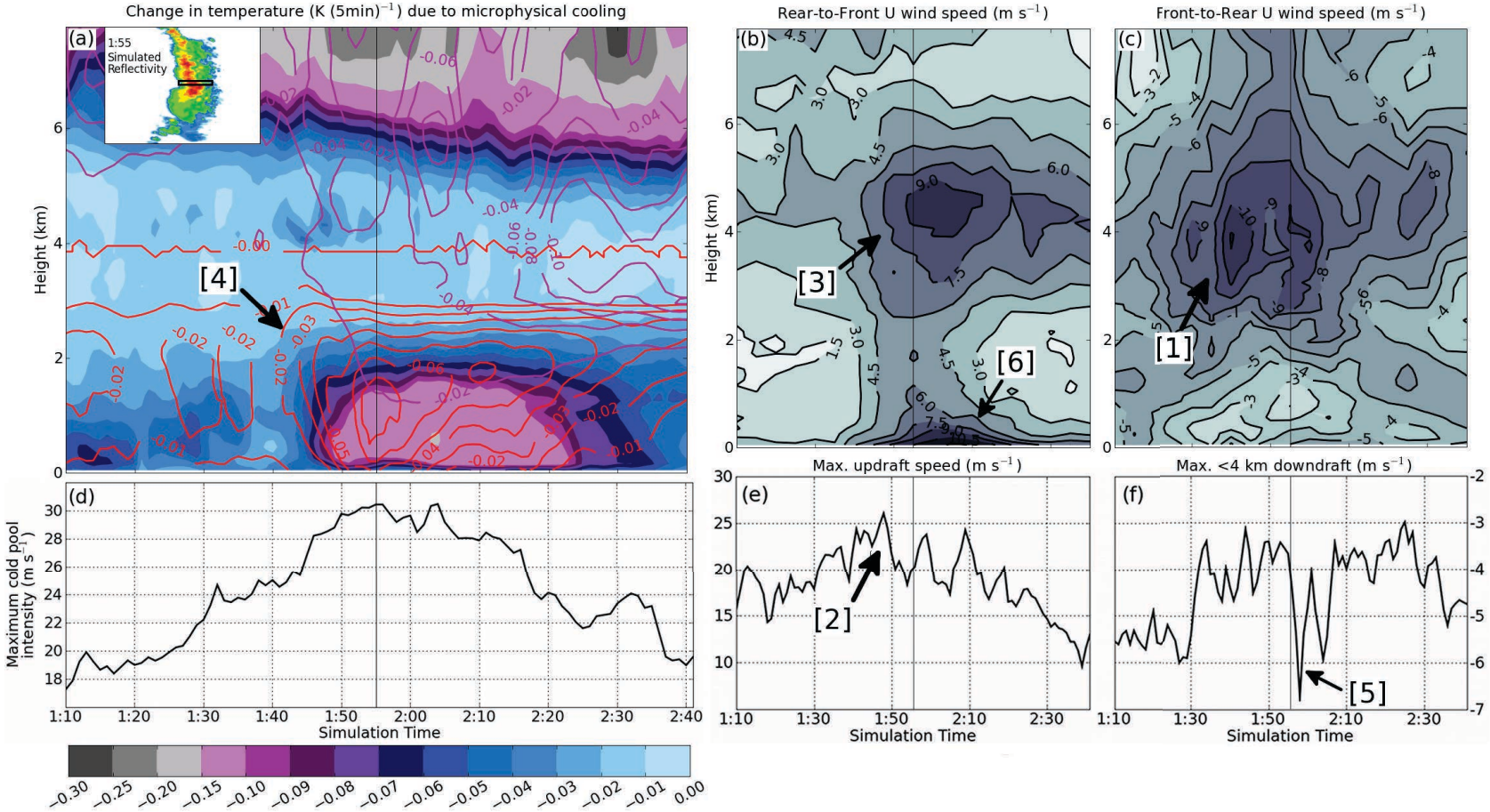

Figure 3.11: Time-height series of mean vertical profiles, created by averaging over the horizontal width of the system and pressure surge in the x-direction, and 5 km about the pressure surge and bow echo in the y-direction. Area averaged over shown in inset in (a); area moves with convective line. The positive and negative u wind averages were calculated separately. The thin black vertical line in each is the time of the start of the pressure surge. (a) Microphysical cooling rates due to evaporation (filled contours, K (5 min)$^{-1}$), melting (red, 0.01 K (5 min)$^{-1}$), and sublimation (purple, 0.02 K (5 min)$^{-1}$). (b) Storm-relative front-to-rear u wind (1.5 m s^{-1}). (c) Storm-relative rear-to-front u wind (1 m s^{-1}). (d) Maximum cold pool intensity (C, m s^{-1}). (e) Maximum upward vertical motion (1 m s^{-1}). (f) Maximum downward vertical motion (1.0 m s^{-1}). Labels [1] through [6] detail the bowing process and are discussed in the text.

3.4.2 Low-level cooling source and effects

The cause of the sudden increase in the low-level cooling can be seen in the time-height cross-sections shown in Fig. 3.11. These are mean vertical profiles created at each output time by averaging over the horizontal width of the convective system and pressure surge in the x-direction, and 5 km about the pressure surge in the y-direction. (Averaging area shown in inset in Fig. 3.11a; this area travels with the convective line). The positive and negative u wind averages are calculated separately. Model gridpoints are separated into two groups, one containing points with rear-to-front flow; the other front-to-rear flow. The mean horizontal motion of each group is calculated and displayed separately, in Figs. 3.11b and c. This procedure allows examination of mean fields without the opposing fields canceling each other out. The magnitude of the intensity of the cold pool (C) is shown in Fig. 3.11d, and it is calculated using $C^2 = \int_0^h B\, dz$, where B is buoyancy, and h the height at which B becomes 0. B is given by

$$B = g\left(\frac{\theta - \overline{\theta}}{\overline{\theta}} + 0.61(q_v - \overline{q_v} - q_t)\right) \tag{3.1}$$

where g is gravitational acceleration, θ potential temperature, q_v water vapor mixing ratio, q_t total hydrometeor mixing ratio, and the bars designate environmental conditions. The maximum updraft speed and maximum low-level (below 4 km) downdraft speed are shown in Figs. 3.11e and f.

Initially, the storm-relative front-to-rear flow increases at 1:30 simulation time, at approximately 3.5 km aloft ([1] in Fig. 3.11c). Shortly thereafter, the convective updraft suddenly strengthens as well ([2] in Fig. 3.11e). The mid-level rear-to-front flow also shows a strong increase at this time, and it deepens up to 6 km and extends to the surface ([3] in Fig. 3.11b). Following this, at 1:45, a large increase in all three of the microphysical cooling fields ([4] in Fig. 3.11a) occurs immediately prior to the appearance of the pressure surge.

The sudden influx of dry air into the rear of the storm as surmised by Figs. 3.11b and 3.4,

as well as the descent of the rear-to-front flow to the surface (Fig. 3.11b), led to these large increases in evaporation and melting. The vertical extent of the total cooling by evaporation, melting, and sublimation at this time is approximately 4 km (Fig. 3.11a). Cold pool intensity significantly increases at this same time (Fig. 3.11d). Finally, at the time the surge can be seen ahead of the convective line, 1:55, the convective downdraft suddenly strengthens even further ([5] in Fig. 3.11f) and strong outflow appears at the surface ([6] in Fig. 3.11b).

It is unclear at this time what causes the first increase in mid-level front-to-rear flow at 1:30. However, after this point the sequence of events follows what would be expected in new bowing development (Weisman 1992; Weisman 1993; Weisman and Rotunno 2005; James et al. 2006). The convective updraft strengthens, increasing heating aloft and strengthening the mid-level pressure perturbation. This forces an increase in the rear-to-front flow, bringing drier air into the system and aiding in evaporative and sublimation cooling. The increase in microphysical cooling helps intensify the low-level downdrafts. All of these in combination act to locally speed one portion of the convective line, creating a bow; the surface winds increase as well. A gravity wave, shown at the surface by a surge in increasing pressure, is produced by the strong increase in low-level cooling and travels ahead of the bowing segment of the convective line.

Time-height cross-sections through a non-bowing section of the convective line at Y = 125 km, generated in the same manner as Fig. 3.11, are shown in Fig. 3.12. At 1:30, the storm-relative front-to-rear inflow is approximately 2 m s^{-1} slower (Fig. 3.12c) than in the bowing segment. Convective updraft speeds at this time are weaker (Fig. 3.12e), and reduced updraft magnitudes are found in the lower levels (not shown). Significantly, after 1:40 the mean rear-to-front flow at 4 km is almost half the magnitude of the rear-to-front flow in the bowing segment (Fig. 3.12b), resulting in a reduced influx of dry air into the rear of the storm system.

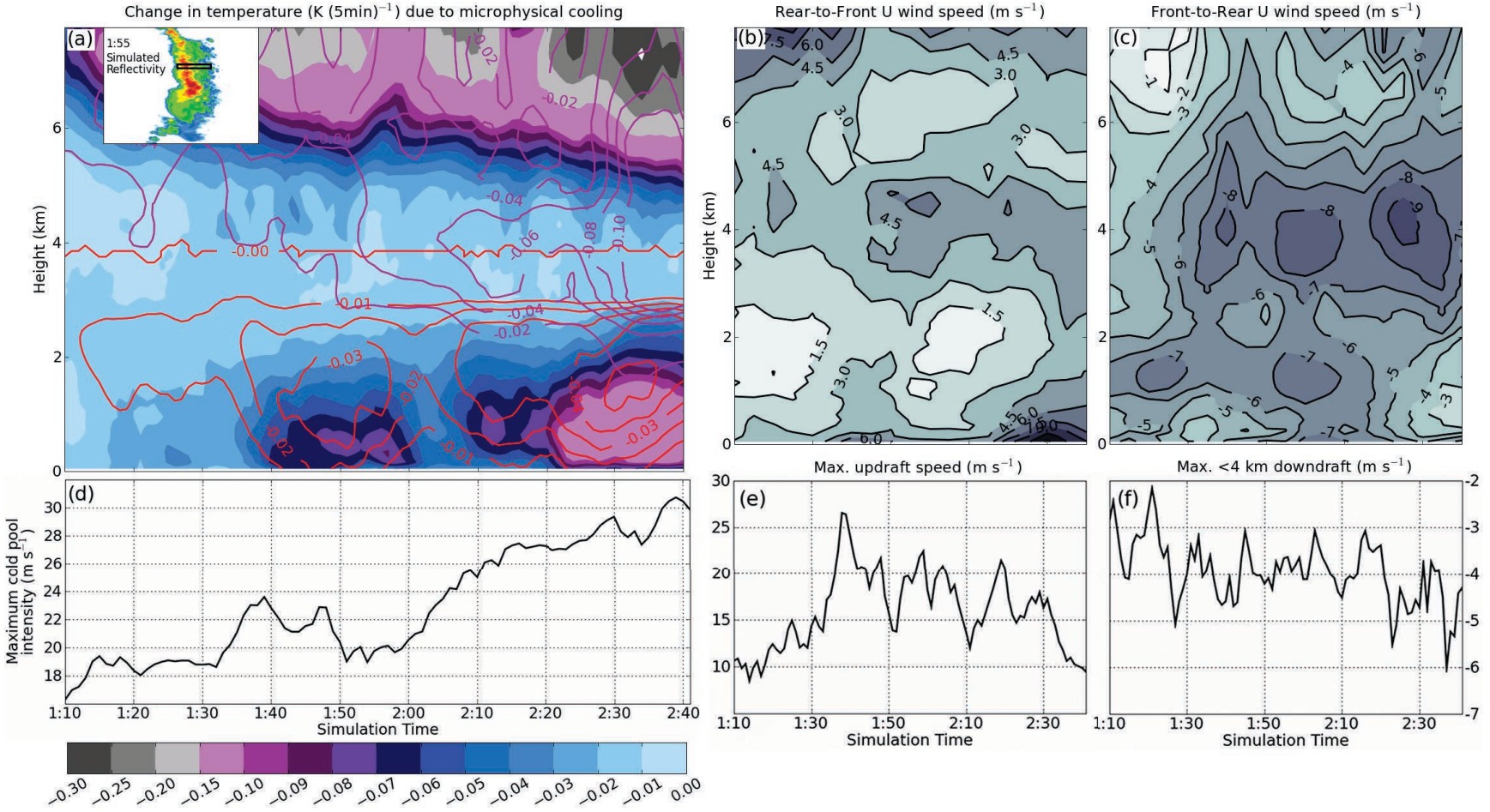

Figure 3.12: As in Fig. 3.11, but for a non-bowing segment of the convective line, shown in inset in (a).

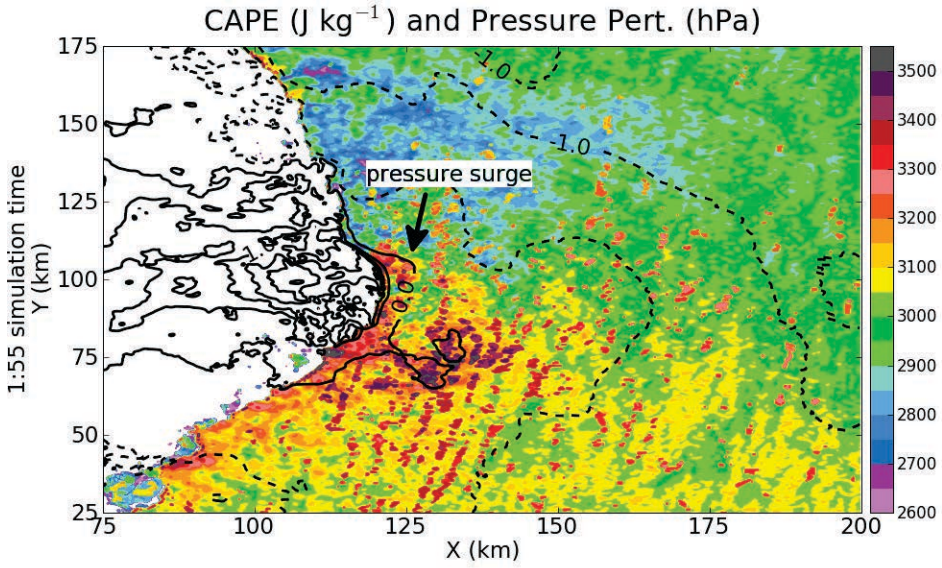

Figure 3.13: CAPE (color, J kg^{-1}) and pressure perturbation (black, 0.5 hPa, negative dashed) at 1:55 simulation time.

As a result, the amount of microphysical cooling by melting and evaporation (Fig. 3.12a) is only half the amount seen in the bowing segment (Fig. 3.11a). The cold pool itself is also not as strong (Fig. 3.12d), resulting in a slower speed for this portion of the convective line compared to the bowing portion. Without a strong increase in cooling, the resulting gravity wave and surface pressure response is much weaker, and the pressure surge is not seen ahead of this portion of the convective line (Fig. 3.5b). Low-level downdrafts are also not as strong (Fig. 3.12f).

As the cooling (including sublimation) within the bowing segment generating the pressure surge gravity wave extends to 4 km, the lifting associated with it should also. Unfortunately, the signal of this vertical motion is masked by the high-frequency features (Fig. 3.9). However, upward motion would act to cool and moisten that layer (Fovell 2002, Fovell et al. 2006), and hence destabilize the atmosphere. Similar pre-storm low-level cooling and moistening was observed by Bryan and Parker (2010), which they considered possibly to be the effect of a $n = 2$ gravity wave. In Figs. 3.13 and 3.8 an approximate 250 J kg^{-1} increase in CAPE is evident over the same area as the surge, from 3050 to 3300 J kg^{-1}. There is not an increase in

CAPE of similar magnitude along other, non-bowing portions of the convective line without a pressure surge (Fig. 3.13).

Surprisingly, CIN was minimally affected by the pressure surge gravity wave (not shown). The main signal shown in the CIN field was a result of the high-frequency features, discussed is Section 6.

3.5 High-frequency gravity waves

In Fig. 3.9b, a series of updraft-downdraft couplets are located between approximately 2 and 2.5 km aloft, and x=125 and 150 km. Couplets of this nature are noted at this height as early as 30 minutes into the simulation. Within the updraft portion of these couplets condensation regularly occurs and clouds form (Fig. 3.9a). These features appear remarkably similar to those observed in Fovell et al. (2006) in association with high-frequency gravity waves generated by multicellularity in the convective line.

Unlike the low-frequency gravity waves discussed above, these higher-frequency waves require a trapping level other than the tropopause so their energy does not propagate vertically immediately. In Fovell et al. (2006), the trapping level was provided by the curvature of the wind profile due to outflow aloft at anvil level. However, the vertical motions associated with the high-frequency gravity waves in that study extended to 7 km. Here, the couplets are trapped in a layer around 2 km.

An examination of the environmental stability explains this (Fig. 3.14). A thin stable layer is evident between approximately 2 and 2.5 km. Both above and below this layer are regions where the Scorer parameter is negative, which act to reflect the wave energy. Thus, the updraft couplets and associated clouds remain in the 2 to 2.5 km layer. A similar trapping level is also evident just below 6 km (Fig. 3.14), with updraft-downdraft couplets and cloud development immediately below (Fig. 3.9). A simulation was run with the trapping levels around 2 km removed, and no high-frequency wave features were found in that region. High-frequency waves were still found just below 6 km, as that trapping level was unmodified.

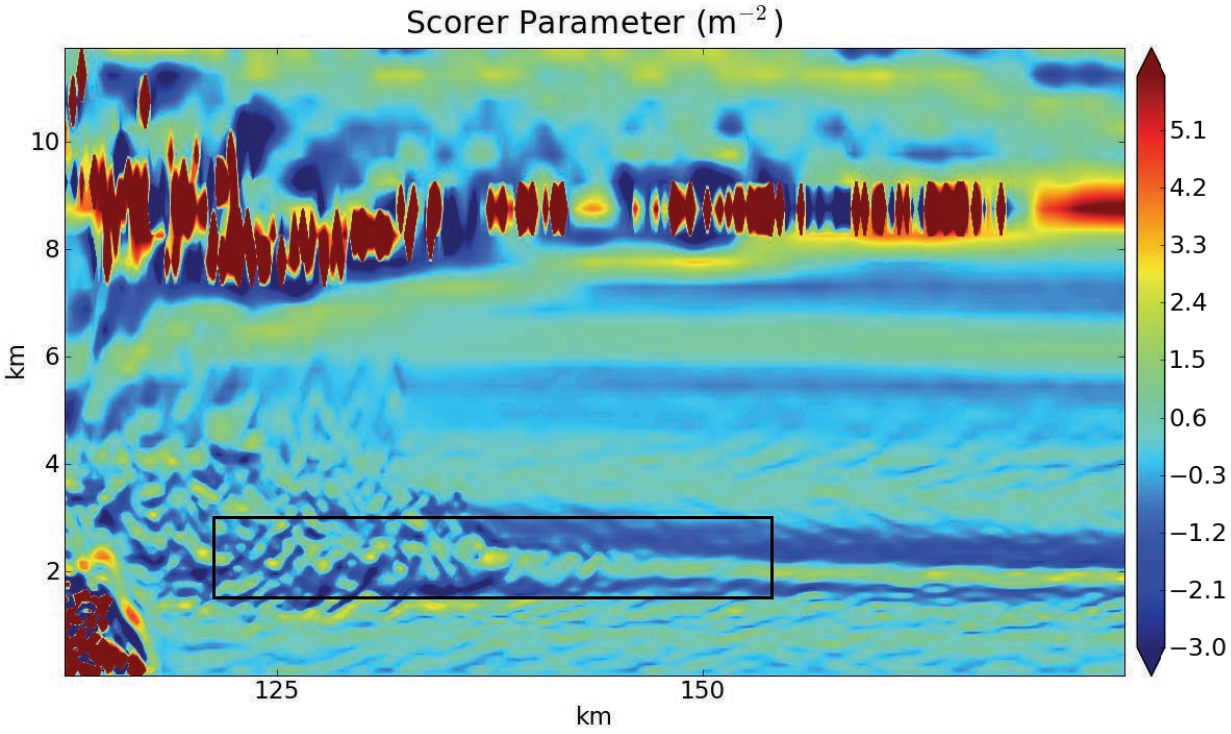

Figure 3.14: Vertical 0-12 km cross-section at 1:50 simulation time, averaged 5 km about x-axis, of the Scorer parameter (color, m^{-2}). Black box delineates the same area as in Fig. 3.9.

It was also noted by Fovell et al. (2006) that these high-frequency gravity waves can have an effect on the pre-storm environment, particularly when condensation occurs within an associated updraft and forms a cloud. The latent heat released would act to modify the parcel's stability; if ingested into the storm the extra warmth and moisture would intensify the system. However, if the cloud became large enough to produce rain, it could create its own cold pool, which would instead have a negative effect when ingested. In this case, none of the clouds produced rain or had individual cold pools, so the feedback to the system should be positive. The effect of the latent heat release on the stability of the 2 to 2.5 km layer can be seen within Fig. 3.14 between x=125 and 130 km: the latent heat release from the formation of multiple clouds, and the turbulent mixing associated with this, mixed out the stable layer and decreased the overall stability.

Increases in CAPE due to these small clouds can be seen in Fig. 3.13. The magnitude of these increases are largest within the pressure surge: small cells containing CAPE values

larger than 3500 J kg^{-1} can be seen immediately ahead of the convective line within the pressure surge in Fig. 3.13. This effect can also be seen in Fig. 3.8. One specific cloud (and associated increase in CAPE) is tracked in Fig. 3.8 by a thin dashed black line. The formation of the cloud was associated with increased CAPE (approximately 200 J kg^{-1}) and decreased CIN (approximately 2 J kg^{-1}, not shown). However, within the CAPE field (Fig. 3.8) the variations associated with these high-frequency features appear largest in magnitude, by approximately 50 J kg^{-1}, after passage of the pressure surge gravity wave.

As in Fovell et al. (2006), the low-frequency wave "prepares" the environment for later high-frequency features by gently lifting and cooling the lower levels of the troposphere. This allows the later high-frequency features to generate much stronger variations in CAPE by forming clouds in this newly-moistened layer. Once a cloud is formed due to lifting from the high-frequency wave, it does not travel with the wave, but instead is advected by the mean flow at that level. Within Fig. 3.8, the thin dashed line is used to track the speed of one of the clouds at -11.4 m s^{-1}. Accounting for the 12.5 m s^{-1} domain translation, the cloud moves at the speed of the mean wind at that level. It is advected toward the system as in Fovell et al. (2006).

3.6 Summary

In this chapter, the surface pressure features observed in conjunction with the 13 March 2003 bow echo by Adams-Selin and Johnson (2010) were further evaluated. In that original study, a fast-moving low pressure feature and slower-moving high pressure surge were both observed. In this chapter, three additional fast-moving pressure features were noted that followed shortly after the originally observed low pressure feature.

The 13 March 2003 bow echo was simulated in an idealized CM1 simulation. Numerous $n = 1$ waves were generated, resulting from both increases and decreases in the first internal mode of heating. The speeds of these waves very closely matched the speeds of the observed fast-moving pressure features, suggesting those were also $n = 1$ waves. In the simulation,

each $n = 1$ wave modified the environmental CAPE by 5-7%. In sum, significantly more wave activity occurred in the environment ahead this convective systems than would previously have been supposed.

The simulation also reproduced the pressure surge, albeit a slightly slower and smaller version. The pressure surge was due to a gravity wave generated by a large increase in low-level (0-4 km) microphysical cooling just prior to its development. The lifting associated with the wave cooled and moistened the low levels in advance of the convective system. Numerous high-frequency waves, created by small-scale heating changes, were ducted between two unstable layers at approximately 2.5 km aloft. These waves warmed and moistened the low levels by condensing water vapor in their updrafts which released latent heat. The combination of these factors increased the CAPE by 8% of the initial sounding.

Due to the proliferation of the high-frequency features and the many gravity waves generated by temporal changes in the convective heating profile, the exact structure of the pressure surge and other waves in the system was difficult to determine. Thus, the next chapter will use a constant heating profile to examine the resulting gravity waves. Also, as Adams-Selin and Johnson (2010) observed the pressure surge in conjunction with 35 of 39 examined bow echoes, this suggests a strong connection between the low-level cooling generating the pressure surge and new bowing development. Chapter 5 will examine this and other microphysical effects on bowing in more detail.

CHAPTER 4
EVALUATION OF MICROPHYSICAL PROFILES ACTING TO GENERATE GRAVITY WAVES

In the previous chapter, so many low- and high-frequency gravity waves were generated within the convective simulation that determining the structure of one, individual wave was difficult. Thus, the goal of this chapter is to examine the gravity waves being produced by a constant heating profile, similar to Pandya and Durran (1996), taken from two moments in time within the previous chapter's simulation. The structure and environmental effects of these waves will be discussed, and the heating profile itself examined via statistical methods.

4.1 Methodology

4.1.1 Simulation descriptions

The simulation discussed in the previous chapter will be referred to hereafter as the "full physics" simulation. Within that simulation, the heating due to microphysical changes was tracked at each model output time. Two two-dimensional microphysical heating profiles of interest from that simulation have been selected to examine further. The first, or "early" profile, occurred at 0:40 in the full physics simulation, just as a $n = 1$ wave was being generated. This profile is displayed in Fig. 4.1a as a vertical x cross-section through the convective line. (The cross-section is located through where the pressure surge will later develop.) Within this profile is some cooling in the lower levels, but it primarily consists of heating throughout the convective line. It is fairly representative of the heating profile within the system in the early stages of its lifecycle.

The second, or "surge" profile (Fig. 4.1b) occurred at 1:50 in the full physics simulation, immediately prior to the development of the pressure surge. It contains the increased low-

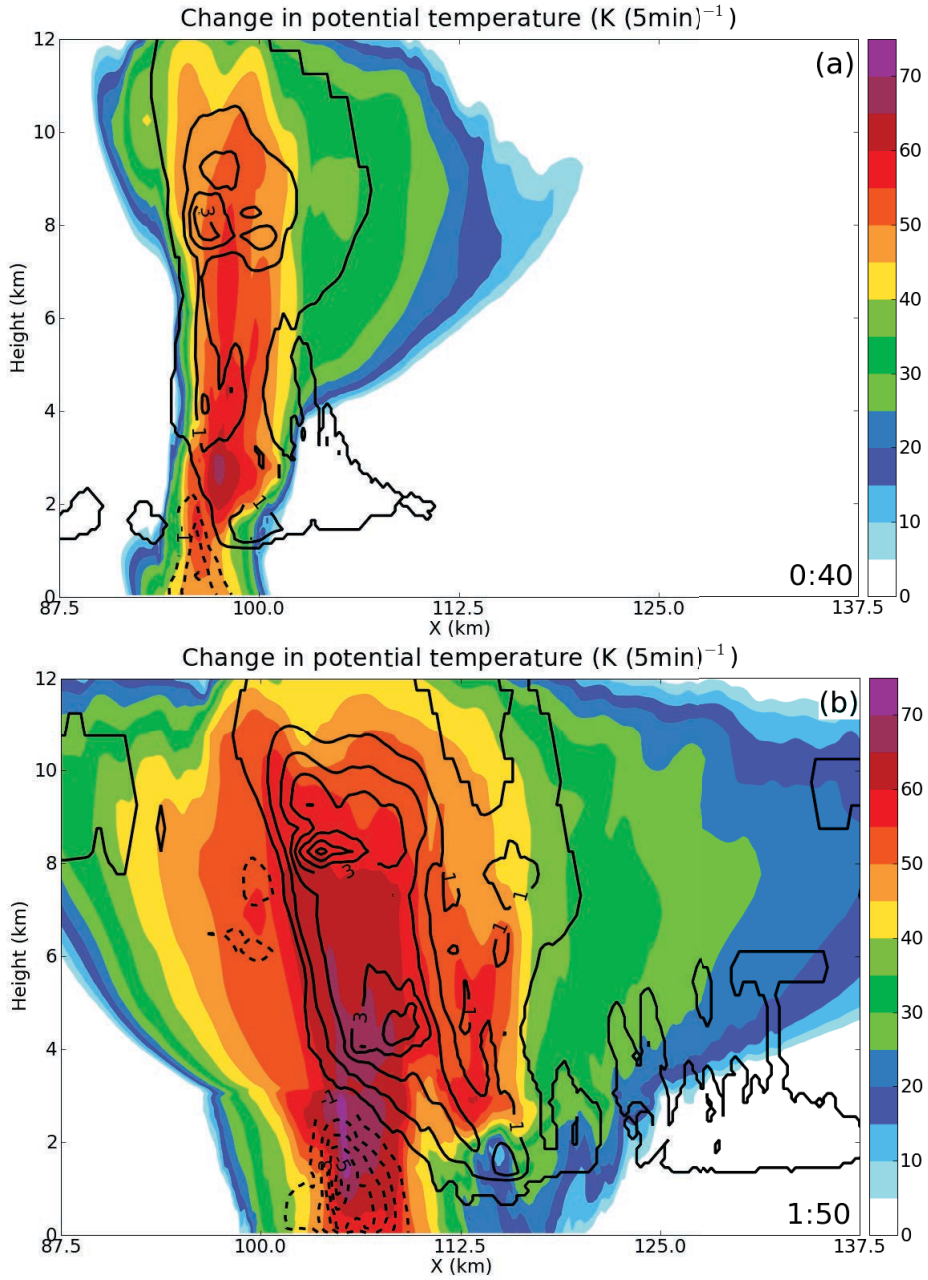

Figure 4.1: Vertical cross-sections of microphysical heating rate over the past 5 minutes (black, 1 K (5 min)$^{-1}$, negative dashed) and simulated radar reflectivity (dBZ). (a) from the full physics simulation at 0:40 simulation time; (b) from 1:50 simulation time. Both are averaged 10 km in the y-direction, about a cross-section through the area of the pressure surge discussed in the previous chapter.

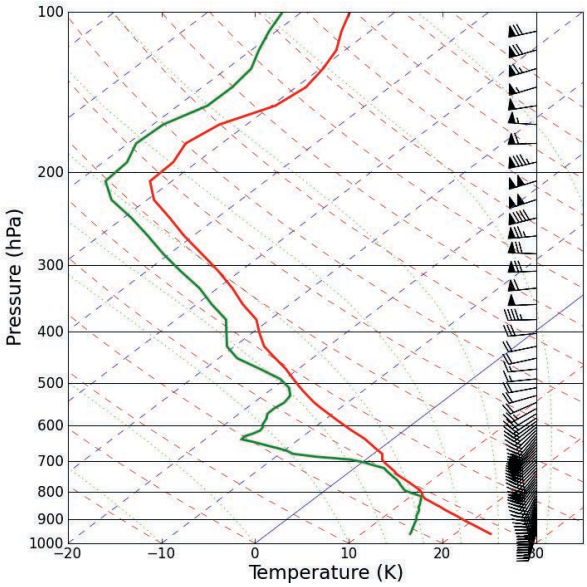

Figure 4.2: Mean sounding profile from full physics simulation, over a 1 km box 5 km in advance of the pressure surge as it developed.

level cooling noted at that time (see Fig. 3.11a in the previous chapter), as well as a more horizontally tilted heating structure.

To better observe the gravity waves generated from these two-dimensional heating profiles, each was placed into a dry simulation of version 1.15 of the CM1 model (Bryan and Fritsch 2002), with all microphysical processes turned off. These two runs are called the "early" and the "surge" dry simulations, respectively. The initial sounding used for the early simulation was the KOUN sounding used for the full physics simulation (Fig. 3.4). At the time the early heating profile occurred in the full physics simulation (0:40), few modifications to the pre-convective environment had taken place (not shown). Using a non-idealized sounding allowed evaluation of the effects changes in stability and the wind profile with height had on the evolution of generated gravity waves; an idealized sounding would have constant stability and wind shear values.

By the time of the surge heating profile, the pre-storm environment had been significantly modified (Fig. 4.2, compare to Fig. 3.4). The initial sounding used in the surge dry simulation was a mean sounding calculated over a 1 km box, 5 km ahead of the pressure surge as it

developed in the full physics simulation (1:50, Fig. 4.2). A significant amount of lifting, cooling, and moistening over the 800 to 700 hPa layer was evident when compared to the original sounding (Fig. 3.4). This lifting was discussed in the previous chapter as a combined effect of low- and high-frequency gravity waves.

The same domain size, horizontal and vertical resolution, and parameterizations (excepting microphysics) of the full physics simulation were used in the dry simulations as well. Each two-dimensional x-z cross-section of heating, as shown in Fig. 4.1, was placed into a dry simulation domain without changing its location in either the x or z direction. That profile was then extended uniformly in the y-direction, until 50 km from the north and south edges of the domain. The heating rates were reduced in amplitude with a cosine half-wavelength, reaching 0 K s^{-1} 30 km from the north and south domain edges. This heating distribution was constant in time, turned on at model initialization, and remained on throughout each simulation.

4.1.2 Statistical evaluation of heating profile

Many previous idealistic evaluations of the generation of gravity waves utilized a one-dimensional tropospheric vertical profile of heating that was a harmonic of the depth of the troposphere (Schmidt and Cotton 1990; Nicholls et al. 1991; Mapes 1993). The distribution of this heating, specifically, the number of its antinodes, determined the type and speed of gravity wave generated through (2.1). If multiple heating modes were superimposed on each other, multiple gravity waves were generated (Nicholls et al. 1991). In order to predict what gravity waves might be generated by the two-dimensional heating profiles in this study, the one-dimensional mean vertical profile of each was calculated. This profile can then be compared to combinations of the harmonic heating functions. If the waves predicted by this method do not match those generated, it suggests that the heating profile of the system cannot be entirely represented by a one-dimensional profile. This will allow evaluation of

Table 4.1: Vertical modes in the "early" mean vertical heating profile determined to be significant at level of 99%. "Sign" of vertical mode explained in the text.

Vertical mode	Sign
$n = 1$	+
$n = 2$	-
$n = 3$	+
$n = 4$	-
$n = 5$	-
$n = 8$	-
$n = 10$	-

the importance of the horizontal distribution of the heating, similar to the work of Pandya and Durran (1996).

Ten vertical harmonics of the troposphere were calculated using:

$$x_n = sin\left(\frac{n\pi z}{H}\right) \tag{4.1}$$

where n is the vertical mode 1 through 10, z is height, and H is the height of the tropopause (12 km). A multiple linear regression technique was used, with the multiple x_n as independent predictor variables, and the one-dimensional vertical heating profile as the dependent predictand. An ordinary least squares method was selected, with the constant coefficient assumed to be zero. A two-tailed Student's t-test was utilized to determine how significantly different each x_n was from 0.

4.2 "Early" dry simulation

4.2.1 Wave identification and structure

Using the statistical method just described, the one-dimensional vertical heating profile used in the early dry simulation was evaluated. The vertical modes that were at least 99% significant are shown in Table 4.1. The term "sign of the mode" indicates if the first antinode, that is, the antinode closest to the surface, was negative or positive. If the antinode was

positive, heating was occurring in those levels; if negative, cooling. For example, the heating profile typically observed in the stratiform precipitation region with cooling in the lower levels and warming aloft (Houze 1982; Johnson and Young 1983) would be considered a $n = 2$ mode wave of negative sign.

The linear regression method used predicted seven different gravity waves to be generated from this heating profile. The cooling at lower levels (Fig. 4.1a) should create a gravity current as well. It is possible that the gravity current could overtake some of the higher mode waves and so not every one of them would be visible. Also, the significance of the $n = 8$ and 10 modes is likely only due to the large increase in deposition heating at 8 km (Fig. 4.1a).

Figure 4.3 displays the early dry simulation at 1:40 simulation time. Four unique features are evident, marked by thick black lines. These four features will be referred to as feature [1]-[4], from right to left across the figure. In Fig. 4.3a feature [1], at approximately x=285 km, consists of a low pressure perturbation at low levels, and increased pressure aloft. Warming is evident throughout the column (Fig. 4.3b), with downward motion at the leading edge of the warming, and upward motion following (Fig. 4.3c). This is very similar to the atmospheric response in a $n = 1$ gravity wave of positive sign (see Fig. 2.1a-d for comparison).

Feature [2] exhibits increased pressure at low levels and aloft, with decreased pressure at mid-levels (Fig. 4.3a). The temperature response contains cooling at low levels, and warming aloft (Fig. 4.3b). The vertical motion field is less clear, but appears to consist of leading upward motion and trailing downward motion in the lower two-thirds of the atmosphere, and the reverse above (Fig. 4.3c). This response matches well with a $n = 2$ gravity wave of negative sign (Fig. 2.1e-h), although the vertical distribution of the pressure and temperature perturbations is not uniform like in Nicholls et al. (1991). This is due to the variations in stability within the environment, not present in the Nicholls et al. (1991) simulations.

Feature [3] is associated with a low pressure perturbation from 0-2 and 6-9 km aloft, and high pressure from 2-6 and 9-11 km (Fig. 4.3a). The potential temperature response

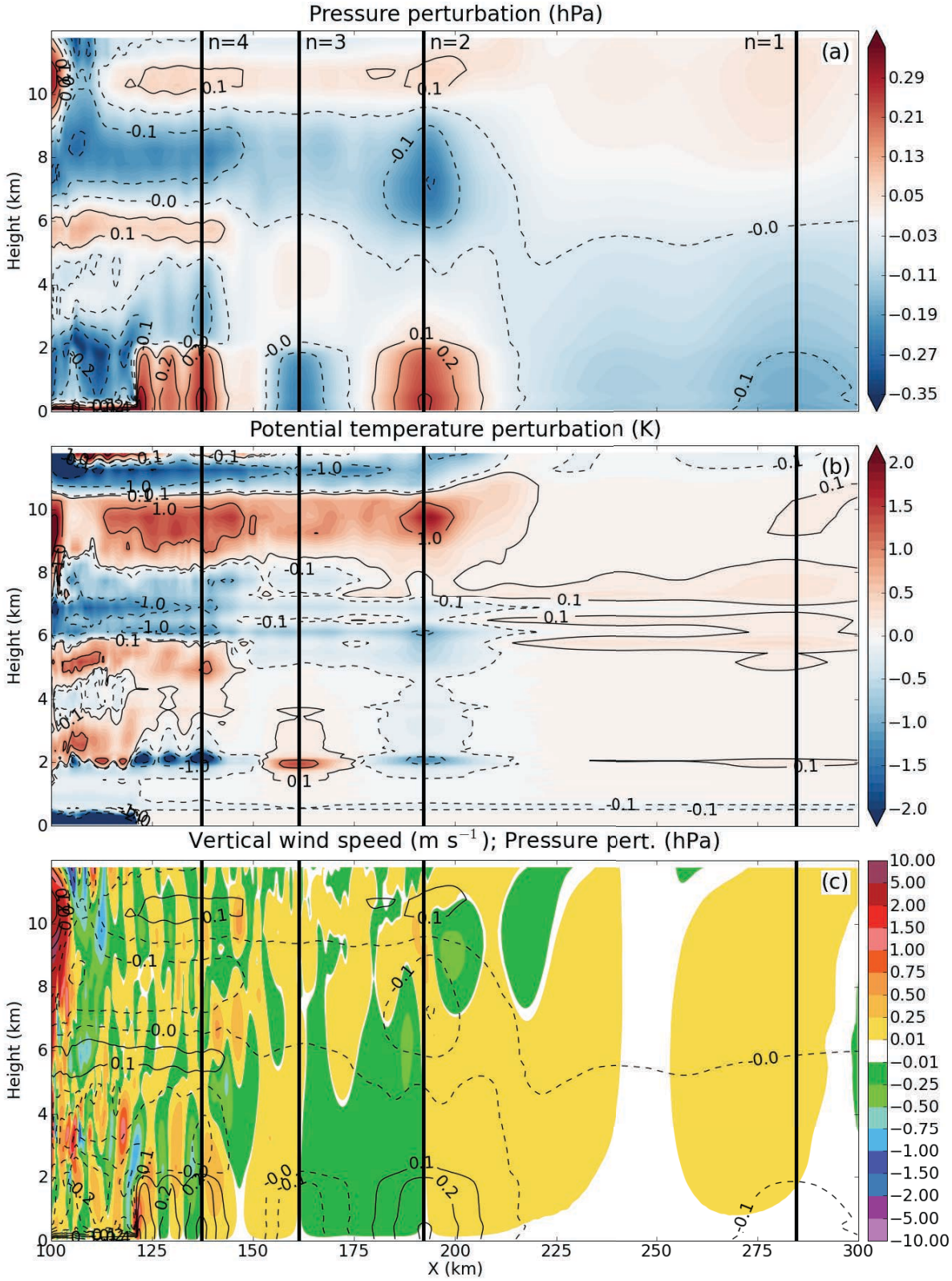

Figure 4.3: *Caption on following page.*

Figure 4.3: *From previous page*: vertical cross-sections of (a) pressure perturbation (0.1 hPa black contours overlaid), (b) potential temperature perturbation (K, black contours at -2, -1, -0.1, 0.1, and 1 K overlaid), and (c) vertical wind speed (m s^{-1}, color) and pressure perturbation (0.1 hPa, black, negative dashed) from 1:40 into the early dry simulation. Thick black lines mark the $n = 4$, 3, 2, and 1 gravity waves, at 157, 161, 192, and 285 km, respectively.

has three nodes: warming in the lower third of the troposphere, cooling at mid-levels, and warming aloft (Fig. 4.3b). There is also additional cooling from 11-12 km whose cause is not clear at this time. The vertical motion field is even more noisy than with feature [2], but it is clear from 0-4 km aloft the feature is led with descending motion, and followed by ascending motion (Fig. 4.3c). This description fits well with a $n = 3$ wave of positive sign.

Finally, feature [4] appears very similar to a $n = 4$ mode wave of negative sign. Increased pressure is evident from the surface to 2 km aloft, between 5 and 6 km, and 10-11 km (Fig. 4.3a). Decreased pressure can be seen from 2-5 and 6-10 km. Cooling is observed from 0-3 km and 6-8 km, and warming from 3-6 and 8-11 km (Fig. 4.3b). The vertical motion field in the vicinity of this feature is even more chaotic, but upward motion extends from 0-4 km in advance of the feature, and downward motion behind it (Fig. 4.3c).

Table 4.2: Simulated and predicated speeds of four wave modes in the first dry run simulation. Predicted speed calculated using the mean N of the profile, 7.8×10^{-3} s^{-1}. The mean wind speed in direction of wave motion, 3.1 m s^{-1}, was accounted for.

Wave mode	Simulated speed (m s^{-1})	Predicted speed (m s^{-1})
$n = 1$	30.7	29.4
$n = 2$	13.7	14.7
$n = 3$	7.9	9.8
$n = 4$	4.1	7.4

To confirm that these features were indeed gravity waves of mode n = 1, 2, 3, and 4, their speeds were tracked throughout the simulation. Those speeds, and the predicted wave speeds using (2.1), the mean N of the initial sounding, 7.8×10^{-3} s^{-1}, and a tropospheric depth of 12 km, are given in Table 4.2. The simulated values are fairly close to predicted,

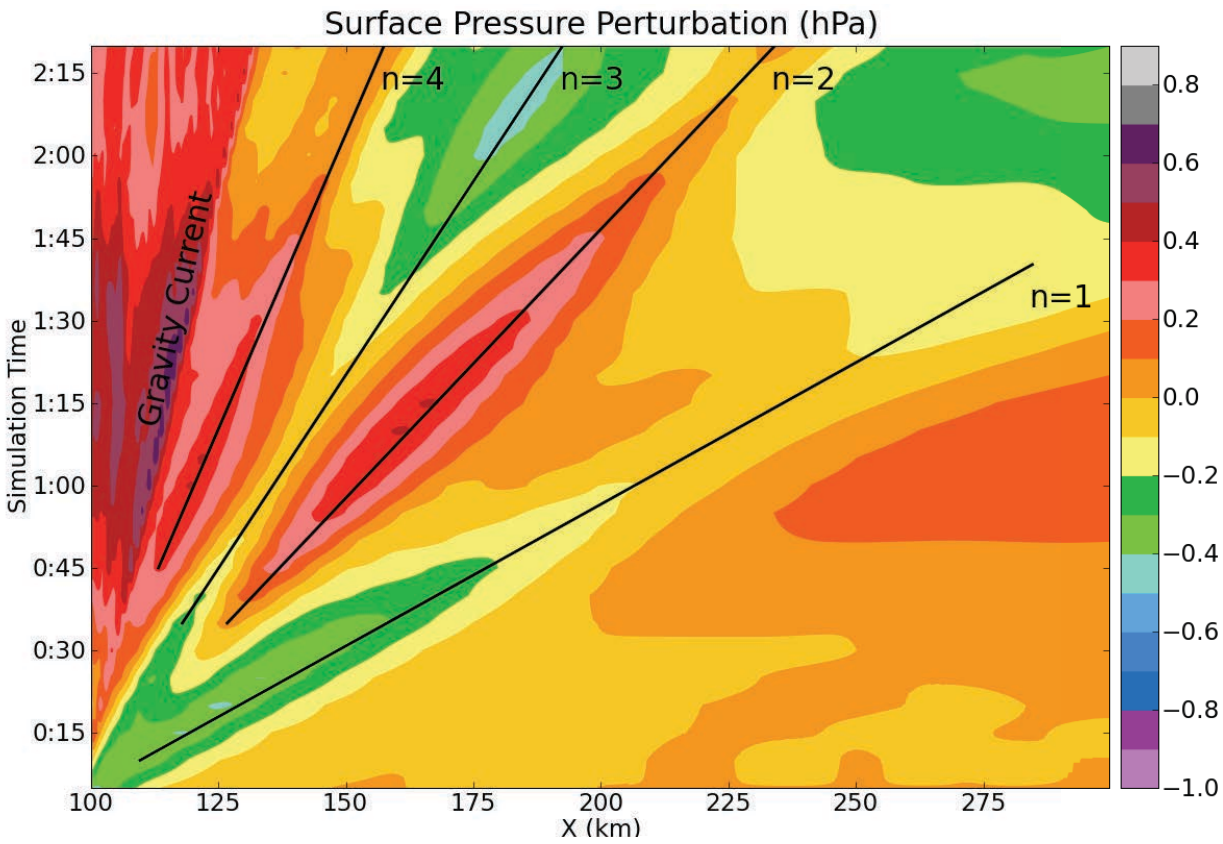

Figure 4.4: Hovmöller diagram of surface pressure (hPa) in the same x-cross-section as shown in Fig. 4.3. Four black lines mark the four gravity waves discussed in Fig. 4.3. The advancing cold pool is marked by the text "Gravity Current".

particularly considering the $n = 1$ and 2 waves would have modified the mean wind and stability profile the $n = 3$ and 4 waves were propagating through.

The statistical method described in Section 4.1.2 correctly predicted the sign and mode of the first four waves in the simulation. It also predicted the existence of $n = 5$, 8 and 10 wave modes. However, the gravity current generated by the cooling in this dry run was moving at a speed of 4.1 m s^{-1}. These other, slower moving waves were likely overtaken by the gravity current, at least at low levels. Fig. 4.4 displays a Hovmöller diagram of surface pressure over the same cross-section shown in the previous figures. The surface pressure response of the $n = 1$ through 4 waves and the gravity current are easily visible, suggesting this is a plausible explanation.

Between the gravity current and the $n = 4$ wave, between 1:35 and 1:50, there is another

signal of increased pressure that has approximately the same speed as a $n = 5$ gravity wave. However, because that wave could not be easily identified in the pressure and temperature perturbation fields aloft (Fig. 4.3), it was not included in this analysis.

4.2.2 Environmental effects

Lane and Reeder (2001) evaluated the effect of low-frequency gravity waves like these on the pre-storm environment. As noted in Chapter 2, they found that the first wave mode, $n = 1$, had the largest effect on CAPE, as it contained vertical motion throughout the column. Higher waves modes, such as $n = 3$, have a larger effect on the CIN, as the largest vertical motions are in the subcloud layer. To compare these results, Hovmöller diagrams of CAPE and CIN were constructed and are displayed in Fig. 4.5. These fields were calculated assuming a surface mixing ratio value unchanged from the initial sounding; as the simulations were dry no moisture values were reported.

None of the gravity waves affected either field as much as they did in Lane and Reeder (2001). The $n = 1$ wave mode did indeed have the largest effect on the CAPE field, but even this was only about 2% compared to the initial CAPE field. Lane and Reeder saw a 15% modification, and even in the previous chapter CAPE fields were modified 7% by most of the $n = 1$ waves. As this heating profile was taken from early in the full physics simulation, it is likely weaker, and the subsequent responses weaker as well, compared to the full convective development in Lane and Reeder (2001) and in the previous chapter.

In agreement with Lane and Reeder (2001), the $n = 3$ wave had the strongest effect on the CIN field, increasing it by 1.4 J kg^{-1}. This is not a very large absolute value, but the CIN in the original sounding was only 1.5 J kg^{-1}. The $n = 1$ and 2 waves with peak vertical motions outside the subcloud layer had very little effect. It should be noted that at this stage in the development of the simulated convective line the $n = 3$ wave mode was of positive sign and increased the CIN, while in Lane and Reeder (2001) it was of negative

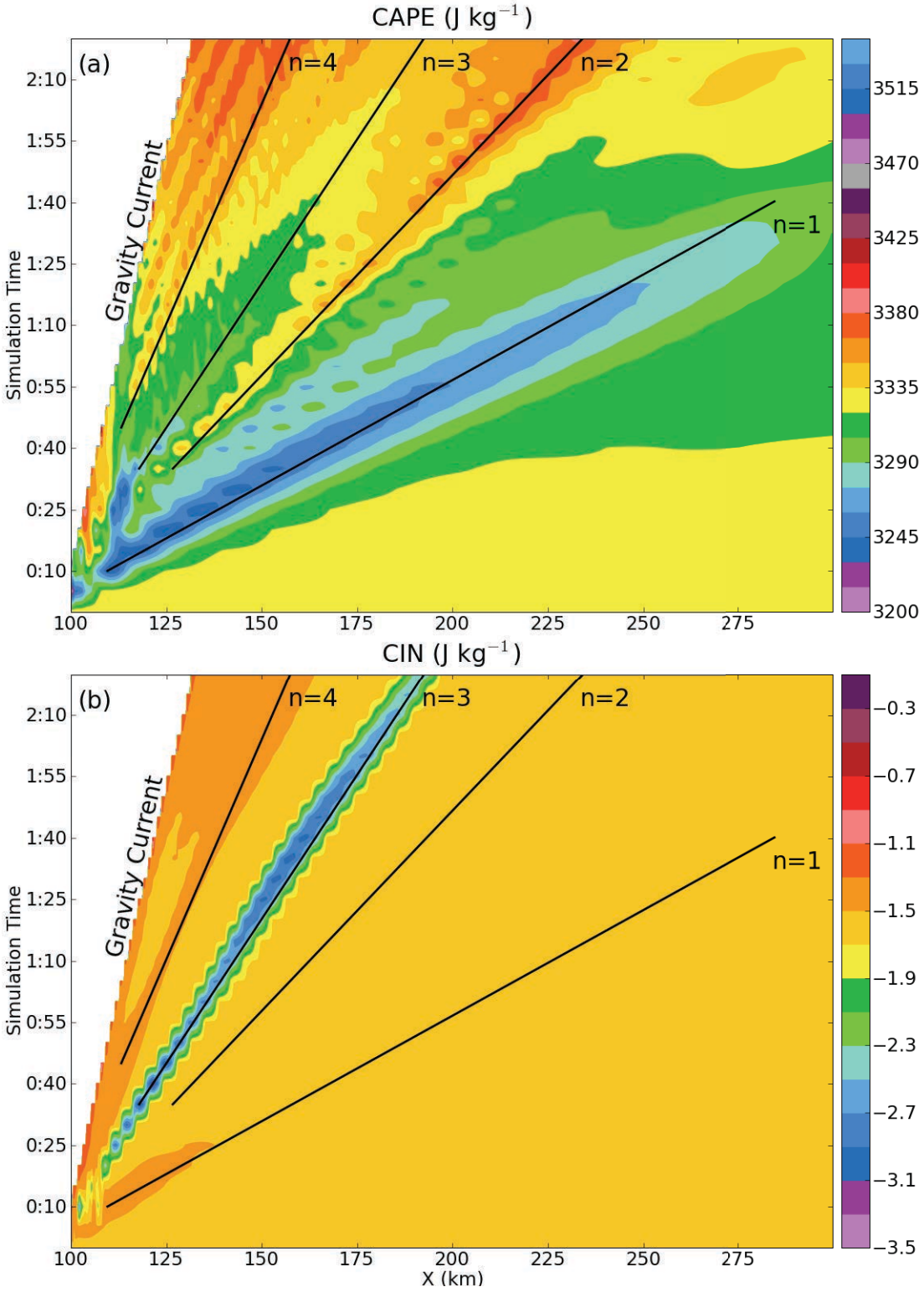

Figure 4.5: As in Fig. 4.4, but of (a) CAPE (J kg^{-1}) and (b) CIN (J kg^{-1}).

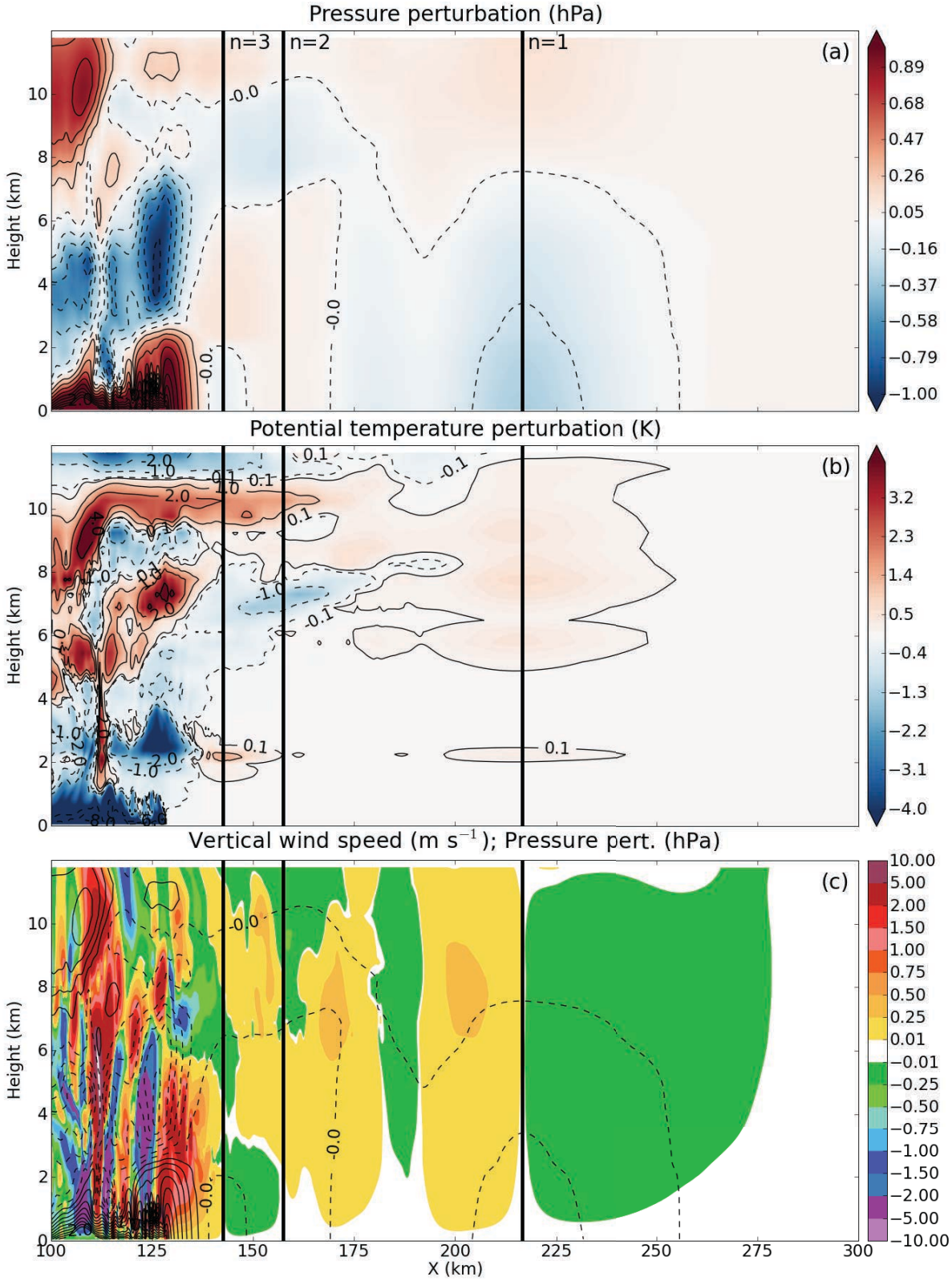

Figure 4.6: *Caption on following page.*

Figure 4.6: *From previous page*: as in Fig. 4.3, but from 0:40 into the surge dry simulation. (a, c) Pressure contours now overlaid every 0.2 hPa. (b) Temperature contours now overlaid at every 2 K, with the addition of -0.1 and 0.1 K. Thick black lines are n = 3, 2, and 1 gravity waves, at x=143, 157, and 217 km, respectively.

sign, decreased the CIN, and was associated with the onset of low-level cooling below the melting level.

4.3 "Surge" dry simulation

The goal of this second simulation was to evaluate the heating profile that generated the pressure surge. Because the vertical profile of the pressure surge in the previous chapter was largely obscured by high-frequency features, using a constant heating profile should provide a clearer picture.

4.3.1 Wave identification and structure

Table 4.3: As in Table 4.1, but for the "surge" mean vertical heating profile.

Vertical mode	Sign
$n = 1$	+
$n = 2$	-
$n = 4$	-
$n = 5$	-
$n = 7$	-
$n = 10$	-

The results of the statistical method discussed in Section 4.1.2 are summarized in Table 4.3. Because the cooling is stronger in this profile, the generated gravity current will move faster, likely overtaking the higher number wave modes. Figures 4.6 and 4.7 display vertical cross-sections of pressure, temperature, and vertical motion from this simulation at 0:40 and 2:00 into the surge dry simulation. Only four total wavelike features are evident in these figures ahead of the gravity current.

As in the early dry simulation, a $n = 1$ wave mode of positive sign exhibits warming

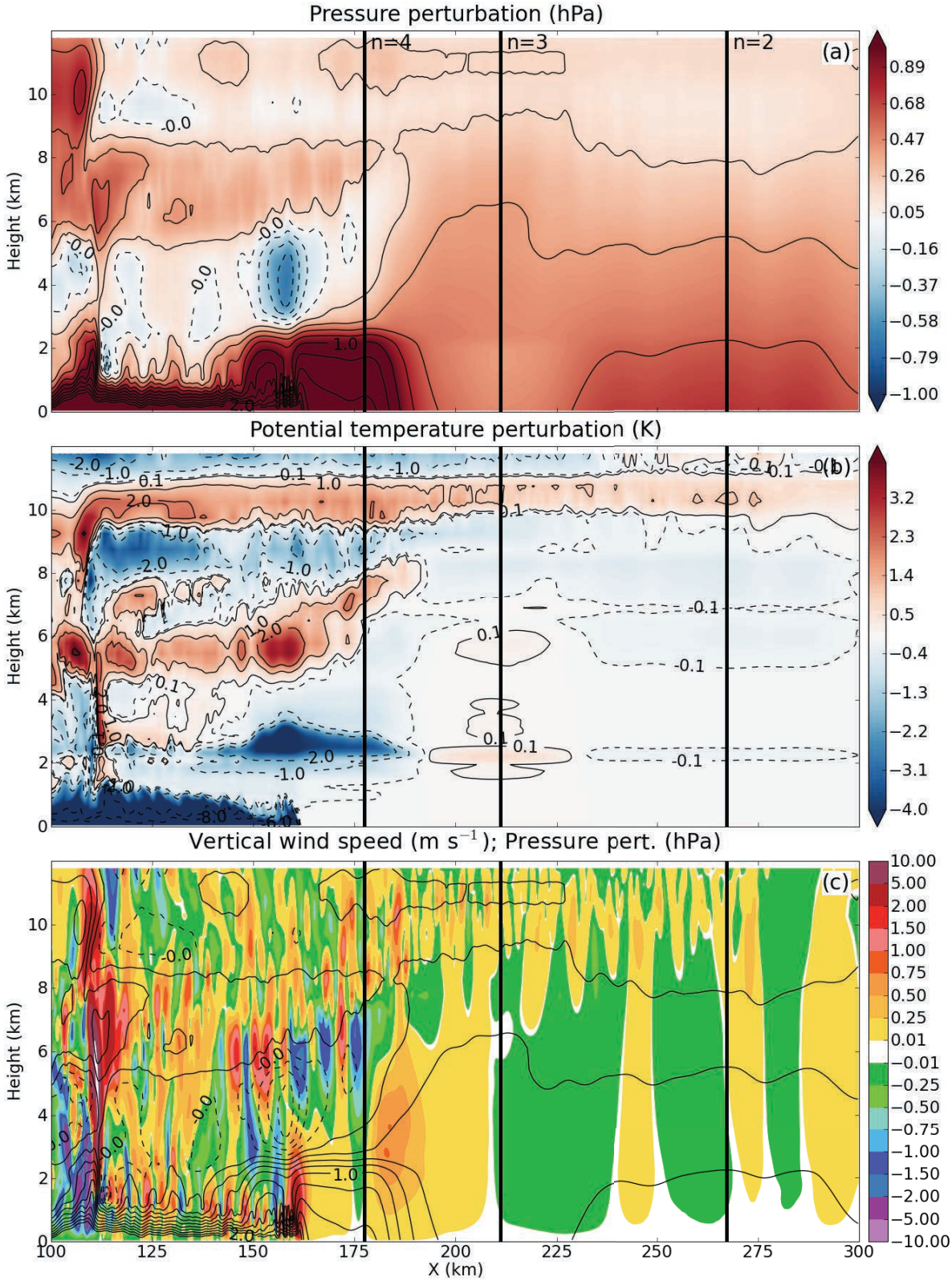

Figure 4.7: As in 4.6, but from 2:00 into the surge dry simulation. Thick black lines are now the $n = 4$, 3, and 2 gravity waves, at x=178, 211, and 267 km, respectively.

throughout the column (Fig. 4.6b), leading downward motion and trailing upward motion (Fig. 4.6c), and low pressure at low levels and high pressure aloft (Fig. 4.6a). An $n = 2$ wave mode of negative sign is less distinct, but cooling and increased surface pressure (Figs. 4.6a, b; 4.7a, b) at low levels is evident.

Despite the statistical method not predicting it, a $n = 3$ wave mode of positive sign is apparent in Figs. 4.6. It is possible the strong low-level heating in the convective line (Fig. 4.1b; approximately x=115 km and 1.5 km aloft) acted to generate this feature despite the strong low-level cooling 10 km rearward. In the one-dimensional mean vertical profile, these were averaged together to a mean cooling at that level, removing the possibility of $n = 3$ positive wave mode generation. This shows the importance of the horizontal distribution of the heating in addition to its vertical distribution, a result similarly noted by Pandya and Durran (1996).

The pressure response of the $n = 3$ wave is negative from 0-2 and 7-10 km, and positive from 2-7 and 10-12 km (Fig. 4.6a); the temperature perturbations are warm in the lower and upper third of the atmosphere, and cool in between (Fig. 4.6b). The wave is led by downward motion in the lower levels (Fig. 4.6c). In Fig. 4.7 these features are not as clear, but decreased pressure, increased temperature, and descent just ahead of the feature and below approximately 3 km is still evident.

Finally, in Fig. 4.7 a feature that appears very similar to the pressure surge discussed in the previous chapter can be seen at x=178 km. The associated positive pressure perturbation extends to approximately 2.5 km aloft (Fig. 4.7a). Cooling is found in the lower levels, associated with a strong updraft at the leading edge of the wave. This feature is unique from the gravity current, which is back at x=160 km.

In the previous chapter, the pressure surge was shown to be generated by low-level cooling, and was hypothesized to be a $n = 3$ wave due to the depth of the increased low-level positive pressure perturbation and its speed. In this simulation, the surge was better defined. It was still generated by low-level cooling, but moved slightly more slowly and could

be identified as a $n = 4$ wave. The difference is likely due to these waves from the dry "surge" simulation being generated by a heating profile selected at one instance in time from the full physics simulation. Within the full physics simulation, it is entirely possible the low-level cooling deepened slightly over time, generating a $n = 3$ wave instead; this appears possible in Fig. 3.11a.

The $n = 4$ wave pressure and temperature perturbations above the low levels were not arranged regularly with height, as would be expected from idealized simulations (Nicholls et al. 1991). This suggests that the high-frequency gravity waves were not the only feature obscuring the low-frequency gravity wave signal in the previous chapter, but the changing stability and wind profile in the pre-storm environment also played a role in modifying these mid- and upper-level perturbations. It is possible that the unstable layer at 2.5 km (Fig. 3.14) acted to partially duct the low-frequency gravity wave response in the full physics simulation, concentrating the perturbations below this level and explaining why the rest of the gravity wave response above 3 km was not seen.

Table 4.4: As in Table 4.2, but for the second dry run simulation. The mean profile N was 8.7×10^{-3} s^{-1}. The mean wind in the direction of wave motion was 4.4 m s^{-1}.

Wave mode	Simulated speed (m s^{-1})	Predicted speed (m s^{-1})
$n = 1$	42.4	33.2
$n = 2$	20.0	16.6
$n = 3$	10.8	11.1
$n = 4$	7.5	8.3

The speeds of these simulated waves were calculated and compared to the speeds calculated using (2.1) and are shown in Table 4.4. The mean stability of the environment, N, was 8.7×10^{-3} s^{-1}. Again, the speeds are fairly close, although the $n = 1$ wave moved almost 10 m s^{-1} faster than the theoretically predicted speed. However, the vertical structure of that feature clearly delineates it as a $n = 1$ wave. The gravity current was moving at a speed of 7.5 m s^{-1}, ensuring that all wave modes higher tha $n = 4$ would be overtaken or difficult to

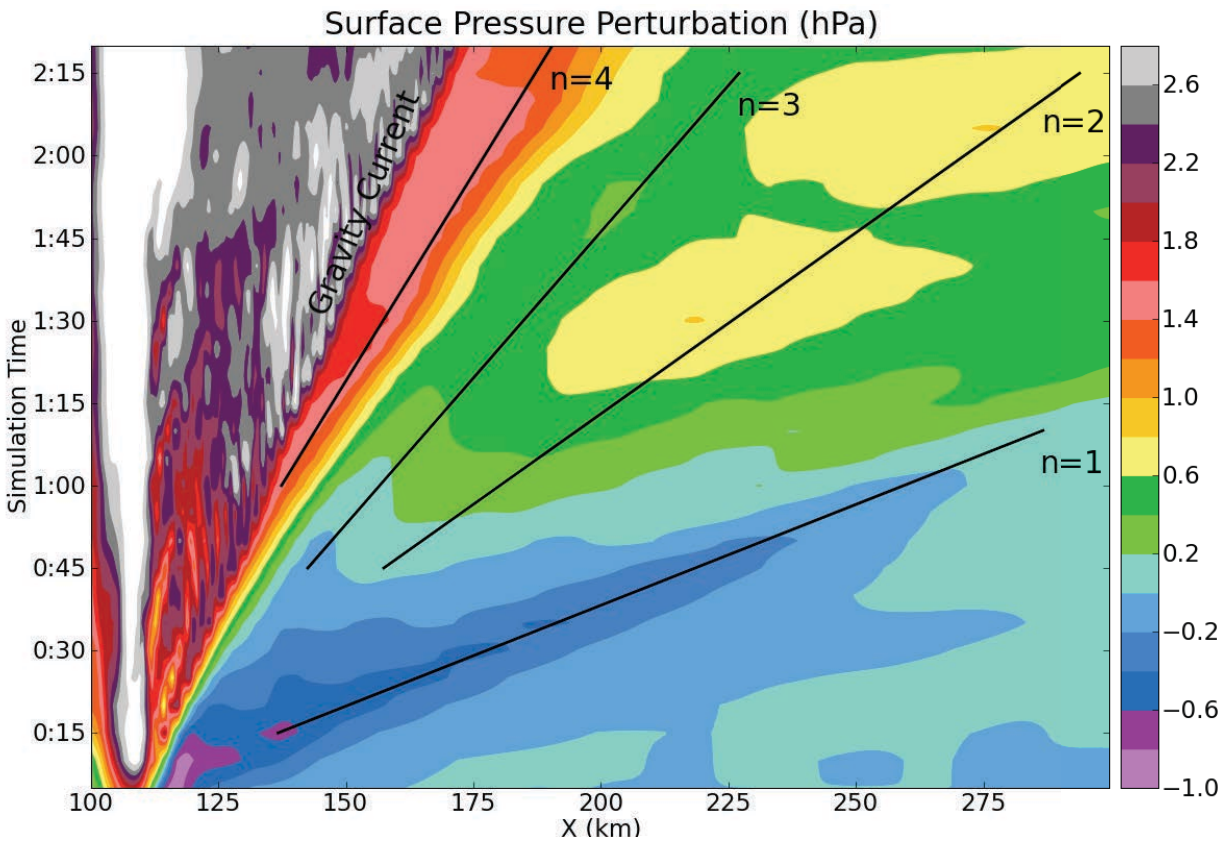

Figure 4.8: As in Fig. 4.4, but for the second dry run simulation.

distinguish from the gravity current. (The $n = 4$ wave moved at a speed of 11.0 m s^{-1} when the mean wind was included).

Fig. 4.8 shows a Hovmöller diagram of surface pressure across the same cross-section as Figs. 4.6 and 4.7. The signature of all four waves are evident, and are marked by thin black lines on the figure. No waves between the $n = 4$ wave and the gravity current are visible.

4.3.2 Environmental effects

Because the sounding used to initialize the surge dry simulation (Fig. 4.2) had almost no CIN associated with it, minimal modifications to the CIN field were possible. However, modifications to the CAPE field did occur, and are shown in Fig. 4.9. Here, the $n = 1$ and $n = 4$ waves both affected the CAPE field approximately equally, by about 3% of CAPE in the original sounding. The large effect of the $n = 4$ wave was partially due to the

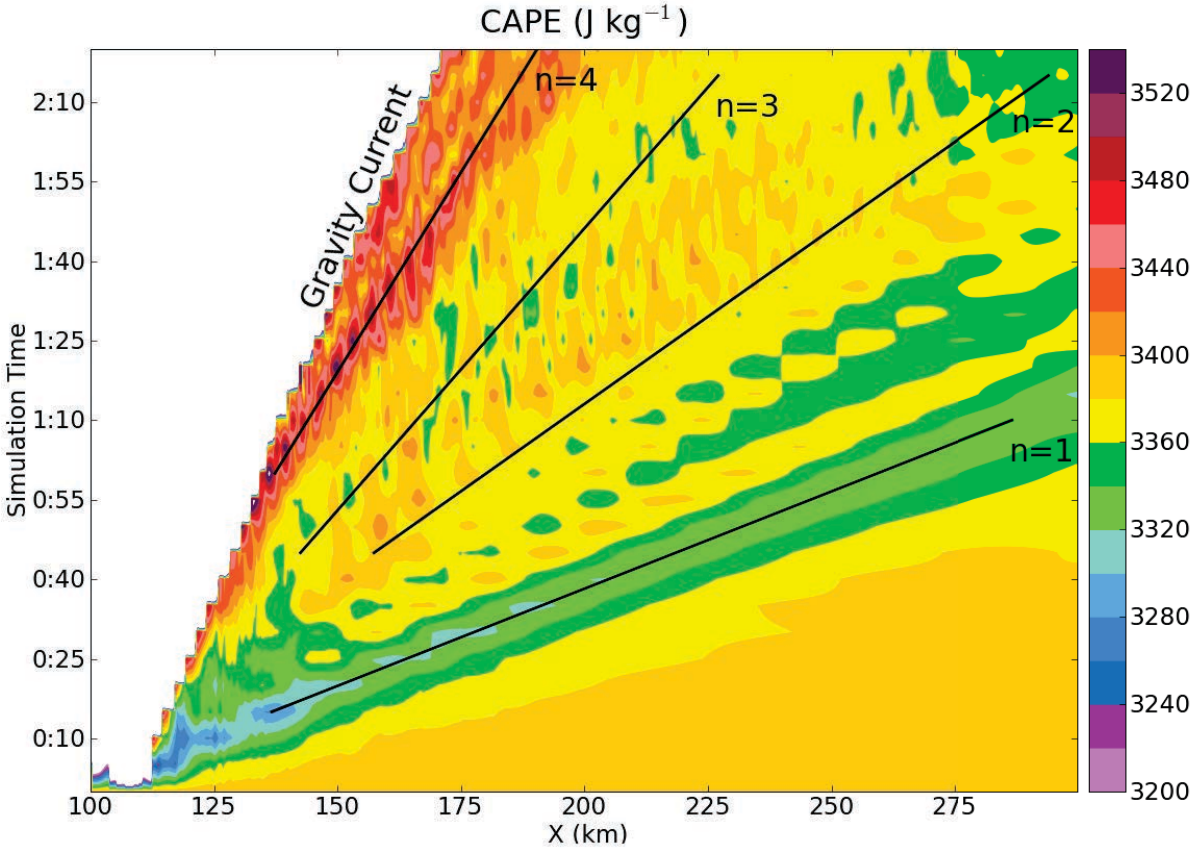

Figure 4.9: As in Fig. 4.5, but of CAPE (J kg^{-1}) for the second dry run simulation.

upward motion associated with it being strongest compared to the other three waves, with perturbations up to 1 m s^{-1} (Fig. 4.7c).

4.4 Summary

Two two-dimensional microphysical heating profiles from the full physics simulation discussed in Chapter 3 were each placed as a constant, stationary heat source within a dry CM1 simulation. The first heating profile was from early in the full physics simulation, shortly after development of a $n = 1$ wave, and the second from immediately prior to the development of the pressure surge. The goal was to evaluate what gravity waves would be generated from a microphysical heating profile alone, without higher-frequency features generated by temporal heating fluctuations.

The dry simulation with the heating profile from early in the convective lifecycle, or

"early", produced four unique gravity waves, $n = 1$, 2, 3, and 4. The $n = 1$ and 3 wave modes were associated with low pressure at the surface; the $n = 2$ and 4 waves had high surface pressure perturbations. Each developed the vertical temperature and pressure structure expected from theory (Nicholls et al. 1991; Lane and Reeder 2001), and the waves moved at speeds similar to theoretically predicted speeds. The $n = 1$ wave affected the ambient CAPE field the most, decreasing it by 2%. CIN was minimally affected by any of the four waves.

The dry simulation with the "surge" heating profile produced the same four types of gravity waves. The $n = 4$ wave generated a surface pressure surge very similar to the pressure surge observed in the full physics simulation, and was also generated by low-level cooling. The full, regularly space vertical temperature and pressure structure of the $n = 4$ wave was not visible; changes in environmental stability and wind with respect to height served to modify the perturbations as effectively as the high-frequency waves in the previous chapter. However, the low-level updraft associated with the $n = 4$ wave increased the ambient CAPE by approximately 3%.

A one-dimensional mean vertical heating profile was calculated from each two-dimensional profile. Multiple linear regression was used to evaluate the significance of each harmonic mode within the heating profile. In the "early" dry simulation the method correctly predicted all four waves and their phase. In the "surge" dry simulation the method failed to predict the $n = 3$ wave. The heating profile at that point had become more complex horizontally; a mean vertical profile was no longer a good representative. The horizontal variations in the heating profile appeared to act independently to generate unique gravity waves.

Chapter 5 evaluates more direct effects changes in the horizontal distribution of the microphysical heating profile have on a bow echo system.

CHAPTER 5
IMPACT OF GRAUPEL PARAMETERIZATION SCHEMES ON IDEALIZED BOW ECHO

Within this chapter, a cloud-resolving model is used to examine the impacts of microphysical variations specifically on bow echoes. The sensitivity of new bowing development to changes in microphysical heating and cooling rates will be investigated, particularly through their relation to cold pool strength and depth, the mid-level thermal and pressure gradients within the system, and the stratiform region microphysical structure.

Section 5.1 describes the experiment and model design, as well as the specific microphysics variations. Sections 5.2 and 5.3 contain results from two different sensitivity studies. Section 5.4 presents a summary.

5.1 Methodology

5.1.1 Model description

The Advanced Research Weather Research and Forecasting (WRF-ARW) model is widely recognized as a reliable tool for simulations of mesoscale phenomena (Skamarock et al. 2008). Here version 3.2.1 was used to simulate a bow echo case over Oklahoma. The model horizontal grid spacing was 1 km, with 72 stretched vertical levels. In total, the domain extended 600 km in the x direction, 400 km in the y direction, and to 100 hPa vertically. Rayleigh damping was applied over the top 5 km of the atmosphere, with a damping coefficient of 0.003. The x and y boundaries were open, and no random perturbations were utilized. No convective, boundary layer, radiative, or land-surface parameterizations were used. A 1.5 order TKE closure turbulence parameterization was selected. No surface friction was applied within the model, as in the Weisman (1992) and (1993) studies; surface wind speeds and gravity current propagation will be somewhat faster than expected.

The 0000 UTC 13 March 2003 KOUN sounding (Fig. 3.4) provided the homogenous initial conditions. This sounding was chosen from among multiple case study simulations after tests showed a strong sensitivity of the bow to microphysics changes. This sensitivity is likely due to relatively weak line-normal wind shear for this modified sounding, with a large surface-based convective available potential energy (CAPE), 3752 J kg^{-1}. The low-level 0-2.5 km shear was 14 m s^{-1}, and 0-5 km layer shear 14.2 m s^{-1}. The convective inhibition (CIN) was just 6 J kg^{-1}.

Other than extrapolation of moisture data at upper levels and minimal cooling to remove unstable layers, the sounding was unmodified. (The unstable layers were removed from the base state sounding to prevent convective overturning immediately upon simulation start.) The observed convection formed along a southwest-northeast line approximately 60° clockwise of vertical. The sounding was not rotated in the idealized simulation, and the idealized convection was initiated along a south-north line. The line-normal wind shear values given above are for this idealized convection.

The simulations were run for six hours. The "cold pool-dam break" initialization scheme, used by Weisman et al. (1997), was modified for these simulations. A "cold dam" of air was created by decreasing the initial potential temperature in the domain, from 0 to 200 km in the x-direction, and 50 to 350 km in the y-direction. The magnitude of the perturbation was 6 K at the surface, and linearly decreased until reaching 0 K, 2.5 km aloft. Upon simulation start, the "dam" of cold air would break, surging forward as a gravity current. Air in advance of the gravity current would be forced upward, initiating convective activity. This initialization method was specifically chosen due to the low-level stable layer in the initial sounding (Fig. 3.4). This stable layer acted as a cap and required a larger amount of forcing to be overcome than would be provided by a warm bubble initialization. In every simulation, cold pool perturbations significantly colder than the initial 6 K developed within one hour; within two hours negative perturbations of 10 to 14 K were common.

5.1.2 Model microphysics and experiment design

A total of six sensitivity tests were performed using the WRF Single-Moment 5- and 6-class microphysics schemes (Hong et al. 2004; Hong and Lim 2006; Lim and Hong 2010), with the goal of examining how modifying the graupel microphysics class affects bowing development.

These schemes are originally based upon the techniques used in Lin et al. (1983) and Rutledge and Hobbs (1983). The 5-class schemes contain explicit classes for water vapor, cloud water, raindrops, cloud ice, and snow; the 6-class schemes add graupel. All of these schemes utilize an inverse exponential Marshall-Palmer size distribution (Marshall and Palmer 1948) for rain, snow, and, for the 6-class, graupel:

$$n_x(D_x)dD_x = n_{0x}exp(-\lambda_x D_x)dD_x \tag{5.1}$$

where x is the microphysics class, $n_x(D_x)dD_x$ is the number of hydrometeors per cubic meter with diameters between D_x and $D_x + dD_x$, n_{0x} is the distribution intercept, and λ_x is the slope. Within these schemes, the distribution intercept is set to a constant value. The slope is a diagnosed value, defined as:

$$\lambda_x = \left(\frac{\pi \rho_x n_{0x}}{\rho q_x}\right)^{0.25} \tag{5.2}$$

where ρ_x is the pre-assigned hydrometeor density (kg m^{-3}), ρ (kg m^{-3}) is the local air density, and q_x (kg kg^{-1}) is the prognostic hydrometeor mixing ratio.

From (5.1) and (5.2), it can be seen that the size distribution of a hydrometeor is a function of n_{0x} and λ_x. Due to the inverse nature of the distribution, with all other factors held constant, a large intercept will result in a smaller mean hydrometeor size, and vice versa. In general, graupel hydrometeors have a smaller mean hydrometeor size (larger intercept) and are less dense, while hail stones have a larger mean hydrometeor size (smaller intercept) and are more dense, but there is quite a bit of overlap between the two in observed data. Gilmore

Table 5.1: Names of model simulations with the intercept value (n_{0G}), density (ρ_G), and fallspeed parameters (a_G, b_G) used in the hail/graupel comparison experiment, and graupel removal experiment. The default values in WSM6 are those of the "graupel" simulation.

Simulation name	Microphysics scheme	Intercept (n_{0G}) m^{-4}	Density (ρ_G) kg m^{-3}	fallspeed coefficient (a_g)	fallspeed coefficient (b_g)
First experiment: hail/graupel comparison					
"hail-like"	WSM6	4×10^2	900	330	0.8
"mid"	WSM6	4×10^4	700	285	0.8
"graupel-like"	WSM6	4×10^6	300	270	0.8
"fast graupel"	WSM6	4×10^6	300	1700	0.8
Second experiment: removal of graupel class					
"no-graupel"	WSM5	—	—	—	—
"graupel"	WSM6	4×10^6	500	330	0.8

et al. (2004a) provided an excellent summary of previous observations of these values: the intercept value for hail and graupel ranged from 10^2 m^{-4} for large hail, to 10^{10} m^{-4} for extremely small graupel (Cheng et al. 1985, Dennis et al. 1971; Federer and Waldvogel 1975; Spahn 1976; Knight et al. 1982). Observations of graupel density ranged from 50 to 890 kg m^{-3}; hail density varied from 700 to 900 kg m^{-3} (Pruppacher and Klett 1978).

In the first experiment, model runs are performed using the WSM6 scheme, but covering this observed range of intercept parameters and densities. The most "hail-like" hydrometeor has an intercept equal to 4×10^2 m^{-4} and a density of 900 kg m^{-3}; the most "graupel-like" hydrometeor an intercept of 4×10^6 m^{-4} and a density of 300 kg m^{-3}; and the "mid" simulation an intercept of 4×10^4 m^{-4} and a density of 700 kg m^{-3}. A plot of the graupel hydrometeor size distributions given the chosen intercepts and densities is shown in Fig. 5.1a. A full list of the microphysical schemes and associated parameters used in each simulation is provided in Table 5.1.

Within these schemes, an increase in density alone acts to actually decrease the mass-weighted mean terminal velocity. This value is calculated for graupel through the following (Hong and Lim 2006):

$$v_g = \frac{a_g \Gamma(4+b_g)}{6} \left(\frac{\rho_0}{\rho}\right)^{1/2} \frac{1}{\lambda_g^{b_g}} \tag{5.3}$$

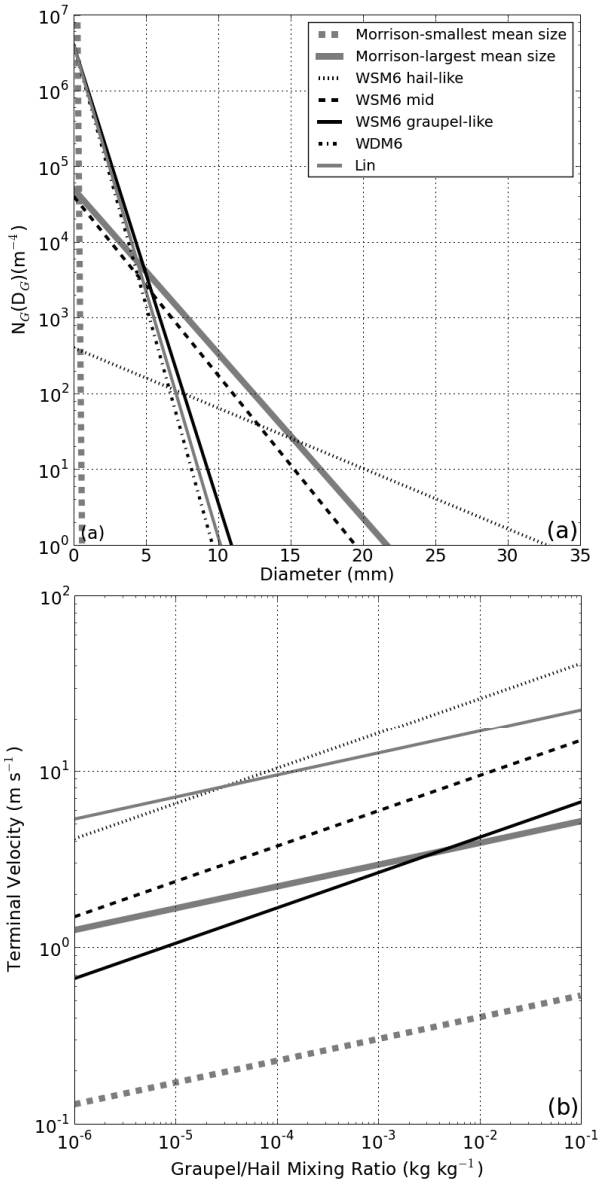

Figure 5.1: (a) Graupel hydrometeor size distributions for the model runs given in Table 1. This assumes a graupel mixing ratio of 1 g kg^{-1} and air density of 1 kg m^{-3}. (b) Mass-weighted mean graupel hydrometeor terminal velocity (m s^{-1}) for a range of graupel mixing ratios (kg kg^{-1}) as a function of four different schemes. Temperature is fixed at 268.15 K, and pressure at 900 hPa. The "fast graupel" fallspeed is equivalent to that of the "hail-like" system. The Morrison fallspeed uses the single-moment Morrison scheme described in Bryan and Morrison (2012).

where a_g and b_g are empirically-determined coefficients, set to 330 and 0.8, respectively, within the WSM6 scheme (Hong et al. 2009). An increase in graupel hydrometeor density with all other factors held constant results in an increased slope value through (5.2), yielding a smaller mean terminal velocity. This is different than the microphysics scheme used in Gilmore et al. (2004a), in which the fallspeed was directly proportional to the hydrometeor density (Gilmore et al. 2004b). To account for this unphysical effect, the a_g empirical coefficient was modified slightly to negate the fallspeed decrease caused by the density changes. A list of these values is provided in Table 1. Figure 5.1b displays mass-weighted terminal velocity for each run for a range of graupel mixing ratios, using these new values for a_g.

Previous studies have evaluated the difference in hail and graupel simulations by using a double-moment graupel distribution and modifying the fallspeed parameters of that class (Bryan and Morrison 2012; van Weverberg et al. 2011a, 2012; Milbrand and Morrison 2011). In this study, a microphysics scheme with a single-moment graupel class with a fixed distribution intercept (N_0) was purposefully chosen to allow direct manipulation of the size distribution through that value, as it is hypothesized that both mean hydrometeor size and fallspeed should have an effect. Within Bryan and Morrison (2012), the differences between the faster- and slower-falling graupel simulations were evident in both the one- and two-moment tests, suggesting comparison among this studys single-moment sensitivity tests should still be instructive.

It is evident from Fig. 5.1a and (5.2) that a decrease in the hydrometeor intercept yields an overall increase in the number of large hydrometeors while decreasing the number of small hydrometeors, all else being equal. This change in mean hydrometeor size will increase the mean terminal velocity of the distribution. This will result in less residence time in the downdraft, and increased downward precipitation flux (Gilmore et al. 2004a), but also less time for melting and evaporation. Larger hydrometeors have less surface area-to-volume ratio, which can also reduce the melting and evaporation rates (van den Heever and Cotton 2004). In order to examine the relative contributions of reduced mean size and reduced fallspeed,

another sensitivity test was designed that contains a large graupel intercept parameter and small mean size, but with fast fallspeeds. This test is termed "fast graupel", and its specific parameters are also given in Table 1.

Separate tests were conducted varying the graupel density in isolation, but little effect was found on the bowing and convective development within the simulations, similar to the results noted in Bryan and Morrison (2012).

In the second experiment, a comparison of the 5- and 6-class schemes is used to examine the importance of graupel as a class in simulating this type of convective system. These will be termed the "graupel" and "no-graupel" simulations, and were run using the WRF Single-Moment 5- and 6-class schemes.

5.2 Results from hail-graupel comparison

Deep convection initiated almost immediately in all five simulations as the cold dam began propagating "east"-ward. By two hours into these simulations, a mesoscale convective system structure with convective line and minimal stratiform precipitation region had appeared (not shown). By 2:35 (2 h 35 min), the stratiform precipitation predominately trailed the convective line in all simulations.

The convective line in each simulation began to bow at 2:40, 2:50, 3:00, and 2:20 simulation time in the "graupel-like", "mid", "hail-like", and "fast graupel" simulations, respectively. All four systems as they started to bow are shown in Fig. 5.2. Figure 5.2 also is representative of the differences in these systems throughout each simulation. The "graupel-like" system was more extensive, with high reflectivities even in the stratiform region. The convective line was over 20 km wider than that of the "hail-like" system, similar to Bryan and Morrison (2012), and contained peak reflectivities approximately 5 dBZ higher. There was also no clear "transition zone" or region of lesser reflectivity between the convective line and the more intense stratiform region (Fig. 5.2a), which is unrealistic compared to typical observed squall lines (Biggerstaff and Houze 1991, 1993), but generally expected with single-

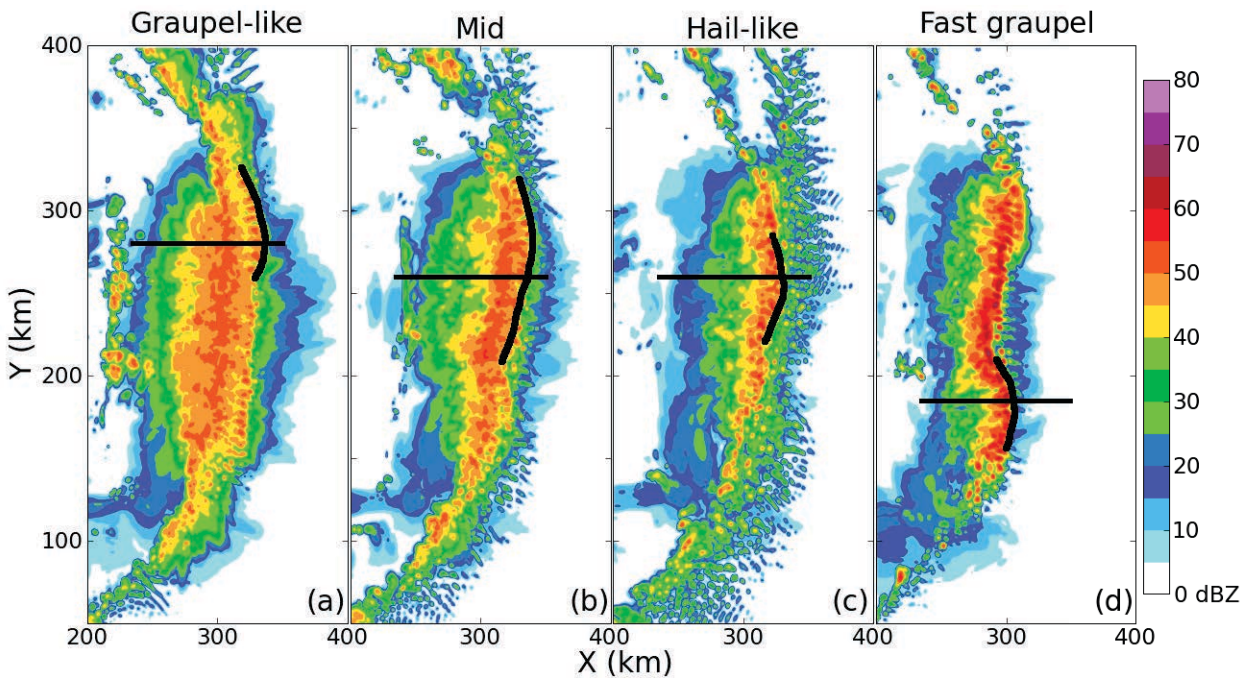

Figure 5.2: Simulated composite reflectivity for the "graupel-like" (a), "mid" (b), "hail-like", and (d) "fast graupel" systems as they each begin to bow, at 2:40, 2:50, 3:00, and 2:20 simulation time, respectively. Thick black lines delineate bowing segments. Thin black lines show location of later vertical cross-section figures. Simulated composite reflectivity calculated as in Stoelinga (2005), but modified to use the WSM6 scheme's temperature-dependent snow intercept parameter.

moment microphysics schemes (Bryan and Morrison 2012). The "mid" system contained stratiform precipitation over about the same area, but of much weaker intensity (Fig. 5.2b). The stratiform regions of the "hail-like" and "fast graupel" systems covered the smallest area and were less intense (Fig. 5.2c,d), although the "fast graupel" convective line was most intense of any simulation (Fig. 5.2d).

The "fast graupel" system began bowing first, followed by the"graupel-like", "mid" and "hail-like" systems at 2:20, 2:40, 2:50 and 3:00, respectively. Reasons for this distinction will be discussed in the following paragraphs. Significant differences were also observed in the mean system speed, determined by cold pool position: the "fast graupel" (23.1 m s^{-1}), "graupel-like", (21.4 m s^{-1}) and "mid" (18.7 m s^{-1}) systems were all faster than the "hail-like" system (16.7 m s^{-1}). All of the systems continued bowing through the end of the run time (not shown).

5.2.1 System-relative rear-to-front flow

As this work is primarily interested in the behavior of the system while bowing, vertical cross-sections will be examined through the region of the storm that later exhibits bowing development. Similar behavior can be seen throughout the segment of the line that bows. Along-line averaging was performed 5 km on either side of the chosen cross-section (shown in Fig. 5.2). Rear-to-front system-relative flow first appeared in the "fast graupel" system at 1:30, the "graupel-like" system at 1:40, then "mid" at 1:45, and finally the "hail-like" system at 2:15 (not shown). The mid-level (3-6 km) low pressure region formed in each system in the same order. The "fast graupel" ("hail-like") system's low pressure region was most (least) intense; causes of this different pressure perturbation strength will be discussed in more detail in the next section.

Immediately after its formation, the rear-to-front flow in each case was located only immediately rearward of the updraft, and at the lowest levels in the simulation. As each run progressed the rear-to-front flow extended farther to the rear of the storm, similar to the gravity wave-generated rear-to-front flow in Pandya and Durran (1996) and Pandya et al. (2000). Shortly before each system bowed, this flow became more evident (Fig. 5.3). In the "graupel-like" system, this rear-to-front flow was spread along the surface within the stratiform region; little ambient airflow into the rear of the system occurred nor descent from aloft (Fig. 5.3a). The same was true of the flow in the "fast graupel" system, although the rear-to-front flow was weaker, and concentrated closer behind the convective line.

In the "mid" system, the rear-to-front flow began aloft in the rear of the stratiform region just below the melting level, and descended to the surface fairly quickly approximately 25 km behind the convective updraft (Fig. 5.3b). The rear-to-front flow in the "hail-like" system began in the same place as the "mid" system, but remained aloft until immediately before the convective updraft, and then descended to the surface (Fig. 5.3a). These simulations agree with results noted by Lafore and Moncrieff (1989), Weisman (1992), and Pandya and Durran (1996) that rear-to-front flow in systems with extensive stratiform precipitation and

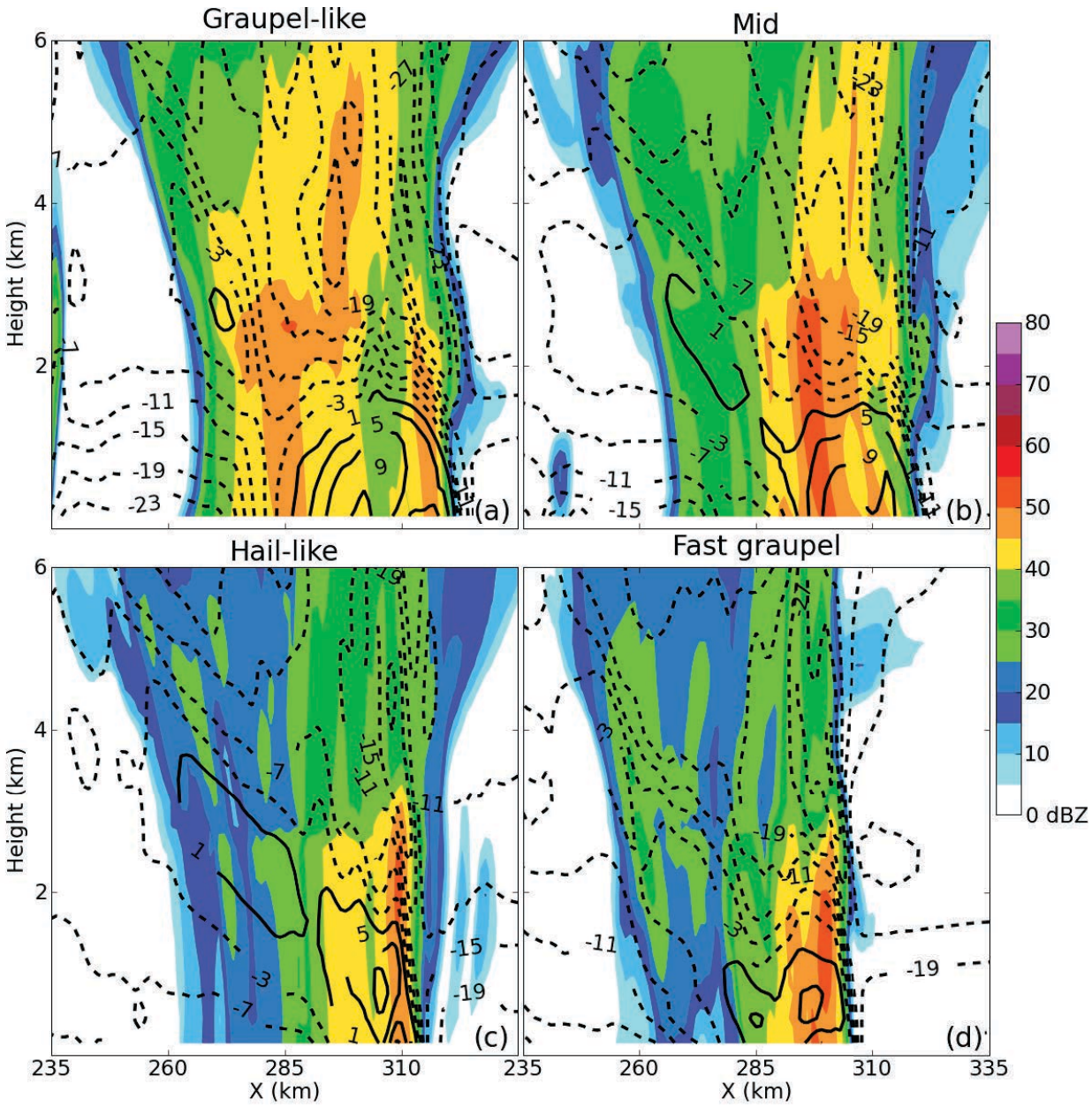

Figure 5.3: 0-6 km vertical cross-sections of the "graupel-like" (a), "mid" (b), "hail-like" (c), and "fast graupel" (d) systems, at the time each developed significant system-relative rear-to-front flow: 2:30, 2:35, 2:45, and 2:20 simulation time, respectively. These cross-sections are taken along the black line shown in Fig. 5.2; plotted values are averages 5 km either side of the cross-section. Simulated reflectivity (color) and storm-relative line-normal winds in the plane of the cross-section (black contours, 4 m s^{-1}, negative dashed) are shown.

microphysical cooling remains closer to the surface much farther rearward of the convective line.

The peak rear-to-front flows in this study were even shallower than those observed by Lafore and Moncrieff (below 1 km as opposed to approximately 3 km; see their Fig. 11b). A significantly different microphysics scheme was used in the Lafore and Moncrieff simulations. Highly altered evaporation and melting rates, and therefore dissimilar low-level stratiform vertical motion and resultant depth of rear-to-front flow, are possible. The lack of surface friction and boundary layer parameterization in this simulation could also have had an effect. In any case, rear-to-front flow which extends to the surface farther behind the convective line, at least temporarily, appears to be associated with new bowing development as it aids the necessary updraft tilt of the convective line (Weisman 1993; Weisman and Rotunno 2005; James et al. 2006). While systems with surface-based rear-to-front flow are expected to dissipate more quickly than systems with elevated rear inflow, that does not preclude them from initiating bowing development more quickly as well (Weisman 1992; Weisman 1993; James et al. 2006).

5.2.2 Mid-level pressure and buoyancy perturbations

The mid-level pressure perturbation can be related to the buoyancy gradient with respect to height through

$$\frac{1}{\rho_0}\nabla^2 p' = -\nabla \cdot (\vec{v} \cdot \nabla \vec{v}) + \frac{\partial B}{\partial z} \tag{5.4}$$

where p' is the perturbation pressure, $\vec{v}$ is the horizontal wind vector, and B is buoyancy. Buoyancy is calculated as in 3.1. The mid-level buoyancy gradient is typically positive, due to the warmer updraft overlying the cold pool. Thus, a system with an intense and deep cold pool would also have a strong vertical buoyancy gradient and lower pressure at mid-levels.

Cross-sections of hydrometeor mixing ratios (Fig. 5.4), cooling rates (Fig. 5.5), and vertical motion and pressure perturbation (Fig. 5.6) are shown from all four simulations at the time of new bowing development in each. Vertically integrated changes in temperature due

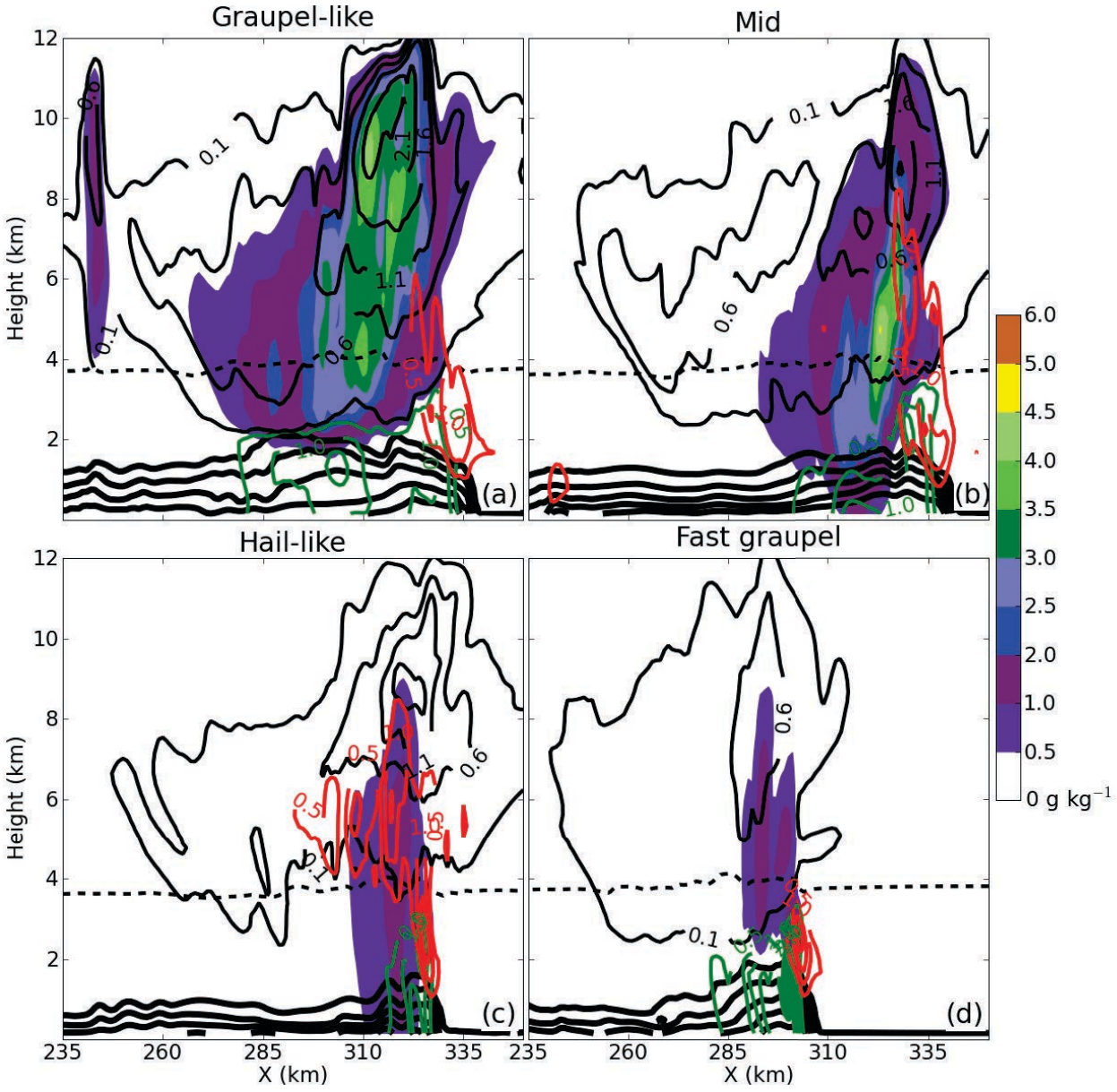

Figure 5.4: Mixing ratios (g kg^{-1}) are of graupel (color), cloud water and ice (red, 0.5 g kg^{-1}), rain water (green, 0.5 g kg^{-1}), and snow (thin black, 0.5 g kg^{-1}); the thick solid black lines are cold pool potential temperature perturbation contours every 2 K. Thin dashed black line is the melting level. Vertical cross-sections as in Fig. 5.3, but from 0 to 12 km.

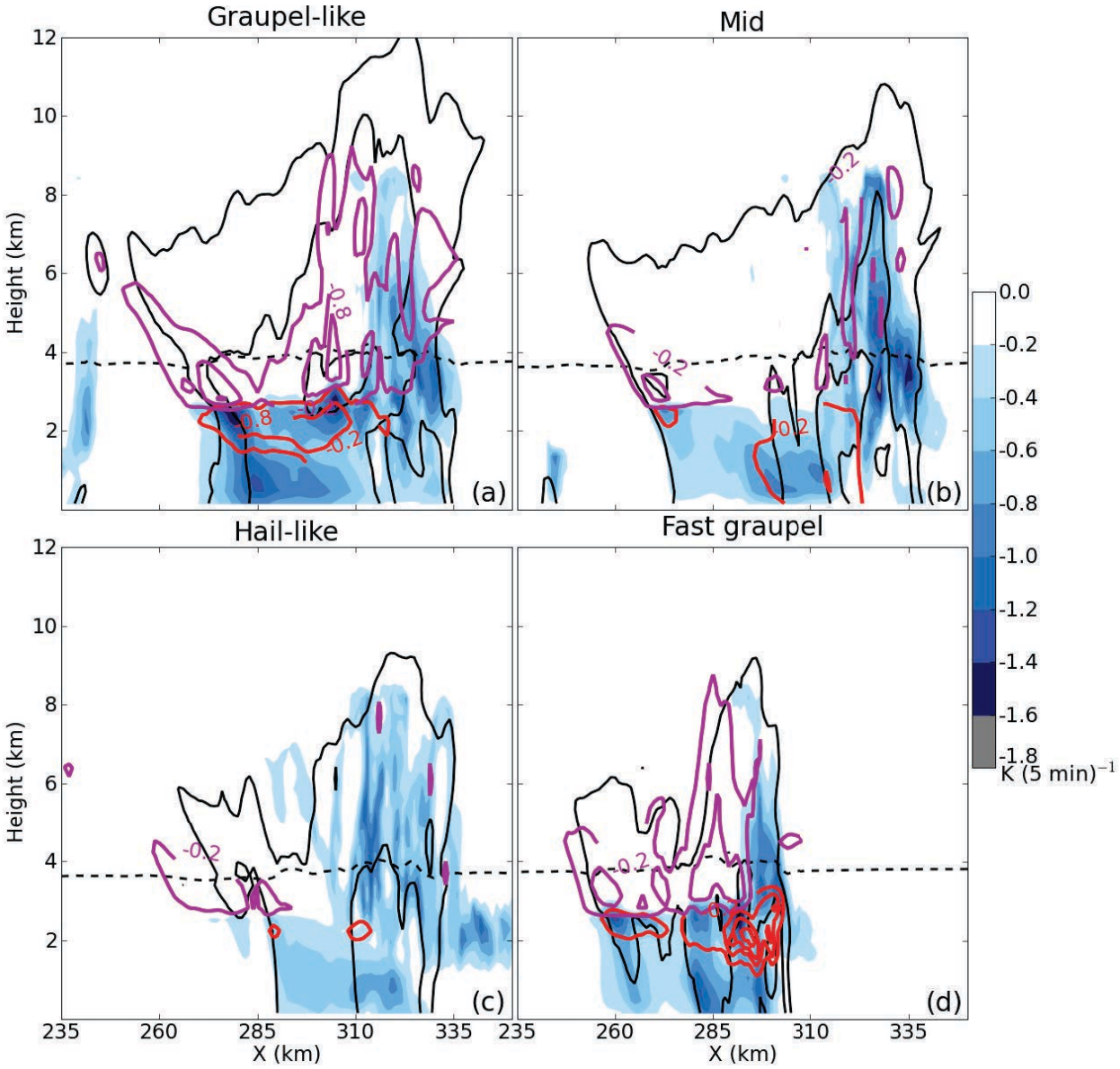

Figure 5.5: Cooling rates (K (5 min)$^{-1}$) of evaporation (blue image), melting (red, 0.6K (5 min)$^{-1}$), and sublimation (purple, 0.6K (5 min)$^{-1}$). Thick solid black lines are the simulated reflectivity at 25, 40, and 50 dBZ. Thin dashed black line is the melting level. Vertical cross-sections as in Fig. 5.4.

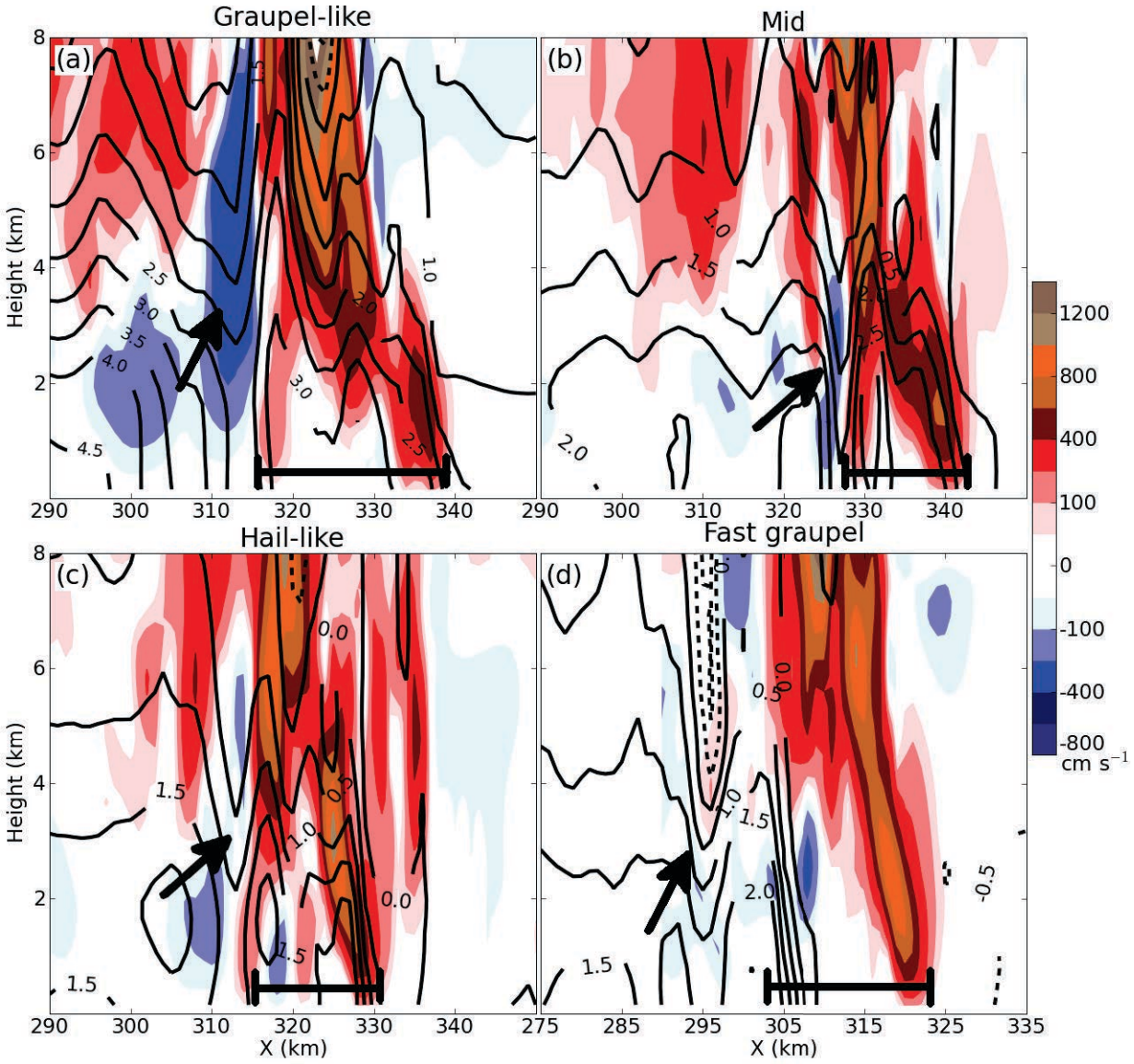

Figure 5.6: Vertical motion (color, cm s^{-1}) and relative perturbation pressure (black, 0.5 hPa, negative dashed). Perturbation pressure was calculated by subtracting the mean total domain pressure profile from the total pressure field. These cross-sections are a 60-km subset of the cross-sections shown in Fig. 5.4. The black arrows in each figure point to the low pressure perturbation discussed in the text. The brackets show the total tilt of the convective updraft over heights from 0 to 6 km.

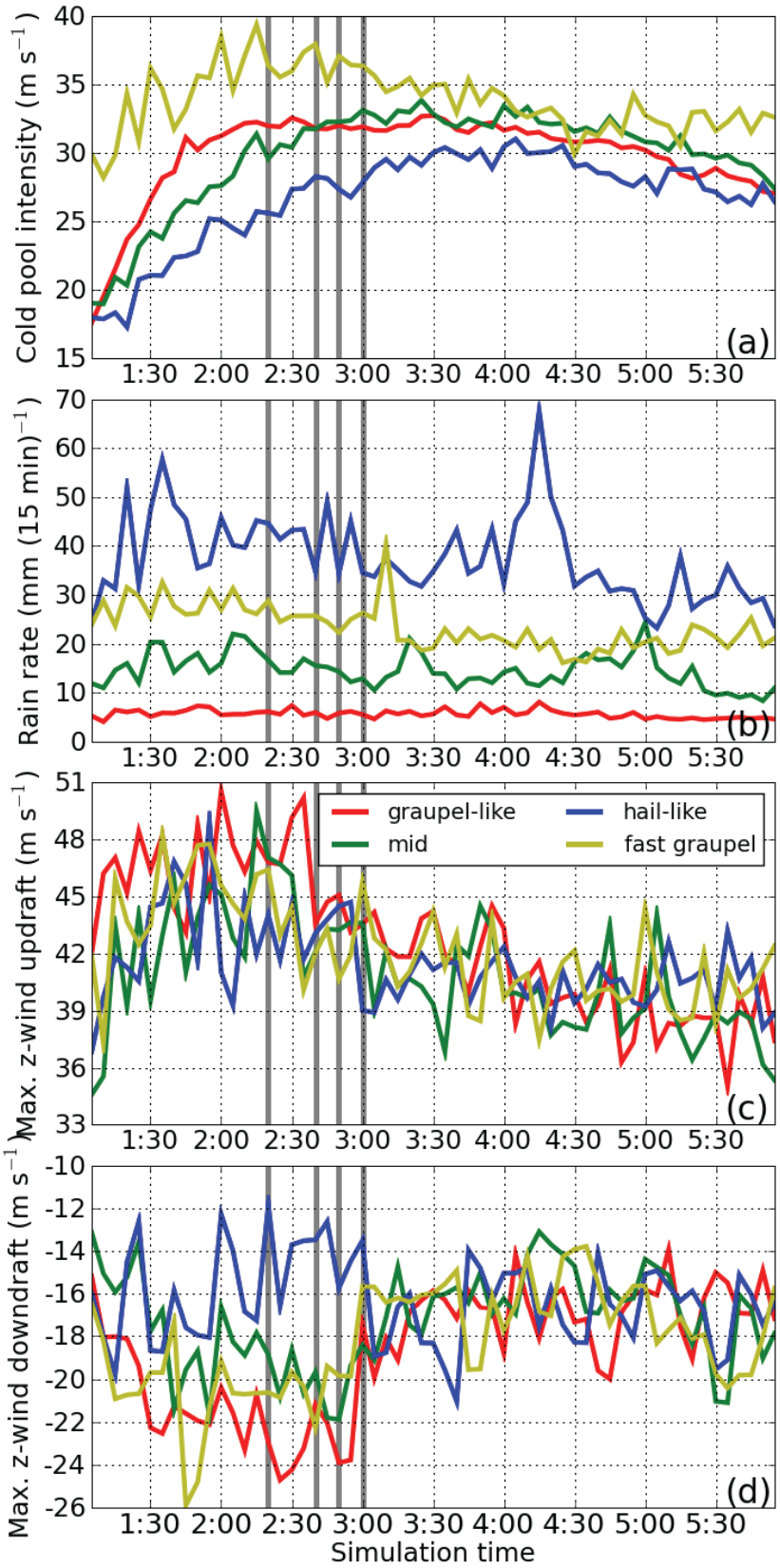

Figure 5.7: *Caption on following page.*

Figure 5.7: *From previous page*: comparison of "graupel–like" (red), "mid" (green), "hail-like" (blue), and "fast graupel" (yellow) simulations from 1 to 6 h simulation time within the convective line. (a) maximum C (m s^{-1}), (b) maximum rain rate (mm (15 min)$^{-1}$), (c) maximum z-wind updraft (m s^{-1}), and (d) maximum z-wind downdraft (m s^{-1}). Maximum and minimum values are calculated over the entire 5-minute timestep. The four thick grey lines are the times new bowing development initiates in the "fast graupel", "graupel-like", "mid", and "hail-like" simulations (2:20, 2:40, 2:50, and 3:00 respectively).

to melting and evaporation, both minimum and domain-averaged values, are given in Table 2. The "graupel-like" system contained smaller graupel hydrometeors that were advected rearward, which formed the extensive convective line and stratiform precipitation regions evident in Fig. 5.4a. The cold pool associated with the "graupel-like" system was widest (Fig. 5.4a), and significantly more intense than the "hail-like" cold pool, as measured by cold pool intensity, C (Fig. 5.7a). C is calculated as in Bryan and Morrison (2012), $C^2 = \int_0^h B\, dz$, where B is given by (3.1) and h is the height at which B becomes 0.

The slower-falling, small graupel hydrometeors resulted in high melting and evaporation rates (Fig. 5.5a, Table 2) almost 40 km behind the convective line. The deepest portion of the cold pool was actually in the stratiform region, co-located with the largest melting and evaporation rates. Because of this strong and deep cold pool, this system contained large mid-level buoyancy and pressure perturbations (Fig. 5.6a). Note that the pressure perturbations are relative, calculated with respect to the domain mean pressure field at the time, so perturbations only need to be lesser than their surroundings to be considered "low", not absolutely negative.

The hail in the "hail-like" system fell almost immediately out of the updraft due to its much larger size (Fig. 5.4c), and was able to reach the surface before much melting occurred. Small amounts of cooling by melting and evaporation are evident in Fig. 5.5c, and associated cooling rates are small (Table 2). The peak magnitudes of cooling were located less than 10 km rearward of the system updraft. Cloud ice content was also much higher in the upper levels of the storm, consistent with other studies noting transfer of mass to smaller frozen hydrometeor classes in simulations with hail (Milbrandt and Morrison 2011). The cold pool

associated with this system at this time was of weaker intensity (Fig. 5.7a) and lesser depth. This would correspond well with the slower system noted earlier, as well as weaker mid-level buoyancy and pressure gradients (Fig. 5.6c).

The "fast graupel" system produced the most intense cold pool (Fig. 5.7a), but it was very narrow. (Initial cold pool intensity values for all simulations were 18.4 m s^{-1}). Little condensate remained aloft as its graupel hydrometeors fell quickly out of the updraft once formed (Fig. 5.4d). Because the mean size of these hydrometeors was quite small, the increased surface area-to-volume ratio still allowed a significant amount of melting and subsequent evaporation to occur (Fig. 5.5d), but it was concentrated in an area immediately behind the convective line. This is evident in Table 2 as the peak magnitude of cooling by melting of the "fast graupel" system is the lowest of all the simulations, but the domain mean less so. The mid-level pressure gradient was most intense compared to the other systems' (Fig. 5.6d). This indicates the mean size of the graupel hydrometeor is important as well as its fallspeed when determining cooling rates.

5.2.3 Microphysical effects on bowing

Prior to bowing, the convective updrafts of all four simulations were similar in intensity (Fig. 5.7c) and minimally tilted. The updrafts in the "graupel-like" system were slightly stronger, due largely to increased freezing rates (not shown, likely from increased concentrations of smaller hydrometeors). The updrafts in the "mid" and "hail-like" systems were slightly weaker, but still minimally tilted.

As bowing occurred, however, each system's convective updrafts became additionally tilted (Fig. 5.6), as would be expected. The updraft of the "fast graupel" and "graupel-like" systems, with their most intense cold pool and surface-based rear-to-front flow (Figs. 5.7a, 5.3a, d), tilted farther rearward first, and therefore also bowed first. At the time of bowing, the tilt of the convective updraft between 0 to 6 km aloft was approximately 20-25 km in these two systems. The tilt of the "graupel-like" system was larger than the "fast graupel"

system, possibly because of the larger magnitude of the rear-to-front flow further adding to the negative vorticity associated with the cold pool. However, both tilts were large enough to initiate bowing. The updraft of the "hail-like" system, with its weaker cold pool and more elevated rear-to-front flow (Figs. 5.7a, 5.3c), increased its updraft tilt later and therefore bowed last as well. Also evident was an increase in the maximum downdraft velocity associated with each system immediately prior to bowing (Fig. 5.7d).

By 4:00, just over an hour after all four systems had bowed, the convective updraft in the "graupel-like" simulation had appeared to separate into two updrafts, one at lower levels from 0-3 km, and the other at mid- and upper levels, from 3-9 km (not shown). The lower-level updraft was approximately 20 km ahead of the upper-level one. The convective updraft in the "mid" and "hail-like" systems were each somewhat less tilted: the "mid" system over approximately 15 km, and the "hail-like" system over about 10 km. By 5:15, because of the extreme updraft tilt, the updraft associated with "graupel-like" system was slightly weaker than the "mid" system, and weaker yet than the most upright "hail-like" system (Fig. 5.7c). The cold pools associated with each were growing correspondingly weaker as well (Fig. 5.7a). Surprisingly, the "fast graupel" system updraft strength remained similar to the less tilted "hail-like" updraft throughout; possibly the result of a more narrow cold pool and slower rear-to-front flow (not shown).

The increased evaporation rates of the "graupel-like" system resulted in its domain-maximum precipitation rates being smallest; because so much of the hail in the "hail-like" system reached the surface without even melting, its maximum precipitation rates were the highest (Fig. 5.7b). Additionally, many of the "graupel-like" system's frozen hydrometeors were still aloft throughout the simulation due to their slower fallspeeds. In the "fast graupel" simulation these hydrometeors were able to reach the surface, producing large maximum precipitation rates. Peak precipitation rate was more sensitive to hydrometeor fallspeed than mean size. Total precipitation accumulation was as well; the mean total gridpoint accumulation of liquid and frozen precipitation in the "fast graupel" and "graupel-like" simulations

(7.88 and 7.90 mm) were less than the "mid" mean total (8.39 mm) and significantly less than the "hail-like" mean total (10.83 mm).

5.2.4 Comparison to other studies

Because the WSM6 scheme is also single-moment with respect to rain drops, increased evaporation was expected in the stratiform rain region as the fixed hydrometeor intercept would keep the concentration of rain drops artificially high compared to the varying concentrations in a double-moment scheme, as discussed in Bryan and Morrison (2012). However, the extreme evaporation rates seen in that study's single-moment Morrison simulation, to the point of the stratiform precipitation region not reaching the surface, were not seen in any of these simulations. The graupel fallspeed parameters in the Morrison scheme, at the mixing ratio values typically seen in the stratiform region (on the order of 1 g kg^{-1}), result in slightly slower fallspeeds (Fig. 5.1b). These slower fallspeeds would allow increased melting and evaporation rates. Additionally, the fixed rain intercept parameter in the WSM5/6 schemes is 8×10^6, slightly lower than the 10^7 value specified in the single-moment Morrison scheme used in that study, meaning the overestimation of concentration in the stratiform region should not be quite as severe. These factors combined could have lessened the evaporation rates in this study.

The result of the "graupel-like" system creating a more intense cold pool than the "hail-like" system is in contrast to Gilmore et al. (2004a), van Weverberg et al. (2011a, 2012), and Milbrandt and Morrison (2011) which found the hail system created more intense cold pools. In general, in those studies the fast hail fallspeeds increased the downward precipitation flux, which increased the melting and evaporation rates. The graupel hydrometeors with their relatively slow fallspeeds remained aloft in those systems. Large amounts of graupel were certainly falling below the melting level in this "graupel-like" simulation (Fig. 5.4a). Additionally, many of the "hail-like" hydrometeors were still frozen upon reaching the surface (Fig. 5.4c), unlike in those other studies, reducing the opportunity for latent cooling.

One possible reason for this difference lies in the initial environment. The environmental soundings used in the simulations of Gilmore et al. (2004a), van Weverberg et al. (2011a), and Milbrandt and Morrison (2011) had lower CAPE values compared to this study; 2200, 1000, and 2200 J kg^{-1}, respectively, compared to an initial CAPE of 3752 J kg^{-1}. Those same studies also had significantly higher deep-layer shear values, as all three studies were simulating supercells: 0-5 km shear of 30 and 50 m s^{-1}, 0-6 km shear of 28 m s^{-1}, and 0-7 km shear of 40 m s^{-1}, respectively, compared to the 0-5 km shear in this study of 14.2 m s^{-1}, almost all of which is in the 0-2.5 km layer. Meanwhile, the colder "graupel-like" cold pool results of this study agree with van den Heever and Cotton (2004) and Bryan and Morrison (2012), both of which simulated convection in environments with higher CAPE (3130 J kg^{-1} and 4200 J kg^{-1}) and weaker shear (0-5 km shear of approximately 20 m s^{-1}, and 0.5 - 10 km shear of 10 m s^{-1}). Changes in CAPE and shear would affect both updraft strength and storm structure, possibly modifying the time spent aloft by hail/graupel hydrometeors and affecting the resulting microphysical cooling rates. For example, van Weverberg et al. (2011b) found a positive correlation between peak updraft strength and the increase in rain rate due to "hail-like" graupel modifications.

In the context of bow echoes, an increase in shear would change the cold pool-environmental shear vorticity balance, increasing the amount of cooling required to overwhelm that balance and possibly delaying bowing. Thus, the sensitivities of the microphysical variations described herein to changes in the environment, specifically an increase in 0-5 km shear, should be tested. However, within this environment of weaker low-level shear changing the graupel parameter to take on more hail-like characteristics acted to diminish both the microphysical cooling and warming within the system. This occurred as a result of both the increased mean size and the increased mean fallspeed. In turn, the strength and depth of the cold pool and mid-level buoyancy gradient was decreased, and weakened the mid-level pressure perturbation. The rear-to-front flow associated with the system was not as fast,

and did not descend to the surface until almost reaching the convective line. Hence, the convective updraft was slower to tilt upshear and bowing did not develop as quickly.

5.3 Results from removal of graupel class

The WRF Single-Moment 5-class and 6-class microphysics schemes are identical except for the inclusion of graupel as a class in the 6-class scheme (Lim and Hong 2010). Simulations using both the 5- and 6-class schemes ("no-graupel" and "graupel" simulations, see Table 1) were run to examine the importance of graupel as a class. These comparisons will continue to explore the effect of changes in microphysical cooling rates on bowing initiation, as well as the effect slowly falling frozen hydrometeors have on cold pool strength.

The "no-graupel" simulation quickly developed a large stratiform shield ahead of the convective line as early at 1:10 (not shown) due to large concentrations of small and slowly falling snow being advected ahead of the updraft; the convective line itself was intense but narrow compared to the "graupel" simulation. The "graupel" simulation did not develop a trailing stratiform shield until approximately 2:00 (not shown), but the convective line was thick and intense. The "graupel" system also propagated at a significantly faster speed than the "no-graupel" system; a discussion of the reason for this will follow.

At 2:35, a small segment on the north end of the "graupel" system began to bow (Fig. 5.8a), which had developed a small but intense stratiform region. The "no-graupel" simulation at this time had not bowed, and still contained an extensive amount of leading stratiform precipitation (Fig. 5.8d). At 3:10, the "no-graupel" simulation's stratiform region had increased in size, and a small segment on its northern end began to bow (Fig. 5.8e). The "graupel" simulation continued to bow (Fig. 5.8b). Neither system dissipated before simulation end (Figs. 5.8c,f).

Figures 5.9, 5.10, and 5.11 show hydrometeor profile, microphysical cooling rate, and storm-relative line-normal wind cross-sections from these two simulations; Table 2 again contains the melting and evaporation cooling rates. Figures a and b in each are from 2:35,

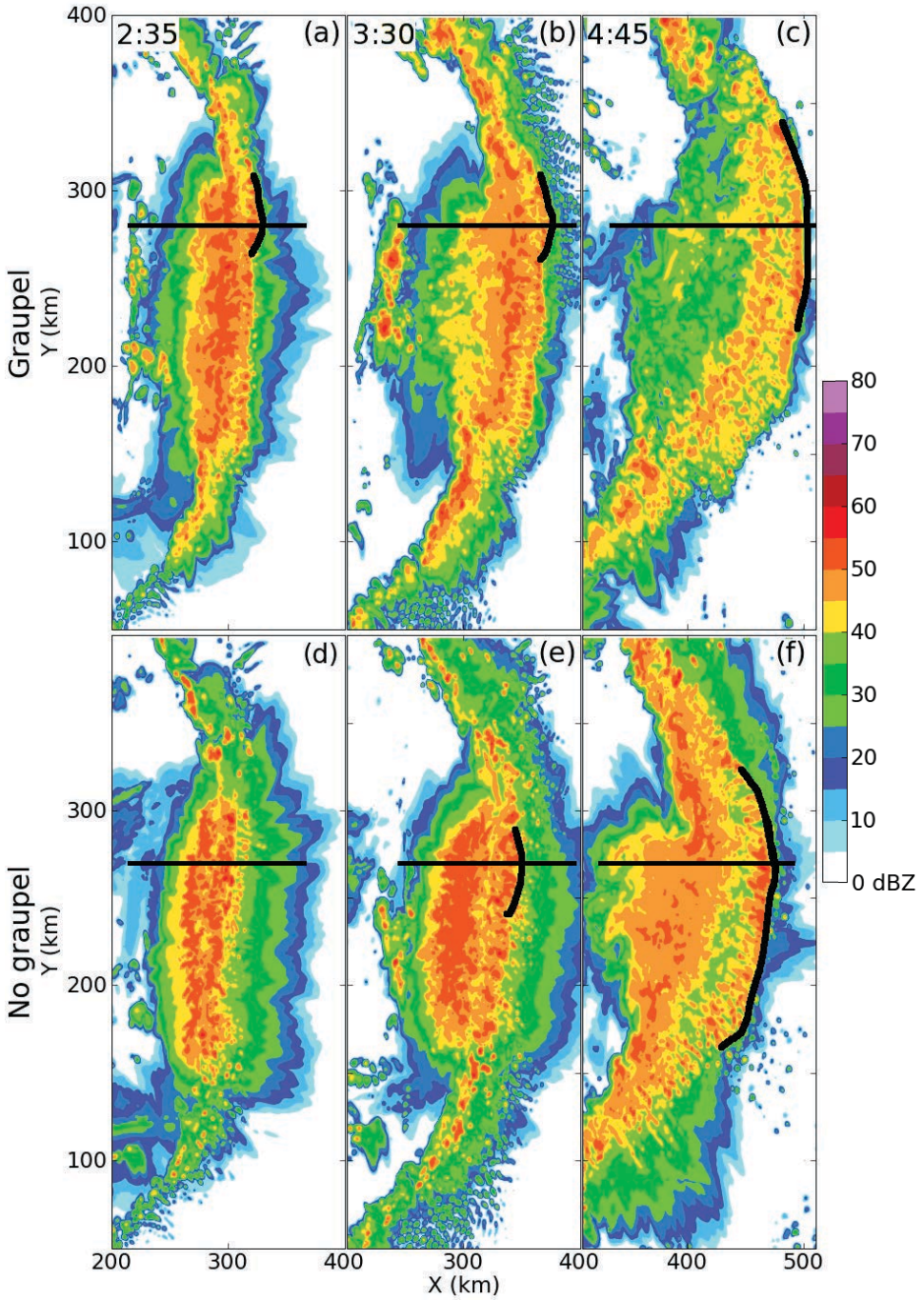

Figure 5.8: Simulated composite reflectivity from the "graupel" (a,b,c) and "no graupel" (d,e,f) simulations. Columns, from left to right, correspond to times 2:35 (a, d), 3:10 (b, e), and 4:45 (c, f). Simulated reflectivity calculated as in Fig. 5.2. Thin black lines delineate location of cross-sections in subsequent figures. Thick black lines show development of bowing segment.

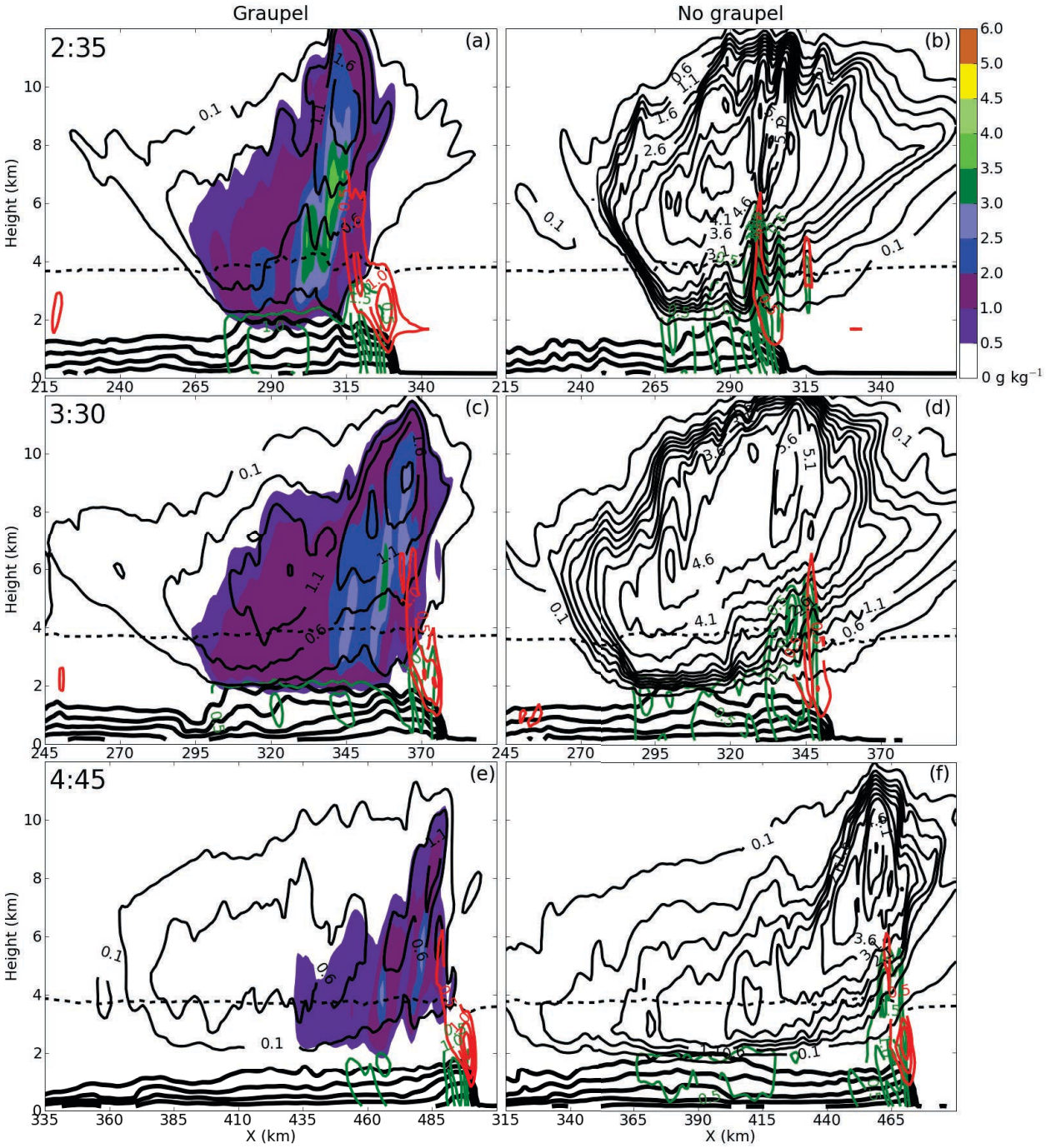

Figure 5.9: Mixing ratio cross-sections from the "graupel" (left column) and "no-graupel" (right column) simulations, at 2:35 (a, b), 3:30 (c, d), and 4:45 (e, f) from cross-section lines shown in Fig. 5.8. Contour values identical to Fig. 5.4. No color in (b), (d), and (f) as they lack graupel.

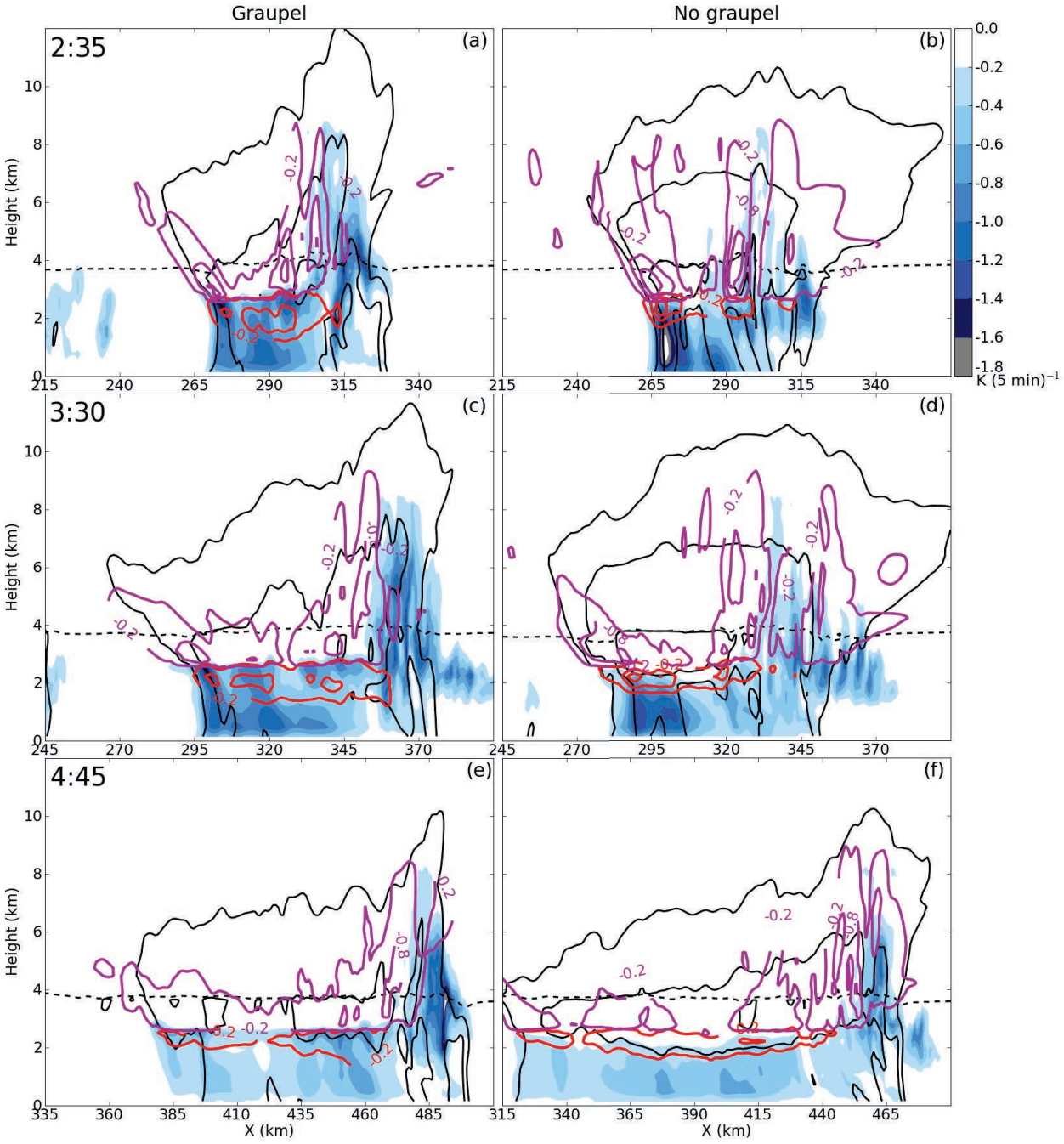

Figure 5.10: Microphysical cooling cross-sections from the "graupel" (left column) and "no-graupel" (right column) simulations, at 2:35 h (a, d), 3:10 h (b, e), and 4:45 (c, f) from cross-section lines shown in Fig. 5.8. Contour values identical to Fig. 5.5.

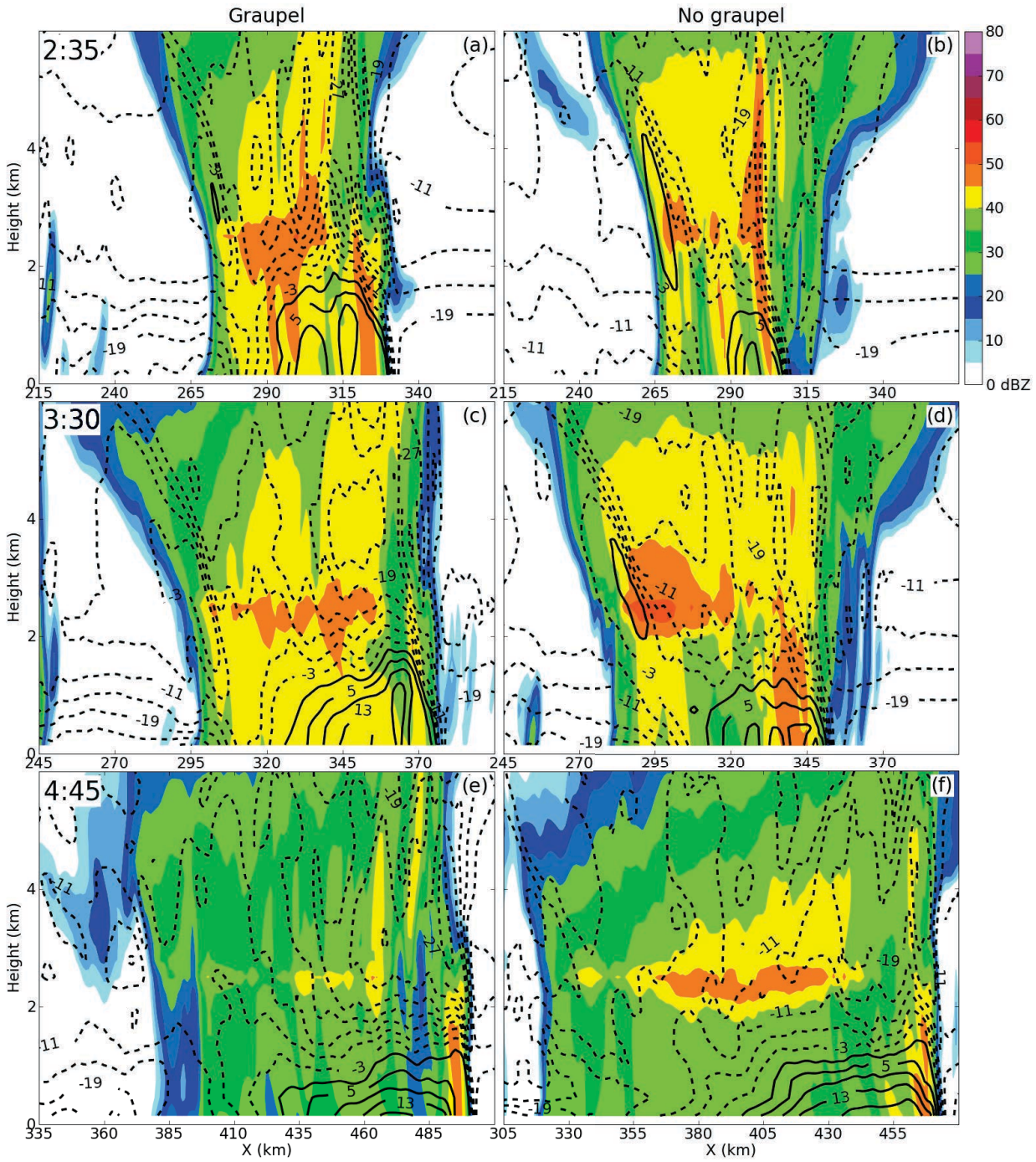

Figure 5.11: Storm relative wind vertical cross-sections from the "graupel" (left column) and "no-graupel" (right column) simulations, at 2:35 (a, b), 3:30 (c, d), and 4:45 (e, f) from cross-section lines shown in Fig. 5.8. Contour values identical to Fig. 5.3.

when the "graupel" system began bowing. The large leading stratiform shield of snow in the "no graupel" simulation is evident in Fig. 5.9b. The main rainshaft was only about 40 km wide and located almost immediately behind the convective updraft; hence, melting and evaporation rates were concentrated in the same location (Fig. 5.10b), and the cold pool was narrow (Fig. 5.9b). It was also less intense than the "graupel" system's cold pool (Fig. 5.13a); this was because much of the snow still remained aloft. Meanwhile, the larger, somewhat less easily advected graupel hydrometeors formed a 55 km wide trailing stratiform region in the "graupel" system (Fig. 5.9a).

At this point, when the "graupel" system was just starting to bow, strong, surface-based rear-to-front flow was evident (Fig. 5.11a). The low-level convective updraft was stronger in the "graupel" system (Figs. 5.12a,b), as were the convective downdrafts which had just intensified immediately prior to this new bowing (Figs. 5.13b,c). There was a strong mid-level low pressure region resulting from the intense cold pool (Fig. 5.13a), located directly behind the convective line (Fig. 5.12a). Thus, the stronger, tilted convective updraft and surface-based rear-to-front flow acted in concert to precipitate earlier new bowing development.

In contrast, the "no graupel" convective updraft remained more upright, tilted only about 10 km between 0 and 6 km, in comparison to the "graupel-like" system's 25 km. Due to slower onset of latent cooling, the "no graupel" system had a less intense cold pool (Fig. 5.13a), slower and still elevated rear-to-front flow (Fig. 5.11b), and weaker convective downdrafts (Fig. 5.13c). The convective updrafts were also weaker (Fig. 5.13b). Hence, the "no graupel" system was not bowing at this time. The low pressure region associated with weaker cold pool was less intense (Fig. 5.12b).

The convective updraft of the "no graupel" system was weaker than that of the "graupel" system initially (Fig. 5.13b), despite being more upright (Figs. 5.12a,b). This is in contrast to Parker (2010), which found a more tilted updraft should be weaker due to downward acceleration from an increased perturbation pressure gradient. However, freezing rates in the updraft were higher in the "graupel" system than in the "no graupel" system (not shown).

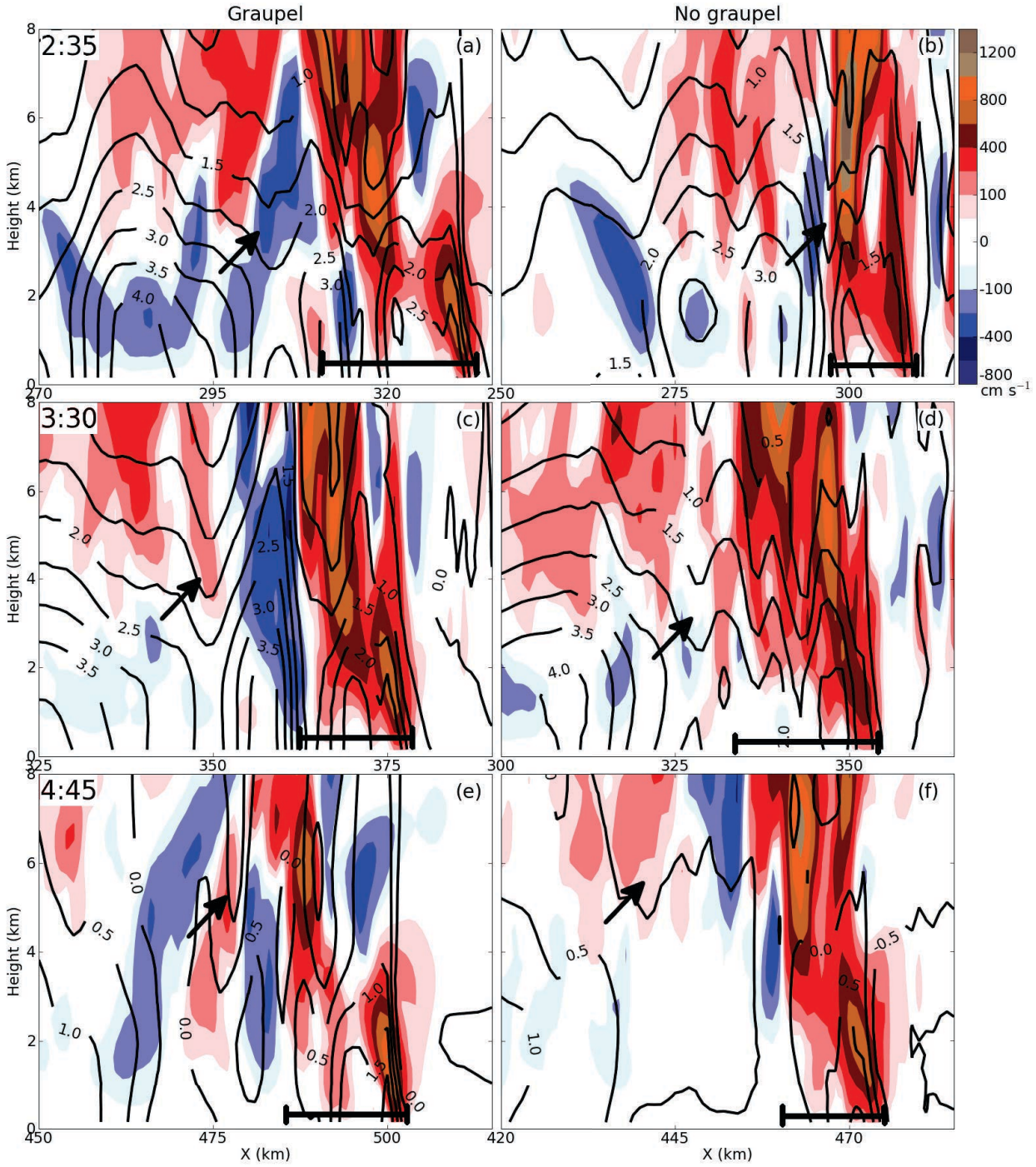

Figure 5.12: Vertical motion and relative pressure perturbation cross-sections from the "graupel" (left column) and "no-graupel" (right column) case study simulation, at 2:35 (a, d), 3:10 (b, e), and 4:45 (c, f). Perturbation pressure was calculated by subtracting the mean domain pressure profile from the total pressure field. Contour values, arrows, an brackets identical to Fig. 5.6. These cross-sections are a 65-km subset of the cross-sections shown in Fig. 5.9.

.

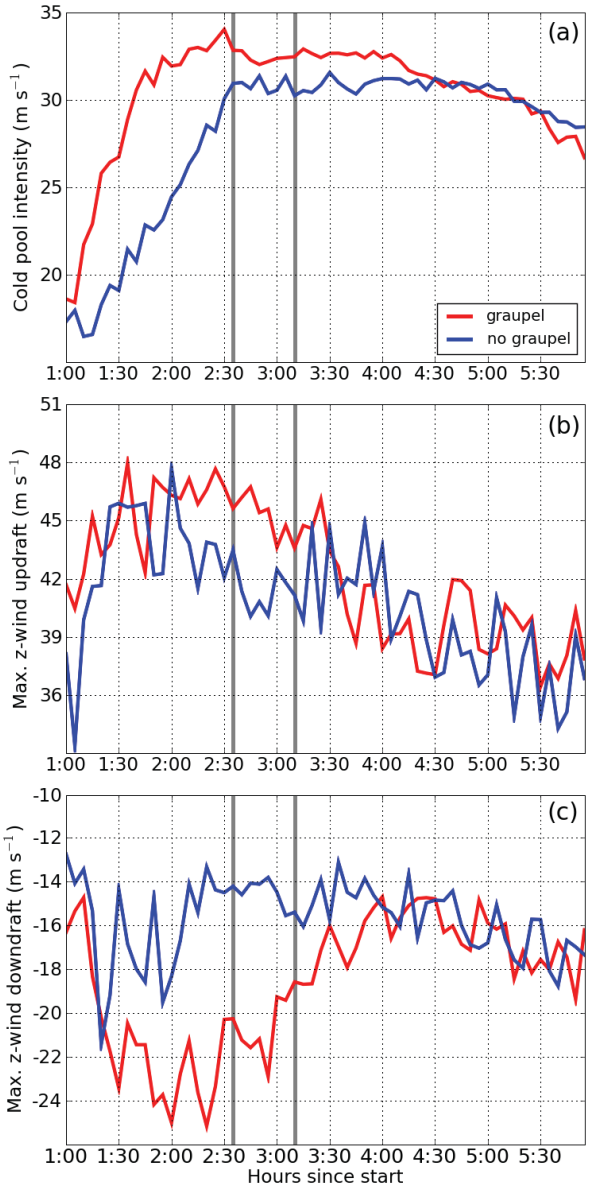

Figure 5.13: Comparison of "no-graupel" (blue) and "graupel" (red) simulations from 1 to 6 h simulation time within the convective line. (a) maximum cold pool intensity (C, m s^{-1}), (b) maximum z-wind updraft (m s^{-1}), and (c) maximum z-wind downdraft (m s^{-1}). Maximum and minimum values are calculated at 5-minute intervals. The two thick grey lines are the times new bowing development initiates in the "no graupel" and "graupel" simulations (2:35 and 3:30, respectively).

This would seem to be counter-intuitive, but the graupel hydrometeors fell relatively quickly. The population of supercooled cloud water was located mainly just above the melting level, in both simulations (Fig. 5.9a,b). As the graupel hydrometeors fell through this population, cloud water accretion rates were large, increasing the freezing rates. Small liquid drops shed from melting graupel hydrometeors were also advected into the updraft by rear-to-front flow, and further increased the freezing rates upon refreezing. This "recirculation" process was similar to that examined by Seigel and van den Heever (2012). Meanwhile, significant amounts of the snow in the "no graupel" simulation did not fall through the supercooled cloud water until later in the simulation, delaying the addition of freezing by accretion to the overall freezing rates. With reduced freezing rates, the "no graupel" updrafts were weaker.

At 3:10, the "no graupel" simulation began to bow. The snow in the stratiform region in the "no-graupel" simulation had been melting, and then evaporating, over a large region rearward of the convective line for quite some time (Fig. 5.10d, Fig. 5.9d). The peak evaporation rate was similar to those of the "graupel" simulation when it began to bow, although the melting rates were not quite as strong (Table 2). The cold pool, while still not quite as large or intense as that of the "graupel" simulation (Fig. 5.9c, Fig. 5.13a), was stronger and wider than previously, with a stronger associated mid-level low pressure region (Fig. 5.12d). The rear-to-front flow had strengthened and descended to the surface farther behind the convective line (Fig. 5.11d). The convective updraft was tilted more rearward over the cold pool than previously, approximately 25 km (Fig. 5.12d), and was about to intensify (Fig. 5.13b). The convective downdrafts had also strengthened (Fig. 5.13c). As such, it is not surprising that the "no graupel" simulation began to bow.

The graupel hydrometeors falling from the large stratiform region in the "graupel" system (Fig. 5.9c) were still producing intense melting and evaporation rates some distance behind the convective line (Fig. 5.10c); however these rates were slightly less than those produced by the more numerous, more slowly falling snow crystals in the "no graupel" simulation. The low pressure perturbation associated with the "graupel" system had shifted farther rearward

of the convective line (Fig. 5.12c) The convective updraft was still tilted over approximately 20 km, but it remained strong (Fig. 5.13b).

By 4:45, the size of the "graupel" system convective updraft had diminished (Fig. 5.12e), although peak values remained steady (Fig. 5.13b). Concentrations of graupel aloft in the stratiform region were much lower as they continued to fall out of the stratiform updraft (Fig. 5.9e) The resulting melting and evaporation rates were lower (Fig. 5.10e) and the cold pool intensity had lessened (Fig. 5.13a). Also evident was a weaker low pressure region, still approximately 25 km behind the convective line(Fig. 5.12e). The rear-to-front flow had descended to the surface even farther rearward of the convective line (Fig. 5.11e), the convective updraft was strongly tilted, and the system was weakening (Fig. 5.13b,c).

The "no graupel" system still had large amounts of snow aloft (Fig. 5.9f). While a portion of the snow had fallen out, a significant amount remained, resulting in still-intense melting and evaporation rates throughout the entire wide system below the melting level (Fig. 5.10f). The cold pool of the "no graupel" system was more intense than the graupel system's through the end of the simulation, although convective updraft and downdraft maxima of the two simulations were roughly steady through this period (Figs. 5.13a,b,c).

In summary, the "no-graupel" simulation cold pool transitioned from relatively warmer to cooler as the slower-falling snow finally began to melt; the system itself became more organized with stronger rear-to-front flow and bowing development as the simulation progressed. Meanwhile the "graupel" simulation cold pool was intense from shortly after initialization, due to the large cooling rates produced by melting graupel and evaporating rain spread throughout the lower levels. However, the cooling rates lessened as the faster-falling graupel fell out of the storm; the strongly tilted updraft was unable to transport enough condensate aloft in replacement. Therefore, the "graupel" system began to weaken more quickly than the "no graupel" simulation, as measured by total condensate aloft and cold pool intensity.

5.4 Summary

Changing the graupel parameter within a WRF microphysics scheme to take on more hail-like characteristics acted to diminish both the microphysical cooling and warming within the bow echo system. This occurred as a result of both the increased mean size and the increased mean fallspeed. In turn, the strength and depth of the system cold pool and mid-level buoyancy gradient was decreased, which weakened the mid-level pressure perturbation. As a result, the rear-to-front flow associated with the system was not as fast, and did not descend to the surface until almost reaching the convective line. Hence, the convective updraft was slower to tilt upshear and bowing did not develop as quickly.

A sensitivity test with graupel entirely removed was also simulated. The "no-graupel" simulation cold pool transitioned from relatively warmer to cooler as the slower-falling snow finally began to melt; the system itself became more organized with stronger rear-to-front flow and bowing development as the simulation progressed. Meanwhile the "graupel" simulation cold pool was very intense from shortly after initialization, due to the large cooling rates produced by melting graupel and evaporating rain spread throughout the lower levels. As a result, the system developed bowing before the "no graupel" system. However, the cooling rates lessened as the faster-falling graupel fell out of the storm; the strongly tilted updraft was unable to transport enough condensate aloft in replacement. Therefore, the "graupel" system began to weaken more quickly than the "no graupel" simulation, as measured by total condensate aloft and cold pool intensity.

The strong sensitivity of these idealized simulations to changes in the graupel parameterization suggest case study simulations should see equally large variations. Ideally, these variations could be compared to observations to determine if the features produced are realistic. Such large variations in model-forecasted fields would also have important operational implications. The next chapter is devoted to these topics.

CHAPTER 6
QUANTITATIVE EVALUATION OF BOW ECHO MICROPHYSICAL SENSITIVITY

The goal of this chapter is to quantify the variability, of five different forecasting parameters related to new bowing development, that can be expected from changes to the microphysics scheme – specifically, to the graupel parameter. The five parameters are timing of new bowing, maximum 10-m wind gust speed, system propagation speed, convective and stratiform areal coverage, and total accumulated precipitation. The graupel parameter was chosen because of its large effects already noted in previous studies on microphysical cooling rates, as discussed in Chapter 2. In order to achieve these goals, a variety of microphysics schemes and parameter settings within the Weather Research and Forecasting (WRF) model were used to simulate a case study of the 13 March 2003 bow echo, with comparison to observations to aid in the quantification.

Section 6.1 describes the experiment and model design, as well as the specific microphysics variations. A review of the case study being simulated is presented in Section 6.2. Section 6.3 discusses the sensitivity of the five operational parameters to microphysical changes, and Section 6.4 the conclusions.

6.1 Methodology

6.1.1 Model setup

The Advanced Research Weather Research and Forecasting (WRF-ARW) model, version 3.2.1 (Skamarock et al. 2008), was used in this study to simulate an isolated bow echo case over Oklahoma on 13 March 2003. This model was chosen as its ability to simulate case studies of mesoscale phenomena is well-known. It is widely used in operational forecasting (High Resolution Rapid Refresh model, Alexander et al. 2011; National Centers for Environ-

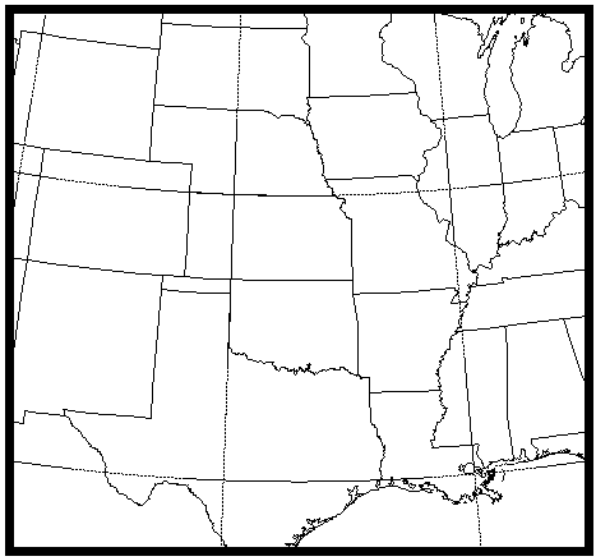

Figure 6.1: WRF-ARW domain. The entire domain was run in 3-km resolution. Later figures will show only a subsection of the domain over eastern Oklahoma for space considerations.

mental Prediction (NCEP) Short Range Ensemble Forecast (SREF) System, Du et al. 2009), and its design easily allows microphysics modifications. This specific case was selected as it initiated and dissipated entirely within the confines of the Oklahoma Mesonet, allowing use of that dataset to better observe the system. Additionally, Adams-Selin and Johnson (2010) analyzed in detail surface observations of this system as it initiated bowing.

The initial and lateral boundary conditions for this simulation were provided by the NCEP Final Operational Global (FNL-GFS) Analysis data, at 1^o by 1^o horizontal and six-hour temporal resolution. The NCEP Eta analysis and the North American Regional Reanalysis datasets were also used, but the FNL-GFS data produced results closest to observations. The model was initialized at 1200 UTC on 12 March 2003, and run for 36 hours to 0000 UTC 14 March 2003. A horizontal grid spacing of 3 km was used; the domain is shown in Fig. 6.1. This resolution was selected as it is typical of current operational model resolutions (Kain et al. 2008). Model differences created by changes in microphysics schemes will vary at different resolutions (Bryan and Morrison 2012); thus to inform the forecaster of expected differences a typical operational resolution should be used.

The 35 vertical levels were stretched, with increasing resolution in the lower levels. Pa-

rameterization schemes other than microphysics include the Mellor-Yamada-Janjic boundary layer scheme (Janjic 1994), the Noah land surface model (Ek et al. 2003), Rapid Radiative Transfer Model longwave radiation scheme (Mlawer et al. 1997), and the Goddard shortwave radiation scheme (Tao et al. 2003). No convective parameterization was used, as typically grid-spacing of 4 km or lower is considered convective-resolving (Weisman et al. 1997). Positive-definite moisture transport was selected to avoid the positive precipitation bias associated with non-positive-definite schemes (Skamarock and Weisman 2009). This combination, in addition to the set of microphysics schemes, was chosen after considerable experimentation as it produced the most realistic convective systems when compared to observations. Additionally, this configuration is very similar to that currently used by the High Resolution Rapid Refresh (HRRR) model (Alexander et al. 2011; only difference is use of the 6-layer land surface model instead of the Noah), the U. S. Air Force Weather Agency's WRF model (http://www.meted.ucar.edu/nwp/pcu2; only difference is use of the Yonsei University boundary layer scheme), and the National Severe Storms Lab experimental high resolution WRF (use of Dudhia shortwave radiation instead of Goddard, http://www.nssl.noaa.gov/wrf).

6.1.2 Microphysics and experiment design

Sensitivity tests were conducted using eight microphysics schemes available within WRF: Kessler (Kessler 1969), Ferrier (Ferrier et al. 2001), WRF Single-Moment 5-class (WSM5; Hong et al. 2004), WRF Double-Moment 5-class (WDM5; Lim and Hong 2010), Lin (Lin et al. 1983), WRF Single-Moment 6-class (WSM6; Hong and Lim 2006), WRF Double-Moment 6-class (WDM6; Lim and Hong 2010), and Morrison (Morrison et al. 2009). These specific schemes were chosen because they include a wide range of predicted frozen hydrometeor classes and highly diverse graupel distribution characteristics, particularly in terms of the distribution intercept parameter, slope, hydrometeor density, and fallspeed.

Variations in the graupel distribution intercept and slope change the mean hydrometeor

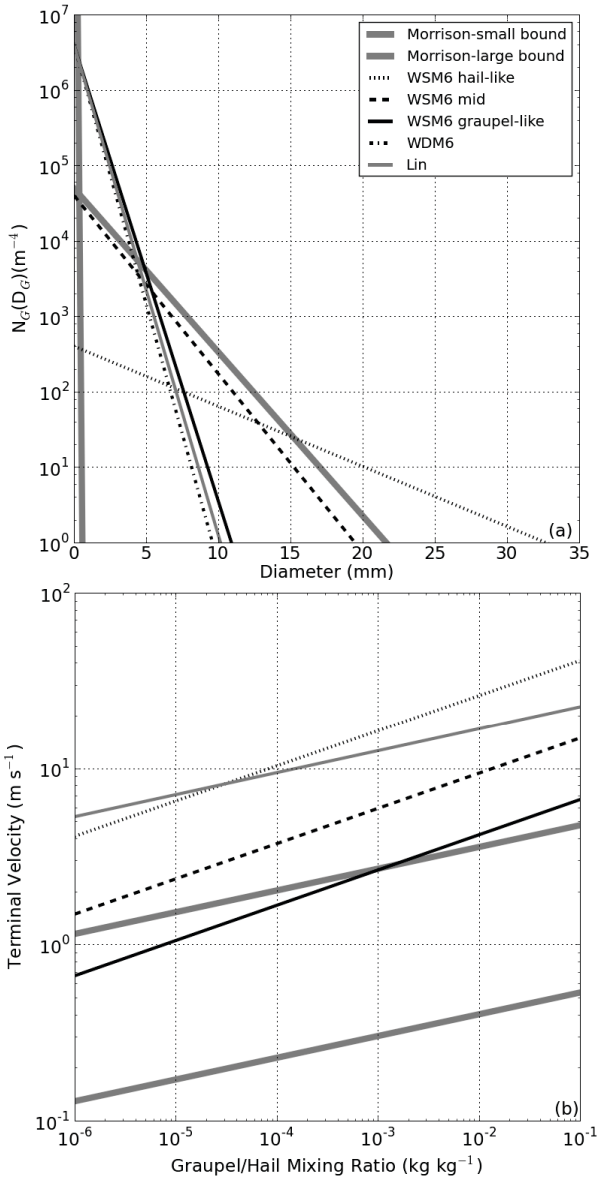

Figure 6.2: (a) Graupel hydrometeor distributions for the microphysics schemes examined that have a graupel class. This assumes a graupel mixing ratio of 1 g kg^{-1} and air density of 1 kg m^{-3}. Within the Morrison scheme, bounds are placed on the distribution slope; the largest and smallest values allowed are shown here. (b) Mass-weighted mean graupel hydrometeor terminal velocity (m s^{-1}) for a range of graupel mixing ratios (kg kg^{-1}). The WDM6 mean terminal velocity is very similar to the WSM6 "graupel-like" modification. The two Morrison terminal velocity functions represent the two bounds on the graupel distribution function, shown above. Temperature is fixed at 268.15 K, and pressure at 900 hPa. Calculations for "graupel-like", "mid", and "hail-like" are as in Chapter 5.

size; larger hydrometeors have a smaller surface area-to-volume ratio, which will decrease melting and evaporation rates (van den Heever and Cotton 2004; Cohen and McCaul 2006). Changes in hydrometeor density and fallspeed both affect the speed at which the graupel hydrometeors leave the system. Larger, denser, and hence faster falling particles increase the downward precipitation flux (Gilmore et al. 2004a) but also allow less time for melting and evaporation. Cooling rates are correspondingly decreased as these hydrometeors fall below the melting level (van den Heever and Cotton 2004; Cohen and McCaul 2006). The combined effect of these two modifications (surface area-to-volume ratio and fallspeed) on cooling will hereafter be referred to as the "mean size effect". Removal of the graupel class or even all frozen classes altogether also significantly modifies the microphysical structure of the storm, by transferring mass into other hydrometeor classes that have different characteristics.

A full description of each of the schemes, its number of classes, and graupel intercept parameter, slope, density, and fallspeed is provided in Table 6.1. The various graupel hydrometeor distributions and fallspeeds for each scheme with a graupel class are shown in Figs. 6.2a and b, respectively. The Kessler scheme has no frozen hydrometeor classes, and is the least complex scheme used. The Morrison scheme is the most complex, and has four double-moment classes where both hydrometeor mixing ratio and total number concentration are prognostic variables. The WDM5 and WDM6 schemes include cloud condensation nuclei (CCN) as a prognostic variable, allowing CCN concentration to be depleted and replenished in interaction with cloud droplets.

Within the Morrison scheme the choice can be made to switch the sixth class from graupel to hail; here it was left as graupel. Bryan and Morrison (2012) have already examined the effect of switching this parameter in simulations of idealized squall lines. They found that simulations with a graupel class developed a wider convective line with weaker reflectivities; the hail simulation convective line was narrower with stronger reflectivities. As the Morrison graupel class is double-moment, the slope and intercept of its distribution can vary, but

Table 6.1: Characteristics of the twelve unique microphysics configurations used in this chapter. Within the classes column, *cw*, *ci*, *rw*, *sn*, *gr* represent cloud water, cloud ice, rain water, snow, and graupel, respectively. ρ is environmental air density (kg m^{-3}); ρ_{850} the density of the standard atmosphere at 850 hPa (kg m^{-3}); q_G graupel mixing ratio (kg kg^{-1}); and N_G total concentration (m^{-3}). Mixing ratio is a prognostic value for all classes; total concentration is the second prognostic value for all double-moment classes.

Microphysics scheme	Classes	Double-Moment classes	Graupel size distribution (m^{-4}; $n_G(D_G)$)	Graupel slope (λ_G)	Graupel density (ρ_G; kg m^{-3})	Graupel intercept (n_{0G})	Graupel fallspeed (m s^{-1}; v_G)
WSM6	*cw*,*ci*,*rw*,*sn*,*gr*	none	$n_{0G}exp(-\lambda_G D_G)$	$\lambda_G = \left(\frac{\pi \rho_G n_{0G}}{\rho q_G}\right)^{1/4}$	500	4×10^6	$v_G = \frac{a_G}{6}\left(\frac{\rho_{850}}{\rho}\right)^{0.54}\frac{\Gamma(4+b_G)}{\lambda_G^{b_G}}$
"hail-like"					900	4×10^2	a_G=330, b_G=0.8
"mid"					700	4×10^4	a_G=285, b_G=0.8
"graupel-like"					300	4×10^6	a_G=270, b_G=0.8
Kessler	*cw*,*rw*	none	—	—	—	—	—
Ferrier	*cw*,*rw*,*sn*	none	—	—	—	—	—
WSM5	*cw*,*ci*,*rw*,*sn*	none	—	—	—	—	—
WDM5	*cw*,*ci*,*rw*,*sn*	*cw*,*rw*	—	—	—	—	—
Lin	*cw*,*ci*,*rw*,*sn*,*gr*	none	$n_{0G}exp(-\lambda_G D_G)$	$\lambda_G = \left(\frac{\pi \rho_G n_{0G}}{\rho q_G}\right)^{1/4}$	400	4×10^6	$v_G = \frac{a_G}{6}\left(\frac{\rho_G}{\rho}\right)^{0.5}\frac{\Gamma(4+b_G)}{\lambda_G^{b_G}}$ a_G=4.67, b_G=0.5
WDM6	*cw*,*ci*,*rw*,*sn*,*gr*	*cw*,*rw*	$n_{0G}exp(-\lambda_G D_G)$	$\lambda_G = \left(\frac{\pi \rho_G n_{0G}}{\rho q_G}\right)^{1/4}$	500	4×10^6	$v_G = \frac{a_G}{6}\left(\frac{\rho_{850}}{\rho}\right)^{0.54}\frac{\Gamma(4+b_G)}{\lambda_G^{b_G}}$ a_G=330, b_G=0.8
Morrison	*cw*,*ci*,*rw*,*sn*,*gr*	*rw*,*ci*,*sn*,*gr*	$n_{0G}exp(-\lambda_G D_G)$	$\lambda_G = \left(\frac{\pi \rho_G N_G}{\rho q_G}\right)^{1/3}$ bounds: 5×10^2 and 5×10^4	400	variable; affected by slope bounds	$v_G = \frac{a_G}{6}\left(\frac{\rho_{850}}{\rho}\right)^{0.54}\frac{\Gamma(4+b_G)}{\lambda_G^{b_G}}$ a_G=19.3, b_G=0.37

within two bounds (Table 6.1; Morrison et al. 2009). The distributions and fallspeeds of the large and small bounds are both displayed in Figs. 6.2a and b.

Additional graupel sensitivity tests were conducted by varying the graupel distribution characteristics within the WRF Single Moment 6-class scheme (WSM6) as in the previous chapter. In that study, the graupel intercept, fallspeed, and density parameters were varied to make the mean graupel hydrometeor larger, denser, faster-falling, and more "hail-like"; smaller, lighter, slower-falling, and more "graupel-like"; or between the two or "mid". The parameter values used in that study were also used here and are detailed in Table 6.1. This study will further elucidate the effects that can be expected from these variations, particularly within operational contexts.

6.1.3 Convective/stratiform area determination

The simulated radar reflectivity algorithm from Stoelinga (2005) was used for reflectivity calculations, but was modified to utilize the default snow and graupel intercept and density parameters in the WSM/WDM6 schemes. The same reflectivity algorithm was used for all simulations. The goal of this study was not to evaluate simulated radar reflectivity algorithms, but instead to compare the effects microphysics scheme modifications had on the resulting reflectivity values. Using different algorithms would allow microphysics changes to "hide" behind different reflectivity algorithms. On a more practical level, customized reflectivity algorithms were not available at the time of the study for all the microphysics schemes tested; as these are now available within WRF version 3.4.1, further study is suggested.

Composite radar reflectivity was computed by selecting the maximum reflectivity value anywhere in the column. A threshold of 40 dBZ was selected for division of composite radar reflectivity returns into stratiform (between 15 and 40 dBZ, inclusive) or convective (greater than 40 dBZ) as in Steiner et al. (1995). (The full convective/stratiform division algorithm given in Steiner et al. (1995) was tested in this case, but the results incorrectly classified some of the stratiform region as convective, unlike the simple threshold method.)

The lower threshold of 15 dBZ was selected to filter out clutter returns in the observational data. While this devision is not exact, it will still allow for comparison between the observed and simulated values.

For model-simulated data, one gridpoint has an area of 9 km^2. For observed radar data, KTLX WSR-88D long-range composite radar reflectivity was downloaded from the National Climatic Data Center (NCDC). The National Oceanic and Atmospheric Administration (NOAA) Weather and Climate Toolkit was utilized to import the data and regrid it to approximately 100-m resolution using nearest-neighbor interpolation. Following this, nearest-neighbor interpolation was used again to reproject the data onto a grid of 3 km horizontal resolution. This method of interpretation was selected after multiple trials as it produced the gridded results closest in appearance to observations. The number of observed and simulated convective and stratiform gridpoints could now be directly compared.

6.2 Case review

Fifteen-minute resolution WSI NOWrad mosaic base reflectivity data was obtained from the National Center for Atmospheric Research's (NCAR) Mesoscale and Microscale Meteorology Division (MMM) archive at http://www.mmm.ucar.edu/imagearchive/WSI. A description of WSI NOWrad data can be found at
http://www.mmm.ucar.edu/imagearchive/WSI/docs/NOWradDescriptionWSICorp.txt.
Oklahoma Mesonet data, available every 5 minutes from over 110 stations across Oklahoma, were utilized to examine all other atmospheric fields.

Initiation of convection first occurred in north-central Oklahoma at 0215 UTC (not shown) within a southwest to northeast-oriented pressure trough and co-located thermal ridge (Adams-Selin and Johnson 2010). A similarly-aligned convective line approximately 250 km in length formed by 0315 UTC (Fig. 6.3a). The system moved to the southeast at a speed of approximately 11 m s^{-1}. A trailing stratiform precipitation region appeared at 0500 UTC (Fig. 6.3b), and began to develop rearward. At 0600 UTC (Fig. 6.3c) the center of

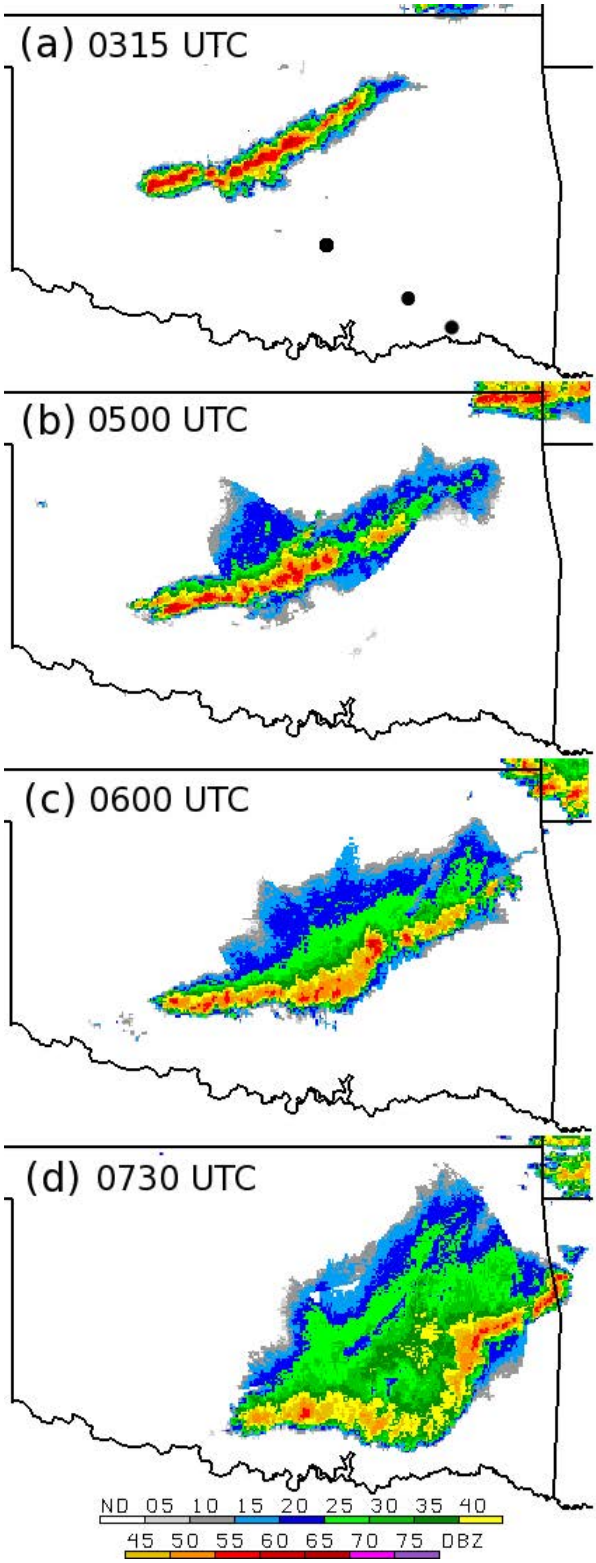

Figure 6.3: 0315 UTC (a), 0500 UTC (b), 0600 UTC (c), and 0730 (d) 13 March 2003 WSI NOWrad composite radar reflectivity data. Oklahoma Mesonet stations VANO, LANE, and HUGO are displayed from northwest to southeast, respectively, as black dots in (a).

the convective line bowed out and its speed increased to approximately 18 m s^{-1}; stratiform precipitation filled in behind the line as it bowed. Strong 10-m wind gusts, some as high as 20 m s^{-1}, developed at this point in association with the bowing convective line.

A secondary reflectivity maximum formed in the stratiform region at 0700 UTC, separated from the convective line by a transition zone. The bow echo continued to increase in size until 0730 UTC (Fig. 6.3d), at which point it started to dissipate. The cold pool and gust front associated with the decaying convective line and stratiform precipitation continued to propagate southeastward over the next four hours. The precipitation eventually reformed into another mesoscale convective system in Louisiana.

6.3 Results from sensitivity tests

All the simulations initialized a single convective cell over south-central Oklahoma, approximately 100 minutes later and 250 km southwest of the actual, linear, convective initiation (not shown). The location, type, and timing of initiated convection is largely a function of the dataset used to provide the initial conditions and the planetary boundary layer parameterization and only indirectly a function of the microphysics scheme. Thus, this study will focus on the characteristics of the simulated convection after its initiation.

All simulations eventually produced a bow echo over southwestern Oklahoma (Fig. 6.4), making it clear that ice microphysics are not required to successfully simulate a bow echo, as also shown in Weisman (1993). However, the simulations differ in significant details that have important forecasting implications. The convection produced in northeast Oklahoma corresponds to but is somewhat displaced from observed convection in central Arkansas, and will not be discussed.

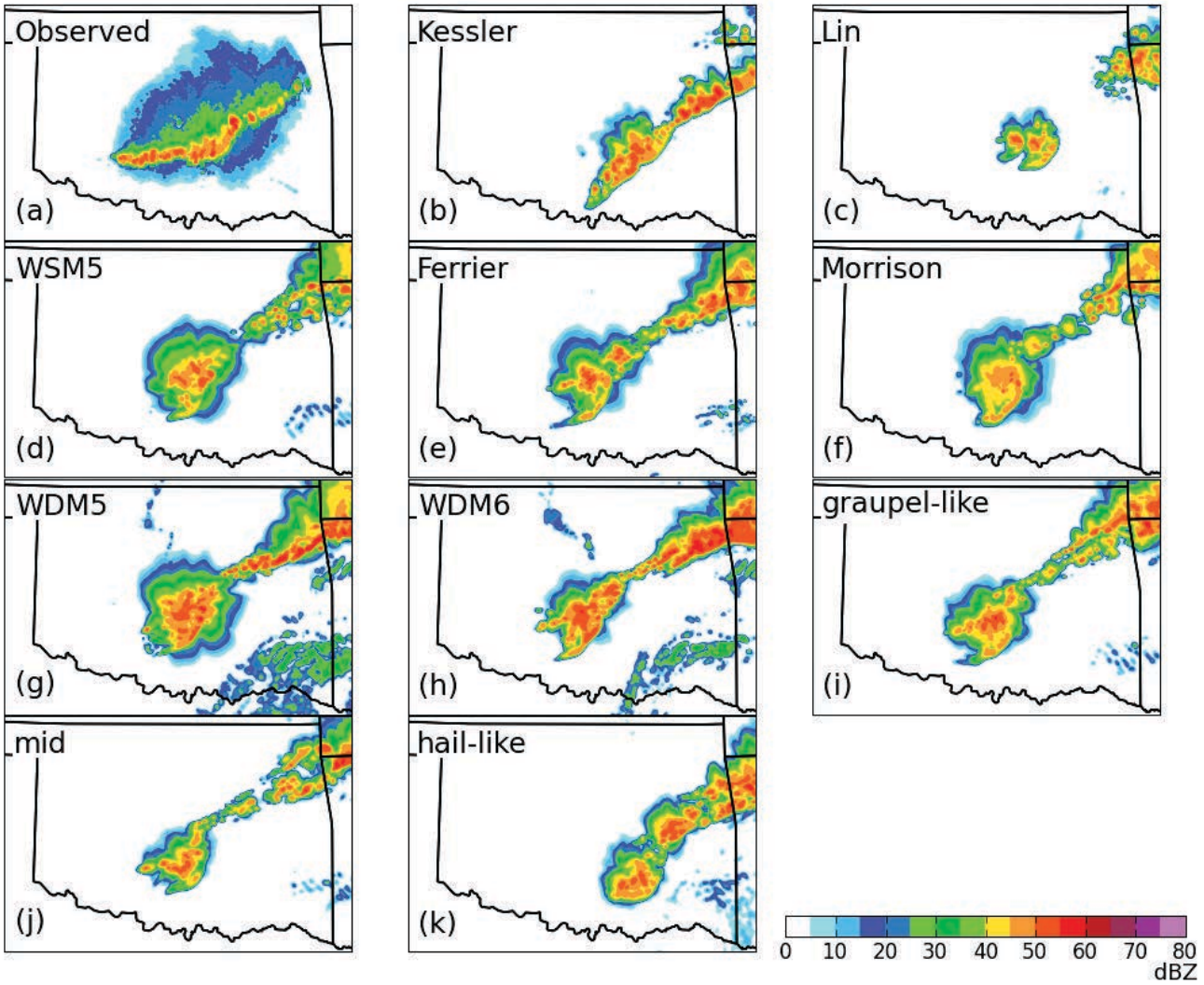

Figure 6.4: Composite reflectivity, from the KTLX radar (a) and model-simulated (b-k) at the time of bowing initiation of each system (see Table 3 for times of bowing initiation).

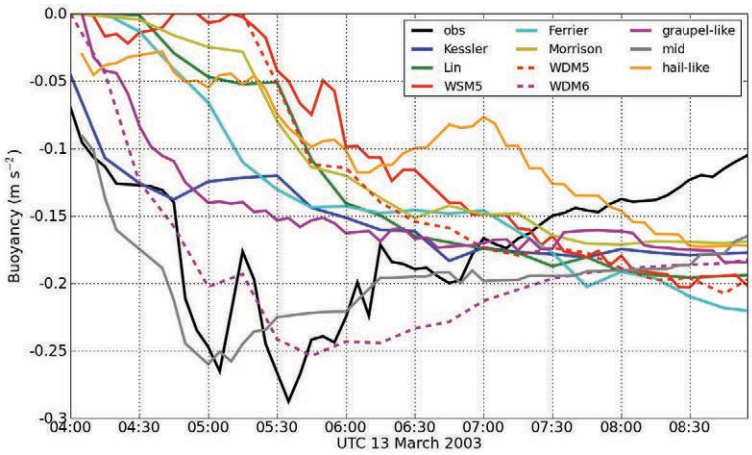

Figure 6.5: Minimum surface buoyancy (m s^{-2}) of the cold pool associated with the simulated and observed (using the Oklahoma Mesonet) convective systems.

Five specific phenomena associated with this convective system that have operational impact will be examined: time of bowing initiation, maximum 10-m wind gust speed, system speed, the respective areas of the convective and stratiform regions, and precipitation accumulation. These will be discussed individually in the following subsections for all sensitivity test simulations.

The strength of the cold pool associated with each convective system is of importance to all five of these phenomena. Minimum surface buoyancy within the convective cold pool of the observed and simulated convection is shown in Fig. 6.5 and will be discussed throughout the section. Buoyancy was calculated using

$$B = g\left(\frac{\theta - \overline{\theta}}{\overline{\theta}} + 0.61(q_v - \overline{q_v})\right) \tag{6.1}$$

where g is gravitational acceleration, θ potential temperature, q_v water vapor mixing ratio, and the bars designate environmental conditions. Values were measured at 1.5 m above ground in the Oklahoma Mesonet and 2 m in the model. Precipitation loading due to liquid and frozen hydrometeors was not included as those measurements were not available from the Oklahoma Mesonet. Observed environmental values were an average of measurements at stations TAHL, WEST, PRYO, and JAYX in extreme eastern Oklahoma. Simulated

environmental conditions were mean values calculated over a 225 km^2 box in far north-central Texas; a different location was required due to the extraneous convection in northeast Oklahoma produced in each simulation.

6.3.1 Bowing initiation

Table 6.2 displays the time of bowing initiation in each simulation, and the actual time bowing developed. These times were determined subjectively by evaluating when the radius of curvature of the convective line began decreasing with time (as defined by Klimowski et al. 2000). The simulated reflectivity at time of bowing initiation in each simulation is shown in Fig. 6.4. The majority of the simulations initiated bowing after the actual system; this fits with the simulated convection initiating later than the observed convection.

Table 6.2: Time bowing initiates; UTC 13 March 2003.

Simulation	Time
WSM6	
"graupel-like"	0545
"mid"	0545
"hail-like"	0730
Kessler	0600
Ferrier	0615
WSM5	0620
WDM5	0615
Lin	0715
WDM6	0545
Morrison	0630
observed	0555

The systems in the "graupel-like" and "mid" WSM6 configurations, and the WDM6 simulation, began bowing first at 0545 UTC. These configurations have smaller, more numerous "graupel-like" hydrometeors, hence via the graupel mean size effect should also result in increased microphysical cooling, and a deeper, more negatively buoyant cold pool. The cold pool buoyancy can be seen in Fig. 6.5: the "mid", "graupel-like", and WDM6 cold pools all developed quickly and by 0545 UTC, the time of bowing in each, had become quite cold.

The Kessler system, whose cold pool also quickly cooled, bowed comparatively early as well, about 15 min later.

The "mid" system reached a buoyancy minimum the earliest of all the simulations, even faster than the WDM6 and "graupel-like" systems (Fig. 6.5). The faster fallspeed of the "mid" graupel hydrometeors allowed them to fall below the melting level first, and subsequently melt and evaporate. Once the smaller "graupel-like" hydrometeors fell in larger numbers below the melting level later in the simulation, the mean size effect ensured a more negatively buoyant cold pool, particularly in the WDM6 simulation. The difference in buoyancy observed between the WDM6 and "graupel-like" simulations will be discussed further in the next two sections.

From the previous chapter, the increased mobility and rearward advection of these smaller graupel particles would both shift the peak microphysical cooling rearward and strengthen it, thereby also aiding the descent of the rear-to-front system flow to the surface farther behind the convective line (Weisman 1992; Yang and Houze 1995; Pandya and Durran 1996). The surface-based flow would help tilt the convective updraft farther rearward earlier and initiate bowing sooner (Weisman 1993).

Meanwhile, the "hail-like" and Lin systems did not bow until over 90 minutes later than the "graupel-like" system, at 0730 and 0715 UTC, respectively. The time period between convective initiation and bowing in the observed system and these simulations was most similar, although the convective line in these simulations contained reflectivities approximately 10 dBZ less than observed (Figs. 6.4a, c, k). From the previous chapter, the large graupel hydrometeors in these simulations would result in reduced evaporation rates through the mean size effect and a weaker cold pool (visible in Fig. 6.5). The decreased mobility and rearward advection of the larger hail particles would ensure the peak cooling, associated downdrafts, and descent of rear-to-front flow to the surface remained closer to the convective updraft. These factors ensured a less tilted convective updraft, delaying bowing.

The Morrison scheme system also bowed comparatively late. Because of the double-

moment nature of its classes, the rain intercept parameter was allowed to decrease in the stratiform region, resulting in decreased concentrations of small raindrops and decreased evaporation rates as well (Morrison et al. 2009). The double-moment graupel class would have the same effect; graupel hydrometeors of large mean size melt to produce larger rain drops and are associated with less evaporation (van Weverberg et al. 2012). Less cooling, evident in Fig. 6.5, would have meant more elevated rear-to-front flow and a more slowly tilting convective updraft, yielding later bowing development.

One notable difference between this study and that of the previous chapter was the interval between the "graupel-like" and "hail-like" simulation bowing initiation times. In that study the interval was approximately 20 minutes; here, the simulations differed by over 90 minutes. The difference between minimum buoyancy values in the "graupel-like" and "hail-like" simulations was approximately 1.1 m s^{-2} in both studies, although in the previous chapter the cold pool of the "graupel-like" system was significantly deeper. It is possible that the convective initiation method used in the idealized simulations in that study aided in simulating a much stronger "hail-like" system than the "hail-like" case study system simulated here. Thus, without a strong initiation mechanism, the role played by microphysics in affecting the timing of new bowing development was even larger.

6.3.2 10-m wind gust speeds

It is known from van den Heever and Cotton (2004) that a decrease in the mean size of the largest frozen hydrometeor in supercell simulations resulted in stronger low-level downdrafts due to the increased microphysical cooling in the same location. As noted in the previous section, variations in microphysical cooling can affect the descent of the rear-to-front flow within the system, and the timing of new bowing development. Thus, it is not unreasonable to expect surface wind gusts to vary as a result of microphysics modifications as well.

Figure 6.6 displays 10-m wind gust speed from the simulations and Oklahoma Mesonet observations 30 minutes after bowing development in each. Thirty minutes after bowing

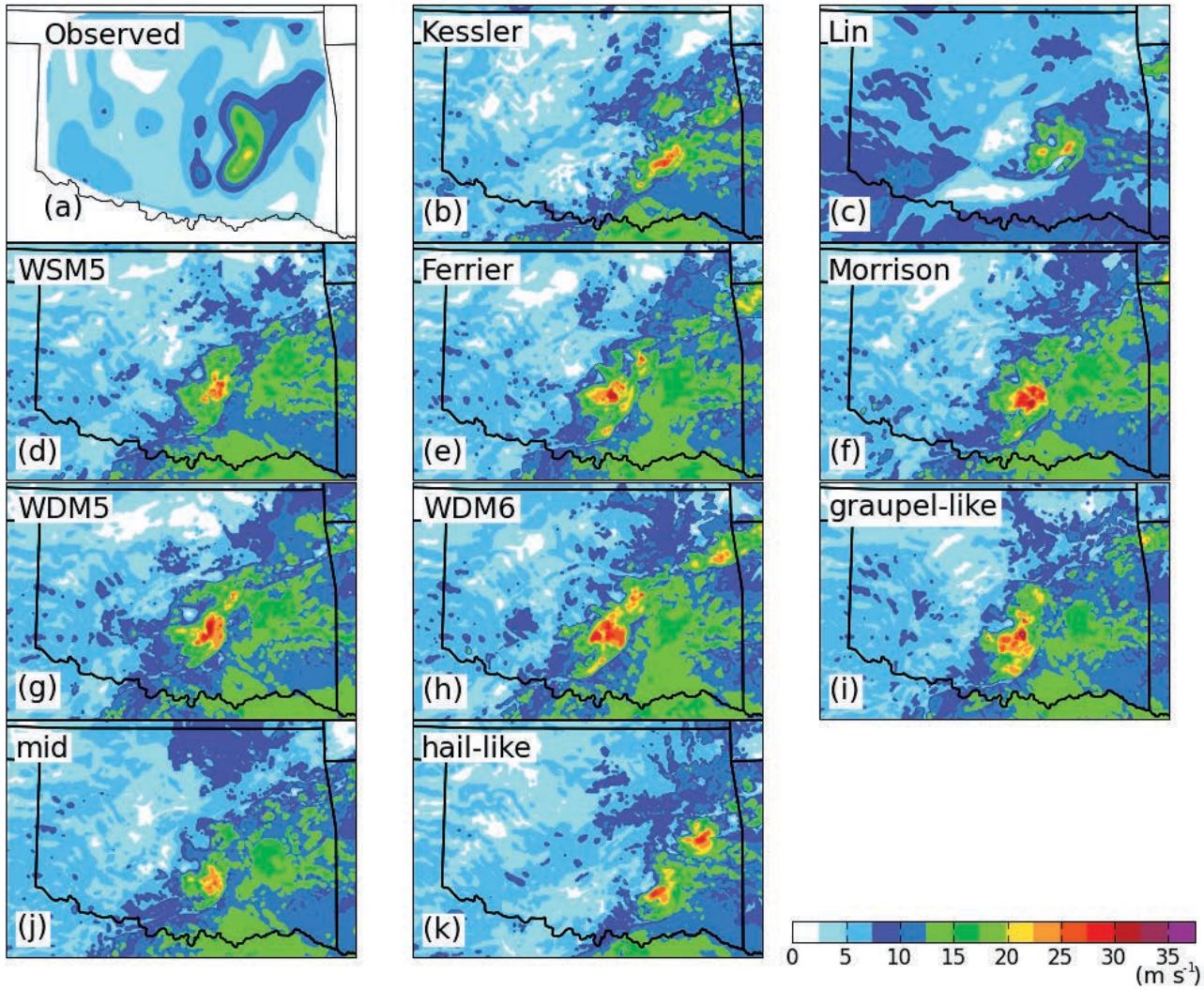

Figure 6.6: 10-m wind gust speed (m s^{-1}), from simulations and observed from Oklahoma Mesonet, 30 min after bowing initiation of each system (see Table 3 for times of bowing initiation). Wind gust speed calculated as in the Unified WRF Post-Processor (UPP).

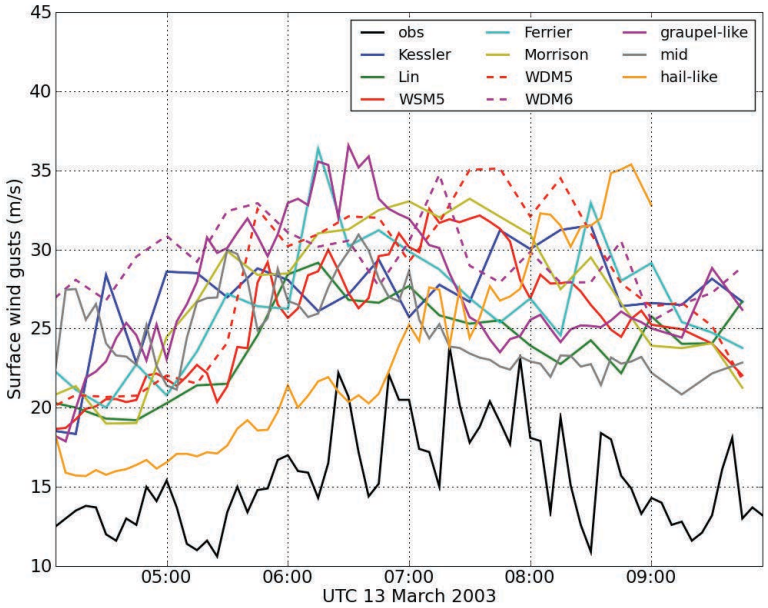

Figure 6.7: Maximum 10-m wind gust within simulated or observed system (using Oklahoma Mesonet). Wind gust speed calculated as in Unified WRF Post-Processor (UPP).

was generally when wind gust speeds were most intense (see Table 2 for times of bowing initiation). Wind gusts were calculated from the model data using the algorithm in the Unified Post Processor (UPP), a commonly-used WRF post-processor. The algorithm mixes momentum downward from the top of the boundary layer. If the boundary layer height is greater than 1 km, the wind gust speed is assumed to be the mean of the 10-m wind speed and the wind speed at the top of the boundary layer. As the boundary layer height decreases, the wind gust speed increases linearly until it is equal to the wind speed at the top of the boundary layer.

Figure 6.7 displays the maximum 10-m wind gust speed associated with each system as measured by the Oklahoma Mesonet or calculated over each simulation model domain. It is obvious from both of these figures that the simulated systems all produced significantly stronger wind gusts than were observed. One possibility is that the observations slightly underestimated the true 10-m wind gust speed because the relatively coarse Mesonet resolution (approximately 30-50 km) was unable to completely sample the highly spatially variant convective winds, compared to the higher resolution of the model (3 km). It is also possible

that either the model or wind gust algorithm was too aggressive, or that the model vertical resolution did not adequately resolve winds at 10 m or the top of the boundary layer, instead interpolating these from a higher level. However, comparison among the simulated values is still instructive.

It is evident that the simulations with a larger mean graupel size or fallspeed (Lin and the "hail-like" WSM6 configurations; Figs. 6.6c, k and 6.7) had weaker wind gusts than those with a smaller mean graupel size or slower fallspeed ("graupel-like" and WDM6; Figs. 6.6i, h and 6.7). These smaller graupel simulations contain systems that from van den Heever and Cotton (2004) would be expected to have stronger low-level downdrafts. Through the increased latent cooling due to the mean size effect, system rear-to-front flow would strengthen (Yang and Houze 1995). The combination of increased system rear-to-front flow and low-level downdrafts appeared to aid intensification of the 10-m wind gusts associated with these simulated systems.

The WDM5, WDM6, and Morrison schemes (Figs. 6.6g, h, f and 6.7) produced the most intense 10-m winds. This was likely due to their double-moment rain distribution. As discussed in Lim and Hong (2010) and Morrison et al. (2009), the double-moment rain distribution allowed the concentration of small rain drops in the convective line to increase, thereby decreasing their mean size. Through the mean size effect, this would result in increased microphysical cooling and faster convective downdrafts. Furthermore, the slower fallspeed of these smaller rain drops would increase amounts of the drops held aloft, resulting in greater condensate loading and increasing the convective downdrafts. This combination could translate to increased 10-m wind gusts through faster downward advection of the momentum of the rear-to-front flow.

At the peak of maturity of the simulated systems, defined as just after the development of a bow echo, simulations with different microphysical schemes produced maximum 10-m wind gust speeds varying from 22 to 35 m s^{-1} (Fig. 6.7), a fluctuation of almost 160%. As the threshold wind gust speed in U. S. National Weather Service severe thunderstorm warning

Table 6.3: Times of arrival of simulated and observed convective line at Oklahoma Mesonet stations VANO and LANE, and system speed between the two. Times are UTC on 13 March 2003.

Simulation	VANO arrival time	LANE arrival time	System speed
WSM6			
"graupel-like"	0540	0700	19.7
"mid"	0545	0710	18.5
"hail-like"	0605	0740	16.5
Kessler	0555	0730	16.5
Ferrier	0615	0745	17.5
WSM5	0620	0750	17.5
WDM5	0620	0740	19.7
Lin	0645	0830	15.0
WDM6	0555	0715	19.7
Morrison	0620	0745	18.5
observed	0545	0709	18.7

criteria is approximately 26 m s^{-1}, this variation has important practical implications. Thus, in addition to the already recognized model factors of initialization environment and boundary layer parameterization that significantly affect system wind gust simulation (Johnson et al. 2011), the choice of model microphysics scheme is not insignificant.

6.3.3 System speed

System speed was determined within the simulations by evaluating the time of arrival of the convective line at Oklahoma Mesonet stations VANO and LANE. These stations are at Vanoss, OK, 34.79°, -96.84°; and Lane, OK, 34.31°, -96.00° (displayed as black dots on Fig. 6.3a). Table 6.3 displays the arrival times of these simulated systems, and the calculated system speed between them. Station VANO was selected as it was approximately the point by which all the simulated systems had organized into linear convection. Station LANE was selected as at that point none of the systems had yet begun to dissipate.

Through gravity current theory, it is known that the propagation speed of a mesoscale convective system depends on the depth and strength of its cold pool (Charba 1974). The more intense the cold pool, the faster the system speed. Because all simulations in this study

were initialized with the same environmental conditions, the difference in system speed can be almost entirely explained by the cold pool. Unfortunately, cold pool depth could not be measured with the Oklahoma Mesonet data, but cold pool buoyancy was available and will be discussed below.

The slowest systems were the "hail-like" WSM6 configuration, Kessler, and Lin simulations (Table 2). The slow speed of the Kessler simulation was unsurprising, as without ice there was no additional cooling by melting or sublimation to add to the strength of the cold pool, matching results found by Nicholls (1987) and Tao and Simpson (1989) for squall lines. In Fig. 6.5, while initially cooling quickly, the Kessler system slowed its cooling after 0445 UTC, resulting in a slow mean system speed. Through the mean size effect, the "hail-like" WSM6 system had reduced microphysical cooling, resulting in a warmer cold pool and slower system speed. The weak convection produced by the Lin microphysics scheme had the same result.

The slower comparative speeds of the WSM5 and Ferrier simulations were at first glance unexpected. Because of the lack of a graupel class in these schemes, much larger concentrations of snow were produced. The small size and slow fallspeed of these hydrometeors should result in large microphysical cooling rates. However, the snow fell so slowly it took some time before significant concentrations fell below the melting level, echoing results in found in the previous chapter. After significant amounts of snow began melting the "no graupel" systems moved faster, but as this occurred late in the system's lifecycle, the overall system speed was still relatively slow. To evaluate this hypothesis, system speed was also calculated from mesonet station LANE to HUGO (34.03^{o}N, 95.54^{o}W; southernmost black dot in Fig. 6.3a); the WSM5 and Ferrier systems had each increased in speed relative to the other systems (not shown). In Fig. 6.5, the WSM5 and WDM5 cold pools were at first relatively warm, but as the simulation progressed they became significantly colder, agreeing with this theory.

The "mid" WSM6 configuration and Morrison systems were in the middle of the distri-

bution and closest to the observed system speed. While the cold pool associated with the "mid" system was very cold (Fig. 6.5), it was also shallow compared to the "graupel-like" system (not shown). Within the double-moment Morrison scheme, the mean graupel size could vary and become quite large, reducing melting and evaporation due to the mean size effect; Fig. 6.5 shows a relatively warmer cold pool. However, because of the bounds placed on the Morrison distribution the mean graupel size could not become as large as that of the "hail-like" distribution, and the cold pool temperature was relatively warmer. Thus, a moderated system speed was expected and observed.

The "graupel-like" WSM6 configuration, WDM5, and WDM6 systems were the fastest of all the simulations. The fast speed and strong cold pool (Fig. 6.5) of the "graupel-like" configuration was expected because of the mean size effect. However, the fast speeds and strong cold pools (Fig. 6.5) of the two double-moment schemes (WDM5 and WDM6) systems were surprising. In Morrison et al. (2009) and Bryan and Morrison (2012), the double-moment schemes used produced slower systems due to lower concentrations of smaller rainwater hydrometeors in the stratiform region, and correspondingly reduced evaporation and melting. However, in those tests, the graupel class was double-moment as well. The graupel class in the WDM6 scheme was still single-moment, and thus the mean graupel size remained small and its fallspeed slow (Fig. 6.2b).

Furthermore, Lim and Hong (2010) compared the WSM6 and WDM6 schemes and found that WDM6 produced overall higher concentrations of rain everywhere in that simulated system, not just the stratiform region. This was due to enhanced snow and graupel melting processes in the WDM5 and WDM6 schemes producing more rain water mass (Lim and Hong 2010). This was also the case here (not shown). The enhanced melting rates, along with increased evaporation rates from the larger concentrations of smaller rain drops, aided in creating a more intense cold pool (Fig. 6.5), and hence faster system speeds. The WSM6 and WDM6 configurations in the 2010 Hazardous Weather Testbed Spring Experiment produced

similarly intense cold pools and faster systems speeds, as measured by south- and eastward displacement of forecast precipitation compared to observations (Clark et al. 2012).

The microphysics changes produced variations in system speed of approximately 30% from slowest to fastest; changes in graupel characteristics within the WSM6 scheme produced a 19% variation. Furthermore, the times of arrival of the systems at the first selected station, before the systems reached maturity, deviated even more than the changes in system speed could account for – up to 90 minutes difference. This would seem to indicate that the microphysics factors were also influential in the early states of the systems' lifetime, while still unorganized.

6.3.4 Convective/stratiform areal coverage

Figure 6.8 displays the observed and simulated areas of convective and stratiform precipitation, calculated as described in Section 2c. Areal coverage from the spurious convection in northeast Oklahoma is not included in this calculation. Unfortunately the equally spurious light precipitation produced in southeastern Oklahoma in the WDM5 and WDM6 simulations (Figs. 6.4g, h), and to a lesser extent in the WSM5, Ferrier, "graupel-like", "mid", and "hail-like" simulations (Figs. 6.4d, e, i, j, k), could not be filtered out. In these simulations, the bow echo intermingled with that precipitation by 0700 UTC, making the stratiform areal coverage due solely to the bow echo difficult to objectively discern. Interestingly, two simulations (Kessler, Morrison; Figs. 6.4b, c) did not produce this precipitation at all, indicating that microphysics scheme changes alone can act to suppress or initiate initial precipitation development in a simulation, as opposed to only modifying its characteristics after development.

This precipitation increases the WDM5 simulation's stratiform areal coverage by as much as 10,000 km^2 after 0530 UTC, and the WDM6 stratiform coverage by as much as 5,000 km^2 throughout Fig. 6.8a. The effect on the other simulations was minimal. Thus, quantified values of the microphysical effects on stratiform areal coverage cannot include these two

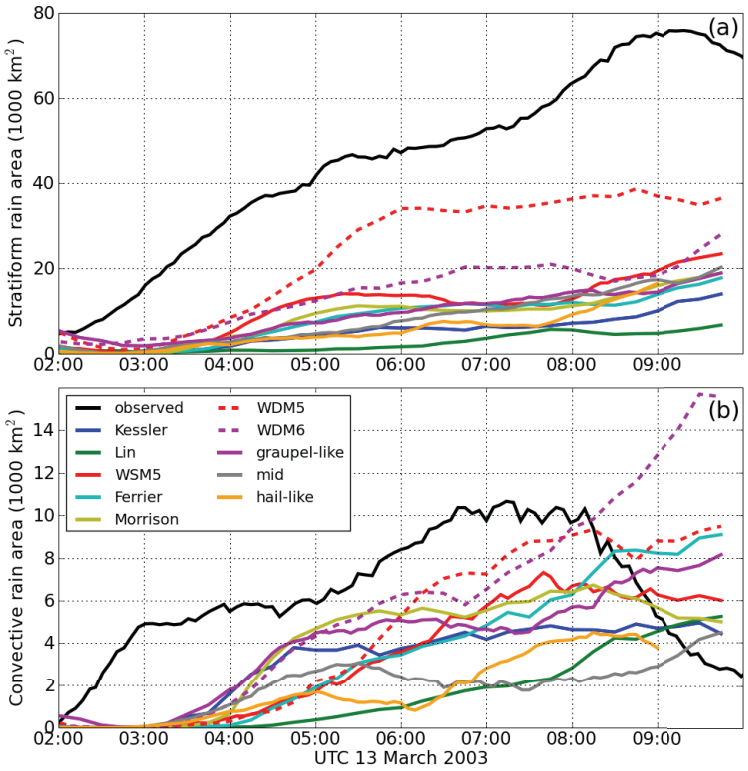

Figure 6.8: Area (in 1000 km^2) of stratiform (a) or convective (b) precipitation, either observed (via KOUN radar) or simulated, over the course of the system's lifecycle. Convective precipitation was assumed to have reflectivity values of 45 dBZ or larger; stratiform precipitation greater than 0 dBZ but less than 45 dBZ. Additional discussion on these calculation is provided in Section 2c.

schemes, but they are still included in Fig. 6.8 for comparison. Convective coverage was not affected.

It is obvious from Figs. 6.4 and 6.8 that all of the simulated systems were both smaller and initiated later than the actual system. This smaller area is partially due to the simulations initiating convection approximately an hour later than was observed, meaning the simulated convection had not had as much time to develop. In addition, the simulated systems originally initiated as an individual cell, and only later organized into the larger, linear systems seen in Fig. 6.4. It is also already known that underestimation of the stratiform-convective region size ratio is a common problem when simulating convection (Luo et al. 2007). However, even noting all these differences, it is still instructive to compare the trends of the observed and simulated precipitation area.

The size of the stratiform region associated with each simulated system largely depends upon the size of the hydrometeors and the strength and positive buoyancy of the front-to-rear flow within the system (Fovell and Ogura 1988; Rotunno et al. 1988, Szeto and Cho 1994; Yang and Houze 1995; Luo et al. 2010). Smaller hydrometeors can be transported more easily by the system airflow, but can also be evaporated or sublimated more easily. A balance must be struck among these processes to produce a large stratiform region. Furthermore, more positively buoyant air in the stratiform region can act to create more hydrometeors, and more easily hold them aloft.

Subjective comparison of the simulated bow echoes (Fig. 6.4) shows that the WDM5 scheme produced the largest stratiform region, although it was still smaller than the observed area. The difference between the stratiform area in the WDM5 and all the other simulations was smaller than Fig. 6.8 would indicate, because of the spurious light precipitation in southeast Oklahoma in the WDM5 and WDM6 simulations, but the difference was still significant. Without a graupel class, large concentrations of snow were produced that were easily transported a great distance from the convective line, creating a very large stratiform shield. Additionally, both of the WDM5 and WDM6 schemes produced larger amounts of rainwater throughout the entire convective system than any other scheme (not shown), further increasing the stratiform shield. Lim and Hong (2010) found a similar result when evaluating effects of adding cloud condensation nuclei (CCN) as a prognostic variable, suggesting a link.

The six other microphysics schemes (WSM5, Ferrier, Morrision, and the three WSM6 configurations) all produced relatively similar stratiform shield sizes, but the Lin and Kessler systems had the smallest stratiform regions. In the Kessler simulation, with no frozen hydrometeors, the raindrops quickly became very large and were not advected large distances from the convective line (similarly observed by Nicholls 1987; Tao and Simpson 1989; and Fovell and Ogura 1988 for squall lines). In addition, with the lack of warming produced in association with freezing and deposition, the system updrafts and overall front-to-rear

flow were not as strong, again resulting in hydrometeors not being advected as far from the convective line (Szeto and Cho 1994).

The Lin system graupel fallspeeds were so fast the hydrometeors were not advected rearward a significant distance. Evaluation of the Lin scheme by Luo et al. (2010) noted that the short graupel residence times yielded decreased condensate loading and therefore a convective updraft that peaked at higher levels aloft. The peak divergence and front-to-rear flow were therefore at higher levels as well: heights containing less ice and less buoyant air, resulting in weaker stratiform updrafts and less deposition aloft.

All of the simulations contained convective areas that were much closer to observed than the stratiform areas were, albeit lagged in time. The WDM5 and WDM6 schemes have the largest convective regions. Lim and Hong (2010) noted similar variations due to increased rainwater amounts. The prognostic CCN in those schemes allowed CCN concentrations, and therefore cloud droplet concentrations, to decrease in the convective line; this resulted in increased autoconversion rates and rainwater amounts. The convective area in the WDM6 scheme in particular was approximately 6,000 km^2 larger than the next largest convective area. This variation was larger than any resulting from graupel characteristics changes, and indicates that the effect of prognostic CCN on convective area size is not insignificant. However, full consideration of CCN effects is beyond the scope of this study.

The Kessler system most quickly developed a convective region; the simulated raindrops were not scavenged by ice crystals and grew in size very quickly . The convective regions in the "hail-like" configuration and Lin systems were slowest to develop - the very fast graupel fallspeeds of these systems resulted in a minimal cold pool and difficulty of the system organizing. The Morrison scheme also had a comparatively small convective region size. Luo et al. (2010) found a similar result due to the increased sublimation and evaporation in the convective region from the increased concentrations of small hydrometeors in all the double-moment classes. The WSM5, WDM5, and Ferrier schemes peaked in convective area later than the other graupel-inclusive schemes, suggesting that the additional cooling by

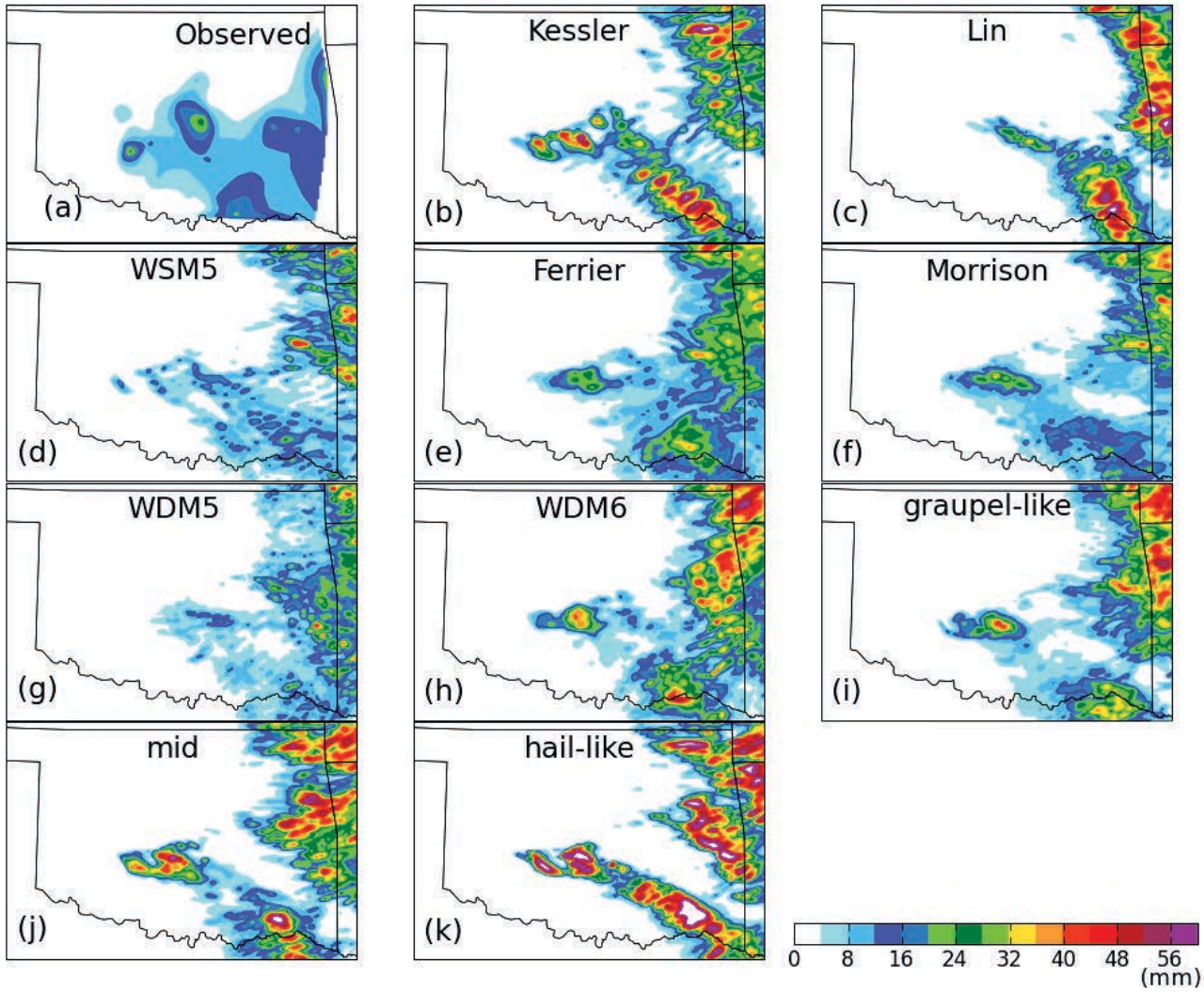

Figure 6.9: Total system accumulated precipitation (mm) for each simulated system and observations (calculated using Oklahoma Mesonet). Precipitation from extraneous simulated convection in northeast Oklahoma is masked out.

melting and evaporation added as the snow aloft finally fell below the melting layer in significant amounts did indeed aid in intensifying the linear systems.

The difference between the largest and smallest simulated stratiform regions, discounting the WDM5 and 6 simulations, was approximately 17,000 km^2, or a variation of over 350%. Given the deficiencies in simulation of stratiform regions documented in the literature (Rutledge and Houze 1987, Nicholls 1987, Szeto et al. 1988, Tao and Simpson 1989, Tao et al. 1993, Szeto and Cho 1994, Chin 1994, Gallus and Johnson 1995, Bryan and Morrison 2012), large variations in the stratiform region are unsurprising.

The convective region sizes differed by 6,700 km^2, or 430% at the point of largest difference. Thus it is clear that the size of simulated reflectivity is heavily dependent on the selected microphysics scheme. Microphysics scheme characteristics of variables other than graupel parameters had a larger effect here: specifically, explicit prediction of cloud condensation nuclei concentration, and lack of ice as a variable. These effects are also more far-reaching than just reflectivity values; cloud cover and ice or liquid water content changes also have significant radiation budget implications.

6.3.5 Accumulated precipitation

Figure 6.9 displays the total accumulated system precipitation of each simulation, as well as the observed values taken from the Oklahoma Mesonet and the NCEP/EMC 4-km Stage-IV gridded analysis. The Stage-IV analysis was included due to the relatively large resolution of the Oklahoma Mesonet gauge network. Every simulation produced extraneous convection over northeast Oklahoma and southeastern Arkansas, which corresponded to observed convection over central Arkansas.

It is obvious from this figure that (1) the choice of microphysics scheme configuration had an enormous effect on the resulting accumulated precipitation and (2) many of the simulations significantly over-forecasted total precipitation. Regarding the latter, this was very likely due to the relatively large, yet currently used operationally, horizontal resolution

of 3 km. Bryan and Morrison (2012) noted that as horizontal resolution decreased, more turbulence was explicitly resolved. Additionally, a larger number of smaller clouds were produced as opposed to a few large clouds, increasing the total cloud surface area. Both of these processes acted to increase cloud water evaporation rates, and decrease precipitation efficiency accordingly. Thus, the schemes which produced lower precipitation totals should not necessarily be considered as having done a "better" job; if simulation resolution was decreased those schemes could begin underpredicting.

However, the point remains that precipitation totals vary between 10 and 60 mm, compared to observed values of approximately 10 to 25 mm. This is a variation of as much as 600% at current operational model resolutions. This has serious implications for warm-season quantitative precipitation forecasting (QPF), and suggests that forecasters should be aware of which microphysics scheme, and its associated biases, is being used to generate a precipitation forecast.

Microphysics configurations containing large, fast-falling, more hail-like graupel hydrometeors, such as the "mid" and "hail-like" configurations, produced the largest precipitation accumulations due to the mean size effect (Figs. 6.9j,k). The fast fallspeeds of the Lin scheme also resulted in larger accumulated precipitation amounts (Fig. 6.9c). These simple changes in the graupel hydrometeor intercept parameter and fallspeed alone accounted for almost all the variation in accumulated precipitation.

For example, the double-moment nature of the WDM5 and WDM6 rain distributions appeared to have little effect. Accumulations in those simulations (Figs. 6.9g,h) were slightly larger than those from the single-moment versions of the schemes (Figs. 6.9d,i), similar to results found in Bryan and Morrison (2012). However, the variations were minimal compared to those yielded by changing the graupel characteristics.

The double moment Morrison scheme (Fig. 6.9f) also did not produce significantly more accumulated precipitation than the single-moment configurations. In Morrison et al. (2009), van Weverberg et al. (2012), and Bryan and Morrison (2012), the double-moment Morrison

scheme simulation did produce more precipitation than the simulation with a modified single-moment Morrison. The double-moment simulation allowed the concentrations of small rain hydrometeors to decrease in the stratiform region, yielding less evaporation and more precipitation. However, the range of fallspeeds for the Morrison graupel parameter (Fig. 6.2b) was generally less than the graupel fallspeeds of the single-moment schemes used in this study (specifically, "graupel-like", "mid", WDM6, and Lin; all originally based on Lin et al. (1983)). These slower fallspeeds in the Morrison scheme would allow more time for melting and evaporation, counteracting the decreased evaporation rates expected due to the double-moment nature of the rain and graupel distributions. Thus, the Morrison and single-moment schemes ended up producing approximately equivalent amounts of accumulated precipitation.

The large values of accumulated precipitation produced by the Kessler scheme agree with the study by Gilmore et al. (2004b). In that study, the increased Kessler rainfall totals were a result of the faster rain drop production rate by cloud droplet accretion and autoconversion. These increased rain drop production rates are a unique feature of the Kessler scheme. In the Gilmore et al. (2004b) study a comparison simulation was run using the Lin scheme with only liquid; that simulation produced approximately 40% less precipitation than the simulation using the Lin scheme that included ice. Thus, removal of ice alone would not act to increase precipitation.

In summary, the size of the graupel hydrometeors played the largest role in modifying precipitation totals in these sensitivity tests, more so than the single- or double-moment nature of the graupel or rain classes. The totals differed in some locations by a factor of 600% due to these variations.

6.4 Summary

Within this chapter, the 13 March 2003 bow echo was simulated in a WRF case study simulation with eight different microphysics schemes. The resulting variations in five different operational forecasting parameters were evaluated and compared to observations. The

five parameters were time of bowing development, maximum 10-m wind gust speed, system propagation speed, convective and stratiform region areal coverage, and accumulated precipitation.

- The time bowing initiated varied by 105 minutes, with the simulations using microphysics schemes with smaller, more "graupel-like" graupel parameters bowing first due to increased cooling. This agrees with the results presented in Chapter 5.
- The increased cooling resulted in system speeds approximately 30% faster.
- The faster-bowing systems also produced 10-m wind gusts 150% stronger than simulations that contained slower-bowing systems.
- The simulations with microphysics schemes with slower-falling, more "hail-like" graupel hydrometeors produced precipitation accumulation totals up to 600% higher than simulations with "graupel-like" graupel hydrometeors. This effect was even larger than variations caused by switching from single- to double-moment distributions.
- Finally, convective areal coverage differed by 430% among simulations. Stratiform areal coverage differed by 350%. This was mainly due to inclusion of prognostic cloud condensation nuclei in a scheme, as opposed to variations in the graupel characteristics.

CHAPTER 7

SUMMARY AND CONCLUSIONS

7.1 Summary and discussion of presented results

In this dissertation, the effect of microphysical heating and cooling rates on bow echo development was evaluated. The focus was twofold: (1) the study of the gravity waves generated by the convective system's microphysical heating profiles and their feedback to the system, and (2) direct microphysical effects on the strength of the system cold pool, mid-level pressure perturbation, and rear-to-front flow.

A number of surface pressure features observed by Adams-Selin and Johnson (2010) in conjunction with the 13 March 2003 bow echo over Oklahoma are further evaluated, using both additional examination of the observations and a high-resolution numerical model simulation. The observed surface pressure features include one approximately 2 hPa temporary decrease in pressure that propagates quickly away from the convective line at 32.5 m s^{-1}, followed by a subsequent rise, dip, and rise in pressure. These propagate away at approximately the same speed. Also observed is a surge of increasing pressure ahead of the convective line. Pressure surges of this nature were observed in 35 of 39 bow echoes examined by Adams-Selin and Johnson (2010). The surges generally occurred immediately prior to or at the same time as the bow echo developed.

An idealized Cloud Model 1 (CM1) numerical simulation was performed in an attempt to understand the processes generating these features. In the simulation, numerous gravity waves were generated by the evolving heating profile. Fluctuations in the amplitude of deep convective heating generated $n = 1$ gravity wave responses that traveled quickly away from the convective line, as theorized by Nicholls et al. (1991). An increase in the heating resulted in a wave with subsidence throughout the tropospheric column and corresponding warming and drying with a low surface pressure perturbation; a decrease in that profile resulted in

a wave with ascent throughout the column, and subsequent cooling and moistening with a high surface pressure perturbation.

Not only did the modeled $n = 1$ waves propagate at nearly the same speed as the observed fast-moving low pressure feature (32 m s^{-1} and 32.5 m s^{-1}, respectively), the vertical structure of the modeled feature matched theoretical studies (Nicholls et al. 1991) exactly. Thus, it was concluded that the observed fast-moving pressure features were indeed $n = 1$ gravity waves. Wave generation was also very frequent and associated with fluctuations in the $n = 1$ heating profile. Eighteen $n = 1$ waves were produced just in this 2.6-h simulation, and surface reflections of four $n = 1$ waves were noted in the observations. Within the simulation, each $n = 1$ wave modified the pre-storm CAPE profile by between 5 to 7% of the initial CAPE value.

A surge of increasing pressure occurs ahead of the bowing segment of the convective line as bowing develops. This simulated pressure feature propagates at a speed of approximately 11.0 m s^{-1}, in good agreement with an n=3 wave (with a speed of 9.8 m s^{-1}) postulated to be excited by strong low-level cooling. Shortly prior to surge development, the system's front-to-rear inflow and convective updraft increases within this segment, strengthening the mid-level pressure perturbation, and resulting in an increase in rear-to-front flow. This increases low-level microphysical cooling and convective downdrafts up to 4 km by introducing additional dry air; the cooling generates the gravity wave. An approximate 250 J kg^{-1} increase in CAPE, or 7% of the initial sounding, is noted in conjunction with the combination of the pressure surge and other higher-frequency features, suggesting lifting and moistening is occurring at lower levels. This higher CAPE partially explains the increasing strength of the convective updraft in the bowing segment at time of bowing, despite increased updraft tilt due to a strengthening cold pool and surface-based rear-to-front flow.

The appearance of the pressure surge can be explained in the context of Haertel and Johnson (2000) wherein the linear response to a moving low-level cool source was investigated. In that study it was found that when the gravity wave speed associated with the vertical

scale of the cooling approximately matched the speed of the cool source, an amplification of the surface pressure response occurred. The modeling results here are analogous.

Finally, a number of high-frequency features, updraft-downdraft couplets that produced small clouds, are trapped in the 2 to 2.5 km stable layer in advance of the system. These features are similar to those modeled by Fovell et al. (2006), although in this case they are trapped by a much lower unstable layer as opposed to the curvature of the wind profile due to the outflowing anvil aloft. The latent heat release associated with the clouds that form within the updraft portion of each wave modifies the pre-storm stable layer by decreasing its stability and the environmental CIN, and increasing the CAPE. However, these effects are more noticeable after passage of the pressure surge. The more gentle lifting generated by that low-frequency wave moderately cools and moistens the lower troposphere, allowing larger destabilizing effects to be generated by the high frequency features. The results support the mechanisms described by Fovell et al. (2006).

The results herein have multiple implications for current convective modeling. As has already been noted in other studies (Lane and Reeder 2001), these types of gravity waves have a significant effect on the pre-storm environment. However, in this study waves are continually generated by both strengthening and weakening of the convective heating profile. Wave fronts generated in response to a weakening of the amplitude of the $n = 1$ heating profile had not been previously observed except in theory (Nicholls et al. 1991). Each passage of just one of these waves significantly modifies the pre-storm environment, making characterization of the pre-storm environment much more difficult than previously supposed.

The lifting and subsequent destabilization created by the pressure surge gravity wave, and associated increase in updraft strength, would positively feed back to the system, helping it further intensify as the bowing process occurs. This indicates that the gravity waves generated by a system can have a feedback effect of short time scales. An interesting point is that this simulated bow echo had not yet produced large amounts of stratiform precipitation. Typically higher vertical wave modes are associated with melting and evaporation in the

stratiform region; this case shows that such a profile can be created within the convective region alone.

In order to more fully evaluate the vertical structure of the gravity waves produced in Chapter 3's simulation, two microphysical heating profiles from that simulation were used as constant heat sources in dry simulations in Chapter 4. The two profiles selected were from 0:40 simulation time, shortly after generation of a $n = 1$ wave, and 1:50, immediately prior to the development of the pressure surge. In both dry simulations, $n = 1$, 2, 3, and 4 waves developed, with the $n = 2$ and 4 waves generated by a heating profile including low-level cooling, and the $n = 3$ wave with low-level warming. All four waves in both simulations generally exhibited propagation speed, and pressure and temperature structure, as predicted by theory (Nicholls et al. 1991).

In the dry simulation containing the heating profile from just prior to surge development, a $n = 4$ wave developed that appeared very similar to the pressure surge. Significant upward vertical motion was colocated with this wave from 0-4 km aloft, as well as a 100 J kg^{-1} increase in CAPE. This agrees with the premise in Chapter 3 that the pressure surge was a low-frequency wave generated by low-level cooling.

A statistical method was developed to predict which gravity wave modes would be generated based on the one-dimensional vertical mean of each heating profile. This method worked well for the profile from early in the convective simulation, which did not have much horizontal variation. However, the heating profile from just prior to the surge development was more horizontally heterogenous, and the statistical method did not correctly predict all the generated waves. This suggests that the horizontal and vertical distribution of the heating are both important, agreeing with the results from Pandya and Durran (1996).

Chapter 5 examined the effect of changes in microphysical cooling rates on bow echo generation, specifically through the connections among cold pool strength, rear-to-front flow, and convective updraft tilt. Multiple WRF simulations were performed over a spectrum of graupel class parameters in a microphysical parameterization scheme, in order to directly

and consistently vary the microphysical heating and cooling rates. The graupel parameter variations acted to render the class larger, more dense and "hail-like", or smaller, lighter and "graupel-like". Additional simulations looked at the effects of removing graupel completely.

The simulations with a larger, more dense "hail-like" graupel class had these hydrometeors fall out of the updraft almost immediately, close to the convective line, and allowing for little melting or evaporation. This resulted in a minimal stratiform precipitation region and reduced convective intensity. The system was less favorable to new bowing development, producing rear-to-front flow which did not descend to the surface until shortly before the convective line, and an updraft which remained minimally tilted throughout.

The simulations with a smaller, less dense "graupel-like" graupel class had smaller graupel hydrometeors that were slower to fall, creating a wide stratiform precipitation region. This allowed for more melting and evaporation, and yielded a wider, deeper, and stronger cold pool. The rear-to-front flow descended to the surface quite some distance behind the convective line, aiding further rearward tilt of the updraft. This helped generate bowing segments earlier than in the hail-like simulations.

A sensitivity test with smaller "graupel-like" hydrometeors that fell at the same speed as "hail-like" hydrometeors showed that their small mean size produced higher latent cooling rates, despite the decreased in-storm residence time. The faster fallspeeds concentrated this cooling close to the convective line by allowing little advection, thereby creating a intense cold pool, surface-based rear-to-front flow, and faster new bowing development.

The various cloud and ice particles generated by the "no-graupel" (5-class) simulation remained almost entirely aloft for some time after initiation as the large amounts of snow generated fell slowly. Some time was required for the snow to reach the melting level. Until that point the melting and evaporation rates were minimal, and the cold pool initially not as intense as the "graupel" simulation (6-class). The resulting mid-level pressure perturbation and rear-to-front flow were weaker as well. Over time the cooling due to melting and evapo-

ration increased as snow reached lower levels, forcing earlier descent of the rear-to-front flow to the surface and temporarily tilting the convective updraft, thus developing a bow echo.

While the study in Chapter 5 examined idealized sensitivities to model microphysical schemes, such variations to the microphysics can occur in reality. For example, the introduction of dust into a system can drastically modify the concentration of both cloud condensation and ice-forming nuclei, as was seen in Twohy et al. (2010). This naturally results in significantly different size distributions of all hydrometeors in deep convection (van den Heever et al. 2006, Storer et al. 2010); this particularly affects the heating and cooling rates as discussed here. There are many further environmental factors that could result in similar microphysical changes, such as variations in nearby temperature, moisture, or shear profiles. Changes in these profiles have been shown to primarily affect system circulation by modifying the internal system thermal forcing (Pandya and Durran 1996; Pandya et al. 2000), so these results are of note.

Therefore, the study in Chapter 6 was designed to evaluate these microphysical changes in a forecasting context. The 13 March 2003 bow echo was run as a case study using WRF. Eight different microphysics schemes were utilized to examine and quantify the differences produced by these variations within the case study simulations, specifically regarding the graupel hydrometeor class (or lack thereof). Five operational forecasting parameters were selected to examine the resultant effects of changes to the graupel parameter on a bow echo simulation.

The time of bowing initiation was strongly affected. The largest impact was from the graupel/hail modifications: the "graupel-like" system bowed 105 minutes earlier than the "hail-like" system. As noted in Chapter 5, the increased cooling associated with the "graupel-like" graupel hydrometeor, and shift in the peak cooling rearward due to its increased mobility, resulted in a faster descent of the rear-to-front flow to the surface, an increased tilt rearward of the convective updraft, and faster development of bowing. In general, systems that bowed faster also had stronger 10-m wind gusts, approximately 150% stronger, due to

the increased low-level downdrafts and more surface-based rear-to-front flow from higher microphysical cooling rates. The increased cooling rates also resulted in faster systems speeds, at approximately 30%.

Systems with smaller, slower-falling, more graupel-like hydrometeors had a much lower precipitation efficiency, producing accumulated precipitation values as much as 600% lower than systems simulated using schemes with heavier, less numerous, and faster-falling graupel (or "hail-like") hydrometeors. Accumulated precipitation was by far the parameter most sensitive to graupel variations examined in this study. Changing the graupel parameter to be more "graupel-like" or "hail-like" had a larger effect than even switching between single- and double-moment rain or graupel distributions, or removing graupel altogether. This is particularly important when considering that the graupel intercept and fallspeed parameters in current microphysics schemes are selected largely arbitrarily due to lack of observed data, and suggests that a field program or other detailed observations of these parameters is warranted.

The total size of the convective and stratiform regions also varied significantly in relation to changes in the microphysics scheme. The difference between the largest and smallest simulated stratiform region area was 350%; between convective areas, 430%. However, this was less due to changes in the graupel parameter, and more likely because of the inclusion of cloud condensation nuclei as a prognostic variable. Among the modified WSM6 configurations designed to test graupel sensitivity, the stratiform (convective) regions varied by approximately 200% (300%).

Thus, it is clear that simple modifications to how graupel is represented within a microphysics scheme used to simulate a case study can have noteworthy effects on the resulting convective system. This has serious implications for operational forecasting, and suggests that forecasters should be aware of which microphysical parameterization - and its associated biases - is being used to produce the model forecast being evaluated. Multi-physics ensembles should also be constructed in a way that incorporates complementary biases. For

example, the WDM6 scheme has a graupel parameter with a generally small mean size and therefore strong cold pools. If that scheme is included in an ensemble, a microphysics scheme scheme with a double-moment graupel distribution that allows for a large mean graupel size should also be included, for balance.

Given all of the results described herein, it can be concluded that the horizontal and vertical distributions of microphysical heating and cooling within a convective system both have a very significant impact on the subsequent development of bowing and other associated convective features. This impact can either be direct, through variations in cold pool and mid-level buoyancy and pressure gradient strength, or indirect, through modification to the pre-storm environment by generation of gravity waves.

7.2 Suggested future work

Multiple avenues of future work are suggested by these results. The most obvious would be to evaluate how the gravity wave features generated by the microphysical heating profile vary as the profile is modified by changes to the graupel distribution. While this study connected the variations in the cooling rates to the descent of the rear-to-front flow to the surface via the mid-level pressure perturbation, Pandya and Durran (1996) have found that the initial onset of that flow is caused by a rearward propagating gravity wave. While such a gravity wave was not clearly seen in the graupel sensitivity simulations, it is possible use of higher resolution, an increased model top height, or even a different model could reveal these features and their subsequent effect on the convective system.

Additional work could further examine the structure of the heating profile that generated these wave features. It was assumed in this study that diabatic heating was responsible for generation, but Lane and Reeder (2001) have noted that other nonlinear heat sources, such as adiabatic cooling from vertical advection, and vertical advection of buoyancy, are possible. Even if the heating profile was entirely diabatic, the breakdown of processes responsible, such as the individual rates of evaporation and melting, would be useful. This is particularly

true regarding the low-level cooling which both generated the pressure surge and, shortly thereafter, the new bowing development. As it was shown here that variations in these rates can affect new bowing development through the mid-level low pressure region, it is likely that those same variations will affect the pressure surge and its associated feedbacks.

The pressure surges associated with bowing observed in ASJ10 occurred in both day and nighttime, so a stable boundary layer was not required to produce the observed feature. Nor was one required to produce the simulated pressure surge gravity wave. However, in the event of a stable nighttime boundary layer, it would be of interest to note if the low-level cooling preceding bowing development generates a bore that moves ahead of the convective system, much as the gravity wave did in this study.

As has been noted, the microphysical sensitivity of supercells has already been studied (Gilmore et al. 2004a; van den Heever and Cotton 2004, 2007; Dawson et al. 2010; Snook and Xue 2008; Lerach et al. 2008). However, the gravity waves generated by these microphysical heating profiles have not been studied. It is highly likely that, as in this study, the gravity waves produced modify the pre-storm environment and affect the original convective system. For example, Schumacher (2009) found a low-level gravity wave helped organize a convective system to produce large amounts of rainfall.

In a wider scope, the possible variations in convective simulations resulting from changes in the microphysics scheme, even beyond graupel, are numerous. This study has shown that changes in the microphysical rates will cause effects that are wide-reaching throughout the simulation, including variations in the pre-storm environment. Thus, microphysical scheme modifications should be carefully evaluated, and the selection of which scheme to use in a simulation should not be a trivial matter.

Differences caused by changes in the rain drop distribution and concentration, through both single- and double-moment schemes and the introduction of prognostic cloud condensation nuclei, should be examined more thoroughly. This is particularly needed within the ongoing work to couple microphysics schemes with the WRF chemistry model (WRF/Chem;

Ward and Cotton 2011). Quantified variations and comparison to observations of many of the recent idealized hail-graupel comparison studies (Milbrandt and Morrison 2011, van Weverberg et al. 2012) would also be useful, especially the modifications of the graupel class from single- to double-moment, in light of the strong sensitivity to graupel changes forecasting parameters had in this study.

REFERENCES

Adams-Selin, R. D., and R. H. Johnson, 2010: Mesoscale surface pressure and temperature features associated with bow echoes. *Mon. Wea. Rev.*, **138**, 212–227.

Alexander, C. R., S. S. Weygandt, S. G. Benjamin, T. G. Smirnova, J. M. Brown, P. Hofmann, and E. P. James, 2011: The High Resolution Rapid Refresh (HRRR): Recent and future enhancements, time-lagged ensembling, and 2010 forecast evaluation activities. *20th Conf. on Num. Weather Pred.*, Seattle, Washington.

American Meteorological Society, 2000: Glossary of meteorology. This is an electronic document. Date of publication: June, 2000. Date retrieved: June 23, 2012. Date last modified: [unavailable]. URL http://amsglossary.allenpress.com/glossary/preface2

Biggerstaff, M. I., and R. A. Houze, 1991: Kinematic and precipitation structure of the 10-11 June 1985 squall line. *Mon. Wea. Rev.*, **119**, 3034–3065.

——, and R. A. Houze, 1993: Kinematics and microphysics of the transition zone of the 10-11 June 1985 squall line. *J. Atmos. Sci.*, **50**, 3091–3110.

Bretherton, C. S., and P. K. Smolarkiewicz, 1989: Gravity waves, compensating subsidence and detrainment around cumulus clouds. *J. Atmos. Sci.*, **46**, 740–759.

Bryan, G. H., and J. M. Fritsch, 2002: A benchmark simulation for moist nonhydrostatic numerical models. *Mon. Wea. Rev.*, **130**, 2917–2928.

——, and R. Rotunno, 2009: The maximum intensity of tropical cyclones in axisymmetric numerical model simulations. *Mon. Wea. Rev.*, **137**, 1770–1789.

——, and M. D. Parker, 2010: Observations of a squall line and its near environment using high-frequency rawinsonde launches during VORTEX2. *Mon. Wea. Rev.*, **138**, 4076–4097.

——, and H. Morrison, 2012: Sensitivity of a simulated squall line to horizontal resolution and parameterization of microphysics. *Mon. Wea. Rev.*, **140**, 202–225.

——, J. C. Knievel, and M. D. Parker, 2006: A multimodel assessment of RKW theory's relevance to squall-line characteristics. *Mon. Wea. Rev.*, **134**, 2772–2792.

Chen, S., and W. R. Cotton, 1988: The sensitivity of a simulated extratropical mesoscale convective system to longwave radiation and ice-phase microphysics. *J. Atmos. Sci.*, **45**, 3897–3910.

Cheng, L., M. English, and R. Wong, 1985: Hailstone size distributions and their relationship to storm thermodynamics. *J. Climate App. Meteor.*, **24**, 1059–1067.

Chin, H. N. S., 1994: The impact of the ice phase and radiation of a midlatitude squall line system. *J. Atmos. Sci.*, **51**, 3320–3343.

Clark, A. J., and Coauthors, 2012: An overview of the 2010 Hazardous Weather Testbed Experimental Forecast Program Spring Experiment. **93**, 55–74.

Cohen, C. and E. W. McCaul Jr., 2006: The sensitivity of simulated convective storms to variations in prescribed single-moment microphysics parameters that describe particle distributions, sizes, and numbers. *Mon. Wea. Rev.*, **134**, 2547–2565.

Dennis, A. S., P. L. Smith Jr., G. A. P. Peterson, and R. D. McNeil, 1971: Hailstone size distributions and equivalent radar reflectivity factors computed from hailstone momentum records. *J. App. Meteor.*, **10**, 79–85.

Dennis, D. T., II, M. Xue, J. A. Milbrandt, M. K. Yau, 2010: Comparison of evaporation and cold pool development between single-moment and multimoment bulk microphysics schemes in idealized simulations of tornadic thunderstorms. *Mon. Wea. Rev.*, **138**, 1152–1171.

Du, J., G. Dimego, Z. Toth, D. Jovic, B. Zhou, J. Zhu, J. Wang, and H. Juang, 2009: Recent upgrade of NCEP short-range ensemble forecast (SREF) system. *19th Conf. on Num. Weather Pred.*, Omaha, Nebraska.

Ek, M. B., K. E. Mitchell, Y. Lin, E. Rogers, P. Grunmann, V. Koren, G. Gayno, and J. D. Tarpley, 2003: Implementation of Noah land surface model advances in the National Centers of Environmental Prediction operational mesoscale Eta model. *J. Geophys. Res.*, **108**, 8851, doi:10.1029/2002JD003296.

Evans, J., and C. Doswell, 2001: Examination of derecho environments using proximity soundings. *Wea. Forecasting*, **16**, 329–342.

Fanelli, P. F., and P. R. Bannon, 2005: Nonlinear atmospheric adjustment to thermal forcing. *J. Atmos. Sci.*, **62**, 4253–4272.

Federer, B., and A. Waldvogel, 1975: Hail and raindrop size distributions from a Swiss multicell storm. *J. App. Meteor.*, **14**, 91–97.

Ferrier, B. S., Y. Jin, Y. Lin, T. Black, E. Rogers, and G. DiMego, 2002: Implementation of a new grid-scale cloud and precipitation scheme in the NCEP Eta Model. *15th Conf. on Num. Weather Pred.*, San Antonio, Texas.

Fovell, R. G., 2002: Upstream influence of numerically simulated squall-line storms. *Quart. J. Roy. Meteorol. Soc.*, **128**, 893–912.

Fovell, R. G., and Y. Ogura, 1988: Numerical simulation of a midlatitude squall line in two dimensions. *J. Atmos. Sci.*, **45**, 3846–3879.

——, and Y. Ogura, 1989: Effect of vertical wind shear on numerically simulated multicell storm structure. *J. Atmos. Sci.*, **46**, 3144–3176.

——, G. L. Mullendore, and S. H. Kim, 2006: Discrete propagation in numerically simulated nocturnal squall lines. *Mon. Wea. Rev.*, **134**, 3735–3752.

Fujita, T., 1978: Manual of downburst identification for project NIMROD. Technical report, Dept. of Geophysical Sciences, University of Chicago, Chicago, IL.

Gallus, W. A., Jr., and R. H. Johnson, 1991: Heat and moisture budgets of an intense midlatitude squall line. *J. Atmos. Sci.*, **48**, 122-146.

——, and ——, 1995: The dynamics of circulations within the trailing stratiform regions of squall lines. Part II: Influence of the convective line and ambient environment. *J. Atmos. Sci.*, **52**, 2188–2211.

Garner, S. T., and A. J. Thorpe, 1992: The development of organized convection in a simplified squall-line model. *Quart. J. Roy. Meteorol. Soc.*, **118**, 101–124.

Gilmore, M. S., J. M. Straka, and E. N. Rasmussen, 2004a: Precipitation uncertainty due to variations in precipitation particle parameters within a simple microphysics scheme. *Mon. Wea. Rev.*, **132**, 2610–2627.

——, J. M. Straka, and E. N. Rasmussen, 2004b: Precipitation and evolution sensitivity in simulated deep convective storms: Comparisons between liquid-only and simple ice and liquid phase microphysics. *Mon. Wea. Rev.*, **132**, 1897–1916.

Haertel, P. T., R. H. Johnson, and S. N. Tulich, 2001: Some simple simulations of thunderstorm outflows. *J. Atmos. Sci.*, **58**, 504–516.

Hane, C. E., 1973: The squall line thunderstorm: Numerical experimentation. *J. Atmos. Sci.*, **30**, 1672–1690.

Hong, S.Y., and J.O. J. Lim, 2006: The WRF single-moment 6-class microphysics scheme (WSM6). *J. Korean. Meteor. Soc.*, **42**, 129–151.

——, J. Dudhia, S.H. Chen, 2004a: A revised approach to ice microphysical processes for the bulk parameterization of clouds and precipitation. *Mon. Wea. Rev.*, **132**, 103–120.

——, J. M. Straka, E. N. Rasmussen, 2004b: Precipitation and evolution sensitivity in simulated deep convective storms: Comparisons between liquid-only and simple ice and liquid phase microphysics. *Mon. Wea. Rev.*, **132**, 1897–1916.

——, K.S. Sunny Lim, J.H. Kim, J.O. Jade Lim, and J. Dudhia, 2009: Sensitivity study of cloud-resolving convective simulations with WRF using two bulk microphysical parameterizations: Ice-phase microphysics versus sedimentation effects. *J. App. Meteor. Clim.*, **48**, 61–76.

Houze, R. A., Jr., 1982: Cloud clusters and large-scale vertical motions in the tropics. *J. Meteor. Soc. Japan*, **60**, 396–410.

——, S. Rutledge, M. Biggerstaff, and B. Smull, 1989: Interpretation of Doppler weather radar displays of midlatitude mesoscale convective systems. *Bull. Amer. Meteor. Soc.*, **70**, 608–619.

James, R. P., J. M. Fritsch, and P. M. Markowski, 2006: Bow echo sensitivity to ambient moisture and cold pool strength. *Mon. Wea. Rev.*, **134**, 950–963.

Janjic, Z., 1994: The step-mountain eta coordinate model: Further developments of the convection, viscous sublayer, and turbulence closure schemes. *Mon. Wea. Rev.*, **122**, 927–945.

Jankov, I., W. A. Gallus, Jr., M. Segal, B. Shaw, S. E. Koch, 2005: The impact of different WRF model physical parameterizations and their interactions on warm season MCS rainfall. *Wea. Forecasting*, **20**, 1048–1060.

Johnson, A., X. Wang, M. Xue, and F. Kong, 2011: Hierarchical cluster analysis of a convection-allowing ensemble during the Hazardous Weather Testbed 2009 Sprint Experiment. Part II: Ensemble clustering over the whole experiment period. **139**, 3694–3710.

Johnson, R. H., and G. S. Young, 1983: Heat and moisture budgets of tropical mesoscale anvil clouds. *J. Atmos. Sci.*, **40**, 2138–2147.

——, and P. Hamilton, 1988: The relationship of surface pressure features to the precipitation and air flow structure of an intense midlatitude squall line. *Mon. Wea. Rev.*, **116**, 1444-1472.

——, and B. E. Mapes, 2001: Mesoscale processes and severe convective weather. C. A. Doswell III, Ed., AMS Monograph, *Severe Convective Weather*, **28**, 71-122.

Kain, J. S., and Coauthors, 2008: Some practical considerations regarding horizontal resolution in the first generation of operational convection-allowing NWP. *Wea. Forecasting*, **23**, 931–952.

Kessler, E., 1969: On the distribution and continuity of water substance in atmospheric circulations. *Meteor. Monogr. No.* **10**, Amer. Meteor. Soc.

Klimowski, B., M. Bunkers, M. Hjemfelt, and J. Covert, 2003: Severe convective windstorms over the Northern High Plains of the United States. *Wea. Forecasting*, **18**, 502–519.

Knight, C. A., W. A. Cooper, D. W. Breed, I. R. Paluch, P. L. Smith, and G. Valie, 1982: Microphysics. *Hailstorms of the Central High Plains*, C. Knight and P. Squires, Eds., Vol. 1, Colorado Associated University Press, 151–193.

Knupp, K., 2006: Observational analysis of a gust front to bore to solitary wave transition within an evolving nocturnal boundary layer. *J. Atmos. Sci.*, **63**, 2016–2035.

Lafore, J.P., and M. W. Moncrieff, 1989: A numerical investigation of the organization and interaction of the convective and stratiform regions of tropical squall lines. *J. Atmos. Sci.*, **46**, 521–544.

Lane, T. P., and M. J. Reeder, 2001: Convectively generated gravity waves and their effect on the cloud environment. *J. Atmos. Sci.*, **58**, 2427–2440.

——, and M. W. Moncrieff, 2008: Stratospheric gravity waves generated by multiscale tropical convection. *J. Atmos. Sci.*, **65**, 2598–2614.

——, and F. Zhang, 2011: Coupling between gravity waves and tropical convection at mesoscales. *J. Atmos. Sci.*, **68**, 2585-2598.

Lerach, D. G., B. J. Gaudet, and W. R. Cotton, 2008: Idealized simulations of aerosol influences on tornadogenesis. *Geophys. Res. Lett.*, **35**, L23806, doi:10.1029/2008GL035617.

Lim, K.S. S., and S.Y. Hong, 2010: Development of an effective double-moment cloud microphysics scheme with prognostic cloud condensation nuclei (CCN) for weather and climate models. *Mon. Wea. Rev.*, **138**, 1587–1612.

Lin, Y.L., R. D. Farley, and H. D. Orville, 1983: Bulk parameterization of the snow field in a cloud model. *J. Climate App. Meteor.*, **22**, 1065–1092.

Liu, C. and M. W. Moncrieff, 2007: Sensitivity of cloud-resolving simulations of warm-season convection to cloud microphysics parameterizations. *Mon. Wea. Rev.*, **135**, 2854–2868.

Luo, Y., Y. Wang, H. Wang, Y. Zheng, and H. Morrison, 2010: Modeling convective-stratiform precipitation processes on a Mei-Yu front with the Weather Research adn Forecasting model: Comparison with observations and sensitivity to cloud microphysics parameterizations. *J. Geophys. Res.*, **115**, D18117.

Mapes, G. E., 1993: Gregarious tropical convection. *J. Atmos. Sci.*, **50**, 2026–2037.

Marshall, J. S., and W. Mc K. Palmer, 1948: The distribution of raindrops with size. *J. Meteor.*, **5**, 165-166.

McAnelly, R. I., J. E. Nachamkin, W. R. Cotton, and M. E. Nicholls, 1997: Upscale evolution of MCSs: Doppler radar analysis and analytical investigation. *Mon. Wea. Rev.*, **125**, 1083–1110.

McCumber, M., W.K. Tao, J. Simpson, R. Penc, and S.T. Soong, 1991: Comparison of ice-phase microphysical parameterization schemes using numerical simulations of tropical convection. **30**, 985–1004.

Molthan, A. L., J. L. Case, S. R. Dembek, G. J. Jedlovec, and W. M. Lapenta, 2008: The Super Tuesday outbreak: Forecast sensitivities to single-moment microphysics schemes. *24th Conf. on Severe Local Storms*, Savannah, Georgia, 17B.3.

Morrison, H., and J. Milbrandt, 2011: Comparison of two-moment bulk microphysics schemes in idealized supercell thunderstorm simulations. *Mon. Wea. Rev.*, **139**, 1103–1130.

——, G. Thompson, and V. Tatarskii, 2009: Impact of cloud microphysics on the development of trailing stratiform precipitation in a simulated squall line: Comparison of one- and two-moment schemes. *Mon. Wea. Rev.*, **137**, 991–1007.

Nicholls, M. E., 1987: A comparison of the results of a two-dimensional numerical simulation of a tropical squall line with observations. *Mon. Wea. Rev.*, **115**, 3055–3077.

——, R. A. Pielke, Sr., 2000: Thermally induced compression waves and gravity waves generated by convective storms. *J. Atmos. Sci.*, **57**, 3251–3271.

——, R. H. Johnson, and W. R. Cotton, 1988: The sensitivity of two-dimensional simulations of tropical squall lines to environmental profiles. *J. Atmos. Sci.*, **45**, 3625–3649.

——, R. A. Pielke, and W. R. Cotton, 1991: Thermally forced gravity waves in an atmosphere at rest. *J. Atmos. Sci.*, **48**, 1869–1884.

Pandya, R. E., and D. R. Durran, 1996: The influence of convectively generated thermal forcing on the mesoscale circulation around squall lines. *J. Atmos. Sci.*, **53**, 2924–2951.

——, D. R. Durran, and M. L. Weisman, 2000: The influence of convective thermal forcing on the three-dimensional circulation around squall lines. *J. Atmos. Sci.*, **57**, 29–45.

Parker, M. D., 2008: Response of simulated squall lines to low-level cooling. *J. Atmos. Sci.*, **65**, 1323–1341.

——, 2010: Relationship between system slop and updraft intensity in squall lines. *Mon. Wea. Rev.*, **138**, 3572–3578.

Pruppacher, H. R., and J. D. Klett, 1978: *Microphysics of Clouds and Precipitation.* D. Reidel, 714 pp.

Rotunno, R., J. B. Klemp, M. L. Weisman, 1988: A theory for strong, long-lived squall lines. *J. Atmos. Sci.*, **45**, 463–485.

Rutledge, S. A., and P. V. Hobbs, 1983: The mesoscale and microscale structure and organization of clouds and precipitation in mid-latitude cyclones. Part VIII: A model for the "seeder feeder" process in warm-frontal rainbands. *J. Atmos. Sci.*, **40**, 1185–1206.

——, and R. A. Houze, 1987: A diagnostic modeling study of the trailing stratiform region of a midlatitude squall line. *J. Atmos. Sci.*, **44**, 2640–2656.

Schmidt, J. M., and W. R. Cotton, 1990: Interactions between upper and lower tropospheric gravity waves on squall line structure and maintenance. *J. Atmos. Sci.*, **47**, 1205–1222.

Schumacher, R. S., 2009: Mechanisms for quasi-stationary behavior in simulated heavy-rain producing convective systems. *J. Atmos. Sci.*, **66**, 1543–1568.

Schwartz, C. S., and Coauthors, 2010: Toward improved convection-allowing ensembles: Model physics sensitivities and optimizing probabilistic guidance with small ensemble membership. *Wea. Forecasting*, **25**, 263–280.

Skamarock, W. C., and M. L. Weisman, 2009: The impact of positive-definite moisture transport on NWP precipitation forecasts. *Mon. Wea. Rev.*, **137**, 488–494.

——, J. B. Klemp, J. Dudhia, D. O. Gill, D. M. Barker, M. G. Duda, X.Y. Huang, W. Wang, and J. G. Powers, 2008: A description of the Advanced Research WRF Version 3. NCAR Tech. Note NCAR/TN-475+STR, 113 pp.

Smith, J. W., and P. R. Bannon, 2008: A comparison of compressible and anelastic models of deep dry convection. *Mon. Wea. Rev.*, **136**, 4555–4571.

Snook, N. A., and M. Xue, 2008: Effects of microphysical drop size distribution on tornadogenesis in supercell thunderstorms. *Geophys. Res. Lett.*, **35**, L24803, doi: 10.1029/2008GL035866.

Spahn, J. E., 1976: The airborne hail disdrometer: An analysis of its 1975 performance. Rep. 76-13, Institute of Atmospheric Sciences, South Dakota School of Mines and Technology, Rapid City, SD, 65 pp.

Steiner, M., R. A. Houze, Jr., and S. E. Yuter, 1995: Climatological characterization of three-dimensional storm structure from operational radar and rain gauge data. *J. App. Meteor.*, **34**, 1978–2007.

Stensrud, D. J., M. C. Coniglio, R. P. Davies-Jones, J. S. Evans, 2005: Comments on "'A Theory for Strong Long-Lived Squall Lines' Revisited." *J. Atmos. Sci.*, **62**, 2989–2996.

Stoelinga, M. T., 2005: Simulated equivalent reflectivity factor as currently formulated in RIP: Description and possible improvements, Read/Interpolate/Plot implementation document.

Storer, R. L., S. C. van den Heever, and G. L. Stephens, 2010: Modeling aerosol impacts on convective storms in different environments. *J. Atmos. Sci.*, **67**, 3904–3915.

Szeto, K. and H. Cho, 1994: A numerical investigation of squall lines. Part III: Sensitivity to precipitation processes and the Coriolis force. *J. Atmos. Sci.*, vol 51 1341–1351.

——, R. E. Stewart, and C. A. Lin, 1988: Mesoscale circulations forced by melting snow. Part II: Application to meteorological features. *J. Atmos. Sci.*, **45**, 1642–1605.

Tao, W. K., and J. Simpson, 1989: Modeling study of a tropical squall-type convective line. *J. Atmos. Sci.*, **46**, 177–202.

——, J. Simpson, C. H. Sui, B. Ferrier, S. Lang, J. Scala, M. D. Chou, and K. Pickering, 1993: Heating, moisture, and water budgets of tropical and midlatitude squall lines: Comparisons and sensitivity to longwave radiation. *J. Atmos. Sci.*, **50**, 673–690.

——, and Coauthors, 2003: Microphysics, radiation, and surface processes in the Goddard Cumulus Ensemble (GCE) model. *Meteor. Atmos. Phys.*, **82**, 97–137.

Thompson, G., P. R. Field, R. M. Rasmussen, and W. D. Hall, 2008: Explicit forecasts of winter precipitation using an improved bulk microphysics scheme. Part II: Implementation of a new snow parameterization. *Mon. Wea. Rev.*, **136**, 5095–5115.

Thorpe, A. J., M. J. Miller, and M. W. Moncrieff, 1982: Two-dimensional convection in non-constant shear: A model of midlatitude squall lines. *Quart. J. Roy. Meteorol. Soc.*, **108**, 739–762.

Twohy, C. H., P. J. DeMott, K. A. Pratt, R. Subramanian, G. L. Kok, S. M. Murphy, T. Lersch, A. J. Heymsfield, Z. Wang, K. A. Prather, and J. H. Seinfeld, 2010: Relationships of biomass-burning aerosols to ice in orographic wave clouds. *J. Atmos. Sci.*, **67**, 2437–2450.

van den Heever, S. C., and W. R. Cotton, 2004: The impact of hail size on simulated supercell storms. *J. Atmos. Sci.*, **61**, 1596–1609.

——, and W. R. Cotton, 2007: Urban aerosol impacts on downwind convective storms. *J. App. Meteor.*, **46**, 828–850.

——, G. G. Carrió, W. R. Cotton, P. J. DeMott, and A. J. Prenni, 2006: Impacts of nucleating aerosol on Florida storms. Part I: Mesoscale simulations. *J. Atmos. Sci.*, **63**, 1752–1775.

van Weverberg, K., N. P. M. van Lipzig, Laurent Delobbe, 2011a: Evaluation of moist processes during intense precipitation in km-scale NWP models using remote sensing and in-situ data: Impact of microphysics size distribution assumptions. *Atmos. Res.*, **99**, 15–38.

——, N. P. M. Lipzig, and L. Delobbe, 2011b: The impact of size distribution assumptions in a bulk one-moment microphysics scheme on simulated surface precipitation and storm dynamics during a low-topped supercell case in Belgium. *Mon. Wea. Rev.*, **139**, 1131–1147.

——, A. M. Vogelmann, H. Morrison, and J. Milbrandt, 2012: Sensitivity of idealized squall line simulations to the level of complexity used in two-moment bulk microphysics schemes.

Ward, D., and W. Cotton, 2011: A method for forecasting cloud condensation nuclei using predictions of aerosol physical and chemical properties from WRF/Chem. *J. App. Meteor. Clim.*, **50**, 1601–1615.

Weisman, M. L., 1992: The role of convectively generated rear-inflow jets in the evolution of long-lived mesoconvective systems. *J. Atmos. Sci.*, **49**, 1826–1847.

——, 1993: The genesis of severe long-lived bow echoes. *J. Atmos. Sci.*, **50**, 645–670.

——, and R. Rotunno, 2004: "A theory for strong long-lived squall lines" revisited. *J. Atmos. Sci.*, **61**, 361–382.

——, and ——, 2005: Reply. *J. Atmos. Sci.*, **62**, 2997–3002.

——, W. C. Skamarock, and J. B. Klemp, 1997: The resolution dependence of explicitly modeled convective systems. *Mon. Wea. Rev.*, **125**, 527–548.

Yang, M.J., and R. A. Houze Jr., 1995: Sensitivity of squall-line rear inflow to ice microphysics and environmental humidity. *Mon. Wea. Rev.*, **123**, 3175–3193.

Zhang, D. L, and K. Gao, 1989: Numerical simulation of an intense squall line during 10-11 June 1985 PRE-STORM. Part II: Rear inflow, surface pressure perturbations, and stratiform precipitation. *Mon. Wea. Rev.*, **117**, 2067–2094.